
SAPIENZA
UNIVERSITÀ DI ROMA

## Facoltà di Ingegneria

**Dottorato di ricerca in Ingegneria Ambientale e Idraulica**

XXIX CICLO

# *NDT for the diagnosis of modern, historical and archaeological structures*

Tutor: Prof.ssa Luciana Orlando

Coordinator: Prof.ssa Maria Rosaria Boni

Luca Di Giambattista

December 2016

# Contents

# ABSTRACT

This thesis has been developed with the aim to explore thoroughly potential and limit of the GPR and ERT methods for monitoring heterogeneous structures where different construction materials are combined together.

Firstly we analysed the GPR response, in various construction materials related to different modern, historical or archaeological structures. In particular, three real examples were investigated during the thesis, namely: the Pyramid of Caius Cestius, the Passage of Commodus and the Colle Oppio Ninpheum, all in Rome. According to the different types of material and frequency antennas, different GPR responses and therefore dissimilar degree of resolution and of attenuation was obtained.

In light of this, the interposition between the surface of the investigated medium and the GPR antenna of a dielectric material (e.g. Plexiglas) was performed in order to improve the resolution.

Furthermore, an application of the GPR and ERT methods for monitoring a load test executed on masonry samples was presented. This panels were built up in the laboratory controlled conditions using tuff and bricks (widespread materials employed in Italy for decades for masonry buildings) and also were reproduced in the phase of theoretical modeling. The laboratory samples are reinforced with a conductive fibre fabric, where a high-conductive material (steel wires) is combined together with a dielectric material (basalt fibre).

In order to improve the sample-antenna coupling in the presence of conductive reinforcements, a Plexiglas (polimetilmetacrilato - PMMA) plate was added underneath a 2 GHz antenna. GPR data were acquired along profiles spaced 0.1 m apart and ERT measurements were executed on a 0.1 m regular spaced grid with a dipole-dipole array operating in a three-dimensional configuration. GPR datasets were also analysed in non-conventional mode, by means of the picking of the reflection time of the EM wave from the rear face of the wall samples.

Results show that GPR and electrical resistivity tomography were both able to detect fractures and weakness zones caused by the load application, even though with a higher resolution for the georadar with respect to the geoelectrical method. Moreover, mapping

the GPR data in terms of the dielectric constant and mean absolute amplitude is particularly diagnostic to detect the effective fracturing pattern, after the application of the diagonal load. Therefore, GPR and ERT methods can reduce the degree of uncertainty in the detection of fractures, voids or cavities, with respect to the standard processing, by the combined analysis of radargrams, time-slices and resistivity ERT models.

Furthermore, for the GPR laboratory data acquired directly on the reinforced face of samples, it is demonstrated how interposing a layer of dielectric material between the antenna and the structure can substantially improve the antenna coupling and consequently the capability to detect fractures and to reach the rear face of the sample, despite losing resolution in the case of shallow high-conductive layers.

Finally, three-dimensional synthetic simulations on the same samples validate the experimental evidences. Therefore, we demonstrate that this approach can be a reliable tool to monitor static load tests and it can be further extended to the whole load cycle (before, during and after the experiment).

# INTRODUCTION

## 0.1 Background

Modern, archaeological and historical buildings are significant symbols of any culture's heritage, and it is important to prioritize their protection against such destructive forces as earthquake, flooding, freeze/thaw cycles, atmospheric and other natural agents. The preservation of these structures is important for several reasons, from the historical, social, aesthetic, and scientific point of view.

Furthermore, the above cited natural phenomena are not alone in inflicting damage on the structural integrity of a building; the effects of live loads and their resultant vibrations are also capable of causing severe damage such as fissures, delamination and cracks. In turn, these can weaken the structure and even lead to its eventual collapse, with a consequent increase of environmental hazards and the gravity of the incidental events. Moreover, as some structural deterioration takes place beneath the ground level, visual inspection cannot offer a comprehensive means of assessing a structure's state, which makes the application of (NDT) highly desirable.

Whilst comprehensive building guidelines exist for the new structures, the construction methods and materials for historic buildings would have varied greatly, depending chiefly upon the era in which the building work was undertaken. The old building materials will largely consist of bricks, stones, adobe and mortar, with blocks size building style again varying depending upon the construction era and the building location.

The high seismic vulnerability of the existing unreinforced masonry structures, highlighted by the recent earthquakes occurred in the last few decades in Central Italy (1997, 2002, 2009, 2012, 2016), calls for investigation of the existing masonry building and for understanding potential and limits of reinforcements applicable to the structures.

However, undertaking a reliable risk assessment of a building is extremely challenging, involving qualitative and quantitative methods to ensure accurate judgments relating to its maintenance. Qualitative data can be retrieved by way of inspection of deterioration in combination with a defects and relevant literature review, but the collection of quantitative data is more problematic, involving complex integrated collection methods.

In this sense, in the last two decades, the use of NDT for the study and preservation of cultural heritage menaced by the ravages of time, human interventions or natural

phenomena, has gained increasing interest due to several reasons: (i) the continuing improvement in survey equipment performance, automation and information resolution of sensors and devices; (ii) the advances in processing and imaging software; (iii) the non-destructive nature and the cost-effectiveness over traditional excavation (Cardarelli et al., 2016).

Therefore, the application of geophysical non-destructive testing can be an important tool for assessing the current state of a masonry structure. Among the different geophysical methods, the most used for these purposes is surely the Ground Penetrating Radar (GPR) whose application on masonry structures constitutes the core of this thesis.

## 0.2 Motivation and objectives

Although being a high-resolution technique, the GPR response can change as a function of different types of construction materials related to different modern, historical or archaeological structures and this issue can affect the capability to correctly establish the construction materials or to detect fractures, joints, reinforcements. In light of this, a preliminary field study involving three test sites performed during the thesis, allows to understand the main issues normally encountered in GPR survey of archeological structures and to steer the main goal of this thesis towards more focused laboratory experiments.

As a matter of fact, the GPR signal has the disadvantage of a low depth of penetration in cases of conductive media (Daniels, 2009), a case that often occurs for structural applications due to the presence of moisture or metallic objects (e.g. reinforcements). Furthermore, in many practical cases it is difficult to identify, with a sufficient degree of confidence, the effective presence of fractures (mainly directed normally to the investigated surface), because the horizontal sampling interval is often too large compared to the limited thickness of the fracture, employing common used frequencies and spatial sampling. In addition to this, it is not always possible to establish a quantitative relationship between the GPR anomalies and the presence of a certain type of construction materials, particularly for heterogeneous structures where different construction materials are combined together.

In light of this, the aim of this thesis is:

- to evaluate an improvement of the GPR response in terms of horizontal and vertical resolution as a function of frequency of the antenna and the type of materials;
- to improve the wall-antenna coupling particularly for rough surfaces and conductive material;
- to understand the detectability of critical elements (fractures, slackening, etc.) and of thicknesses and geometries of the masonry;
- to evaluate the type of construction materials of the masonry structure;
- to assess the change in the electromagnetic and electrical response of the constituent structural elements in the laboratory sample, in terms of attenuation and different degree of resolution, before and after the application of a stress on a masonry samples;
- to determine the advantages and drawbacks of GPR, investigation for the characterization of reinforced and unreinforced masonry samples, also Electrical Resistivity Tomography (ERT) was applied in order to reduce the uncertainty of data interpretation.

## 0.3 Structure of Thesis

**Chapter 1** of this thesis highlights the main aspects related to the state of the art of NDT for the characterization of masonries, focusing on the GPR technique. Results from preliminary field investigations of the three selected test sites (Pyramid, Colosseum and Nymphaeum) were presented, underlining the differences in the GPR responses according to the different types of materials and antenna frequencies.

The theoretical principles of GPR techniques are reviewed in the **Chapter 2**, both analysing the propagation of electromagnetic waves in dielectric materials and the wave polarization, with particular regard to attenuation and lateral and vertical resolution.

In **Chapter 3** the electromagnetic modelling and simulation results are presented. In particular, a preliminary model composed by stone blocks containing a micro-pile was set up, evaluating the changes in the GPR response due to the interposition of a Plexiglas layer between the antenna and the sample. Then, the benefit of the Plexiglas interposition for fractures detection is assessed, through a simulation of a load test monitoring executed on small-sized tuff and bricks samples, later investigated in the laboratory (Chapter 4).

In **Chapter 4** materials and methods employed for investigation of the above mentioned samples are described together with the results achieved. GPR and ERT investigations are performed on both samples before and after the application of a diagonal compressive load and GPR data are analysed in terms of energy through time slices, and by means of maps of dielectric constant and of mean absolute amplitude. At the end the resistivity models, obtained with inversion of ERT data, are used to validate the GPR evidences.
Finally, the conclusions of the thesis (**Chapter 5**) point out how the integrated application of GPR and ERT investigations can be a reliable tool to monitor static load tests, due to the complete non-invasiveness, the cost-effectiveness and the high-resolution achieved by these methods giving also some focal points about the future challenges for researchers.

# 1. STATE OF THE ART

The high seismic vulnerability of the existing unreinforced masonry structures, highlighted by the recent earthquakes occurred in Central Italy in the last few decades (1997, 2002, 2009, 2012, 2016), calls for investigation of the existing masonry building and for understanding potential and limits of reinforcements applicable to the structures. Therefore, the application of geophysical non-destructive testing can be an important tool for assessing the current state of a masonry structure.

In light of this, geophysical methods were applied in order to detect and characterize structures without any damage (Gaffney, 2008 ). In particular in this thesis we explore the potential and limits of Ground Penetrating Radar (GPR) for these purposes. In fact, through this method a high-resolution image of the existent structures or important information about the location of buried bodies (voids, rebars, etc.) or fractures can be retrieved (Conyers, 2013).

Although the GPR is generally the most used and reliable technique for structural investigations, the integration of experimental data from different NDT methods is often employed in order to avoid interpretation ambiguities and pitfalls in the characterization of near-surface structures.

## 1.1 NDT for characterization of masonries

NDT techniques are generally based on different theoretical principles, and producing as a result different sets of information regarding the physical properties of the structure. These properties, such as compressional and shear wave velocities, electrical resistivity and so on, have to be interpreted in terms of the fabric of the structure and its engineering properties. Unavoidably, this interpretation involves some degree of assumption about the structure, so the use of calibration measurements is an essential feature of most non-destructive surveys. Furthermore, many structural problems will be best studied by a particular NDT method, depending upon which physical properties of the construction materials offer the best chance of being reliably determined (McCann & Forde, 2001).

There are five major factors, which need to be considered in the planning of a survey:

- the required depth of penetration into the structure;
- the vertical and lateral resolution required for the expected targets;

- the contrast in physical properties between the target and its surroundings;
- signal to noise ratio for the physical property measured at the structure under investigation;
- historical information concerning the methods used in the construction of the structure.

The NDT can be divided as a function of their different theoretical principles into five main groups:

- Seismic, sonic and ultrasonic methods
- Electromagnetic methods
- Electrical methods
- Infrared thermography
- Interferometry

Non-destructive **sonic and ultrasonic** testing methods have been used in the assessment of civil engineering structures and materials and they refer to the transmission and reflection of mechanical stress waves through a medium at sonic and ultrasonic frequencies.

The **seismic method** involves compressional waves at frequencies between 500 Hz and 10 kHz propagating within the wall (or the structure) under investigation, allowing a simple evaluation of the relative condition of the masonry or concrete walls of the structure or an evaluation of the internal fabric of a structure (Cardarelli, et al., 2002). This method has been successfully used to: evaluate the degree of material homogeneity, detect the presence of voids, estimate the depth of superficial cracks, and calculate an average compressive strength for the structure or the material (McCann & Forde, 2001). Through the **seismic tomography,** local variations in velocity can be identified and correlated with zones of weakness or flaws in the internal fabric of the structure. Several studies have used seismic tomography to image the internal structures of buildings, structures and ancient monuments (Cardarelli & De Nardis, 1998; Polymenakos et al., 2002; Orlando & Renzi, 2013; Orlando et al., 2015).

**The seismic reflection method** may be used for the investigation of retaining walls/wing walls/spandrel walls: internal dimensions and shape, type and properties of fill, voiding within the fill material and for cracks and voids within the internal fabric of the structure (McCann & Forde, 2001).

The most recent development of ultrasonic methods: the **impact–echo test method** is suitable for determining the thickness of concrete and reinforced concrete slabs accessible from one side, detecting defects (delamination, debonding, local flaws, cracks, etc.) in such slabs and floor toppings. The method is particularly suitable for checking the interlayer adhesion in floor toppings, checking the adhesion of repair layers to the base in various concrete and reinforced concrete elements, determining the depth of cracks, checking the filling of tendons with cement grout in post-tensioned concrete girders and the diagnostic testing of sewer mains (Sansalone & Street, 1997; Hoła et al., 2009).

The **ultrasonic reflection** method has been successfully used for identifying and locating specific flaws in concrete and it is also applicable to the investigation of small defects within masonry walls (Vasanelli et al., 2016).

The **Falling Weight Deflectometer** (**FWD**) is widely used for road evaluations, in order to assess the functional and structural conditions of road pavement sections either for purposes of routine monitoring or planned corrective action (Hadi & Preko, 2013).

Also the GPR technique has been focused on different types of applications on low traffic volume roads, both paved and gravel roads (Saarenketo & and Aho, 2005). The most important application of GPR in pavements is the determination of different layer thicknesses (Hadi & Preko, 2013).

Beyond the already mentioned **GPR** technique, that will be extensively presented in the next section, other electromagnetic techniques were employed for the structures analysis, as the conductivity measurements and the covermeter.

**Conductivity measurements** can be used to assess: the moisture content in the masonry; the salt content in the masonry associated with moisture content; the height of moisture capillary rise; to evaluate the thickness of the masonry wall; the multiple-wythe nature of the masonry wall; to determine the composite construction of the masonry structure; to individuate the presence of voids or in-homogeneities as well as the presence of metal reinforcements, pipes, drains etc. in the wall (Colla et al., 1997).

**Covermeters** are widely used for the non-destructive testing of concrete structures to determine if reinforcement bars are adequately covered with concrete and to infer the location of safe spots for drilling, for strengthening, for repair work and for refurbishing the structure (Fletcher & Woolhouse, 2012).

Another technique used in a fully non-destructive mode is the **electrical resistivity tomography (ERT)** method. The application of ERT into standing structures has become very popular in order to provide useful information about the hidden foundations and the surrounding geology and hydrogeology, and secondarily, to the externals structures, as long as non-invasive electrodes are used (Cardarelli et al., 2016). Furthermore, this geophysical technique was recently used on stone exposures (Sass, 2005) in an effort to understand the processes of weathering of stone and was also adopted for analysing rising damp phenomenon and assessing moisture content of historic walls (Mol & Preston, 2010; Sass & Viles, 2010). ERT can be complementary employed for understanding the resistive behaviour of the building materials, individuating possible defects or fractures, and validating the GPR evidences. Moreover, given the electrical conductivity of the structure from ERT, we can have a rough estimation of the intrinsic attenuation of the GPR signal, which is directly proportional to the conductivity. However, the main disadvantage of this technique is the rapid loss of resolution with depth, that makes the detection of a small deep target impractical.

The **half-cell potential** measurements can be performed on structures with ordinary or stainless steel reinforcement. The method can be applied regardless of the depth of concrete cover and the rebar size and detailing. The measurements indicate corroding rebar not only in the most external layers of reinforcement facing the reference electrode but also in greater depth (Elsener et al., 2003).

Buildings or structures with defects such as debonding render and mosaic or delaminating concrete emit differing amounts of *infrared radiation*. **Infrared thermography** (IRT) has met an extensive popularity among the non-destructive technologies for building diagnostics, especially with the increasing concerns of energy minimization and low energy consumption of the building sector. Its popularity for a broad range of applications can be attributed to its non-contact safe nature, its usefulness and effectiveness, as well as the energy and cost savings it can achieve (Kylili et al., 2014). Furthermore, thermography was applied in order to identify different materials and moisture content (Linan et al., 2015).

Usually, evolution of unstable structures is monitored by observing the cracks (or the entire building) with deflectometers and topographical measurements. Recently, SAR

based **interferometric techniques** have also received increasing interest (Tarchi et al., 2000; Pieraccini et al., 2001; 2002; 2004). These techniques are of little use for monitoring cracks in building, because deflectometer measurements monitor only particular types of cracks while topographical and SAR surveys can be applied when steady datum points are available near the building, which then provide only global information on building movement.

## 1.2 GPR for characterization of masonries

Ground Penetrating Radar (GPR) can provide important information about the location and the consistence of both buried and elevated structures. To these aims, GPR has been successfully applied during the last decades to detect and characterize ancient structures (Abbas et al., 2005; Orlando & Slob, 2009; among many others, and to search for Roman buildings (Neubauer et al., 2002; Piro et al., 2003). These studies demonstrated that the GPR method can be a useful tool for the detection of buried structures in the shallow subsurface as well as of cavities and hidden objects inside ancient structures, with the aim to assess the current state of the structure and give safety indications to the archaeologists (Orlando et al., 2014).

The GPR has been also developed large application to obtain information about modern structures, such as pavement and structures layer thickness (Al-Qadi & Lahouar, 2005; Orlando L. et al., 2016); changes in materials or degraded zones (Lorenzo & Cuéllar, 2001); changes in the water content (Grote et al., 2005); the existence of voids and anomalous elements (Grandjean et al., 2000); the location of reinforcing bars and metal elements in concrete bases or structures (Barrile & Pucinotti, 2005); and characterization of different constructive materials (Shaari et al., 2004).

GPR is also a useful technique for finding hidden characteristics in structures (Bungey, 2004). Voids, cracks, embedded elements or other anomalous bodies can be detected that would otherwise not be discovered except with destructive testing or other expensive and time-consuming techniques (Perez-Gracia et al., 2008).

The main advantages of GPR are: its fast data acquisition capability, its high resolving ability and the fact that it can individuate both metallic and nonmetallic targets. This features allow that the Ground-penetrating radar (GPR) is, arguably, the most popular,

broad-based geophysical technique for near-surface ground investigation due to its unrivalled ability to stratigraphically map large areas in relatively short times.

Although being a high-resolution technique, the GPR signal has the disadvantage of a lower depth of penetration in cases of conductive media (Daniels, 2009), a case that often occurs for structural applications due to the presence of rebars and similar metallic structures (e.g. reinforcements). However, a more common problem is related to the high overall conductivity of building materials like concrete and some types of bricks, as a consequence of the chemical composition of the constitutive materials. Furthermore, in many practical cases it is difficult to identify, with a sufficient degree of confidence, the effective presence of fractures (mainly vertical-directed), because the sample interval is often too large compared to the limited thickness of the fracture, employing common used frequencies. In addition to this, it is not always feasible to establish a biunivocal relationship between the GPR anomalies and the presence of a certain type of construction materials or of fractures, particularly for heterogeneous structures where different construction materials are combined together. By the way, the integration of different geophysical techniques can remove ambiguities on interpretation of geophysical models, increasing the degree of accuracy of the physical parameters reconstruction (Diamanti et al., 2005). Therefore, the benefit of the integration between GPR and ERT dataset for improving the interpretation of geophysical models still needs to be analysed. In fact, Electrical Resistivity Tomography (ERT) can be complementary employed for understanding the resistive behaviour of the construction materials, individuating possible defects or fractures and validating the GPR evidences.

Since the GPR response can change as a function of different types of construction materials related to different modern, historical or archaeological structures, this issue can affect the capability to correctly estimate the construction materials or to detect fractures, joints, reinforcements. In light of this, in the following sections, three tests performed in different test-sites during the thesis, are presented, in order to understand the main issues normally encountered in GPR survey of archeological structures.

## 1.3 Test sites

### ✓ 1.3.1 Pyramid of Caius Cestius (Rome)

The Pyramid of Caius Cestius is the only surviving monument of a series of similar buildings existing in Rome in the 1st century BC, when funerary architecture was influenced by the fashion that had arisen in Rome after the conquest of Egypt in 31 BC.

The structure, 36.4 m high with a square base of 29.5 m per side, is composed of a nucleus of concrete with a curtain of bricks (Fig. 1.1); the external cladding is made of Luni marble.

The barrel-vaulted burial chamber, of about 23 $m^2$, was walled up at the time of the entombment, after the Egyptian custom (Golubića et al., 2015).

The restoration of the burial chamber was executed by the Archaeological Authority of Rome in 2001. In 2011, further interventions were announced and, in November 2012 construction work began to erect the scaffolding needed to carry out the restoration of the Pyramid. The GPR investigation was performed simultaneously, in order to detect potential anomalies within the marble blocks and to investigate for the presence of other internal chambers.

We used a IDS GPR system equipped with 200, 600, 900 and 2000 MHz bipolar antennas, in order to evaluate the changes in the recorded dataset as a function of frequency. For the sake of simplicity, the GPR profile no. 1, placed at a height of 1.65 m from ground is shown (Fig. 1.1), as it is representative of the whole campaign performed at the site.


*Figure 1.1: Pyramid of Caius Cestius, where the GPR profile path, placed at 1.65 m from the ground level, is superimposed*

Dataset processing consisted in the time zero correction, a vertical band pass filter and a divergence compensation.

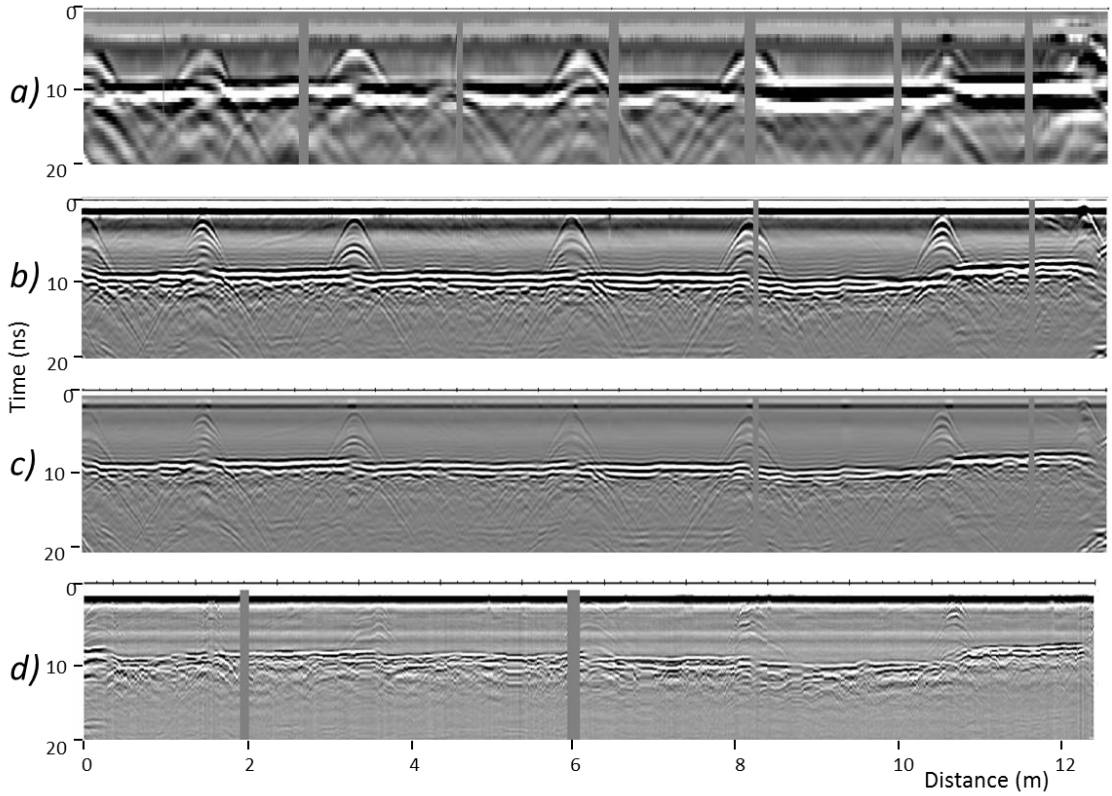


*Figure 1.2: GPR profiles acquired on the profile no. 1 in Fig. 1.1, using 200 (a), 600 (b), 900 (c) and 2000 MHz (d) antennas*

The GPR sections show (Fig. 1.2) enough horizontal and vertical resolution, in a way that it is possible to discriminate, for all frequencies, the interface between the marble blocks and the inner wall and the joints between two consecutive blocks (by the diffraction hyperbolae). The high resolution achieved is mainly due to the type of material, compact and homogeneous compared with the signal frequency, which allows an optimal coupling between antenna and surface, preventing scattering and undesired events, with a consequent optimal GPR signal penetration.

### ✓ 1.3.2 Passage of Commodus (Colosseum, Rome)

The Passage of Commodus was dug within the foundation of the Colosseum (Rome) under Emperor Domitian (81-96 AD). The passage is a radial-directed 4 m high and about 60 m long tunnel extended form the arena towards south, with a final part outside the foundation (Fig. 1.3). The floor elevation difference between the outer and the inner (arena) part of the passage is around 2.5 m. The ceilings are brick-made barrel vaults and both walls and ceilings were originally covered with a thick layer of mortar. However, over time the latter material has been partially removed and the walls nowadays have rough surfaces (La Regina, 2009).

A previous work where GPR data were acquired from the ground level (Orlando & Slob, 2009) detected the top of the vault of the Passage of Commodus at a depth of 1-1.5 m. Therefore, the floor level is located around 19 m a.s.l. in the inner zone, confirming the hypothesis made by Rea *et al.* (2002), and it was likely excavated within the foundation.

The aim of this survey is the characterization of the foundation of the Colosseum, still partially unknown in terms of building technique and material employed, by means of a GPR survey on the lateral walls of the Passage of Commodus. A secondary aim is the evaluation of the GPR response as a function of the frequency and the construction materials.

The GPR antennas were placed on the lateral walls of the Passage, at a height of 1.5 m from the floor level, operating at 200, 600 and 900 MHz, resulting on a 60 m long south-directed profile (C-D, Fig. 1.3).

Each profile was divided into two sub-profiles named C-Gate and Gate-D, due to the presence of a gate between them. Since these lines were executed at a fixed height of 1.5 m from the floor level, they are located at decreasing depth from the ground level due to the above mentioned slope of the floor.

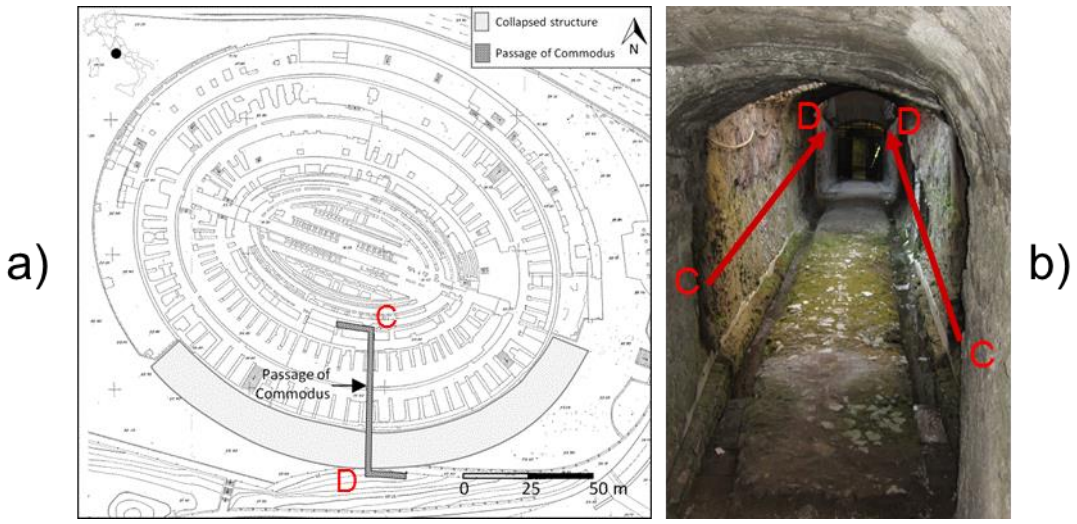


*Figure 1.3: Passage of Commodus within the Colosseum. a) Top view at the ground level where the location of the Passage of Commodus is superimposed. b) Image of the surveyed areas and location of the field GPR investigations.*

GPR dataset was processed through the standard procedure described above for the Pyramid. The propagation velocity of electromagnetic waves was inferred in 8 cm/ns from the diffraction hyperbola fitting on the wall (Conyers, 2013), and compared with that (7 cm/ns) obtained from Common Mid Points (CMP), acquired on the floor. Hence, a mean velocity value for the following interpretation of 7.5 cm/ns was used.

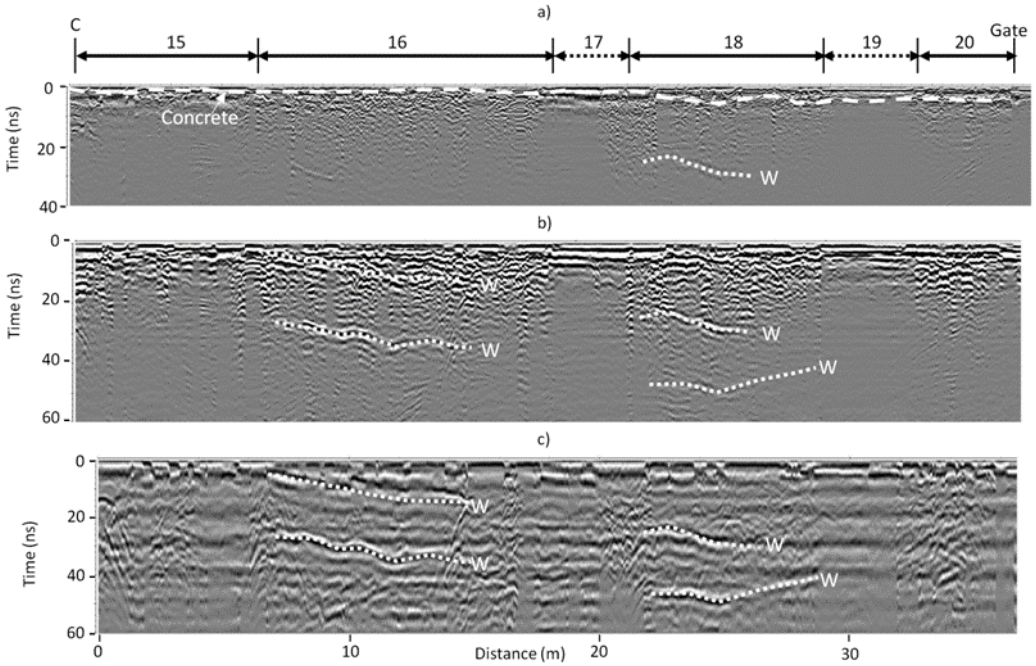


*Figure 1.4: GPR profiles acquired on the left wall along the C-Gate section in Fig. 1.3, using 900 (a), 600 (b) and 200 MHz (c) antennas. The white dotted lines with the capital letter "W",*

*represent the foundation elements, while the mortar/concrete discontinuity is marked with a dashed line.*

GPR dataset acquired on left wall along the C-Gate profile (Fig. 1.4) reaches a maximum lateral penetration of about 1.875 m (50 ns). Here we detect six different sub-sections labelled with no. 15-20. A shallow reflection (few nanoseconds) can be seen continuously along the line (white dotted line in Fig. 1.4), while it is deeper from 22 m to the end of the line. This reflection is probably due to the interface between the mortar covering the wall and the concrete of the foundation. The zones no. 15, 17 and 19 are characterized by a high attenuation that prevents any individuation of deeper anomalies. The reflections marked with W in Fig. 1.4 can be due to the extension of the pillars in depth, below the ground level.

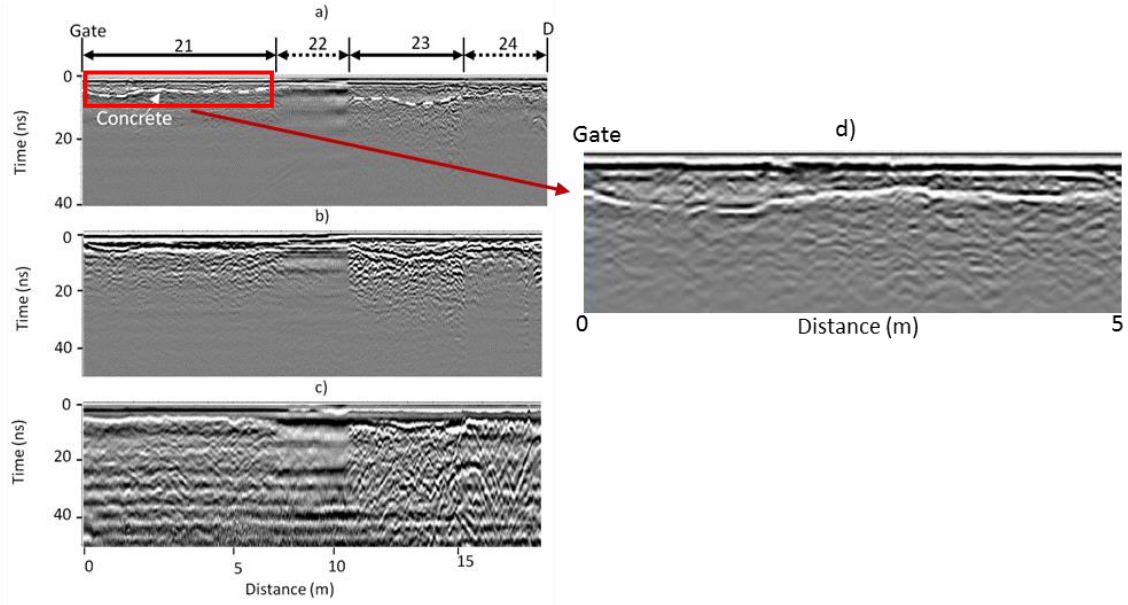


*Figure 1.5: GPR profiles acquired on the left wall along the Gate-D section in Fig. 1.3, using 900 (a), 600 (b) and 200 MHz (c) antennas. The white dashed line represents the mortar/concrete discontinuity. (d) Enlarged view of the area within the red rectangle*

The second GPR sub-profile (Gate-D) of the left wall (Fig. 1.5), is able to detect four different areas (no. 21-24), where zones no. 21, 22 and 24 are characterized by a strong signal attenuation. In this zone we cannot distinguish any clear reflection, but we can well discriminate the shallow mortar/concrete interface due to the covering (Fig.1.5d). The zone n. 23 displays a similar behaviour of the anomalies no. 16-18 in Fig. 1.4, as a consequence of the presence of a vertical discontinuity (dotted line), as seen before. The

sharp transition between zones no. 23 and 24 could be due to the interface between the foundation and the outer 3 m thick retaining wall of the foundation.

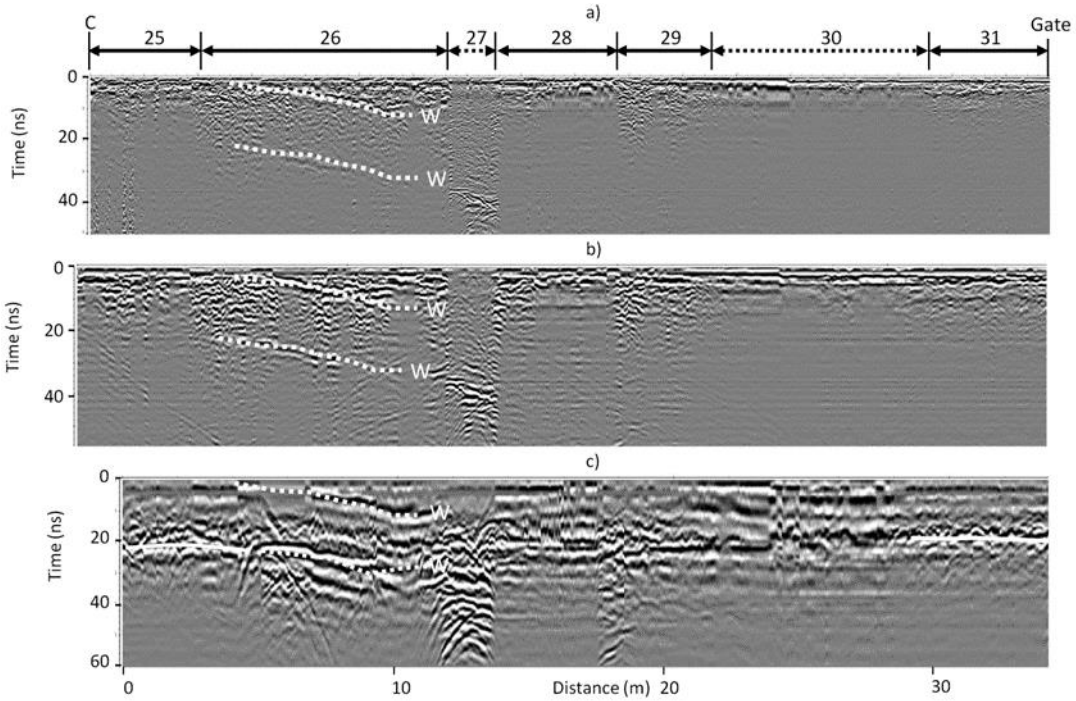


*Figure 1.6: GPR profiles acquired on the right wall along the C-Gate section in Fig. 1.3, using 900 (a), 600 (b) and 200 MHz (c) antennas. The white dotted lines with the capital letter "W" represent the foundation elements*

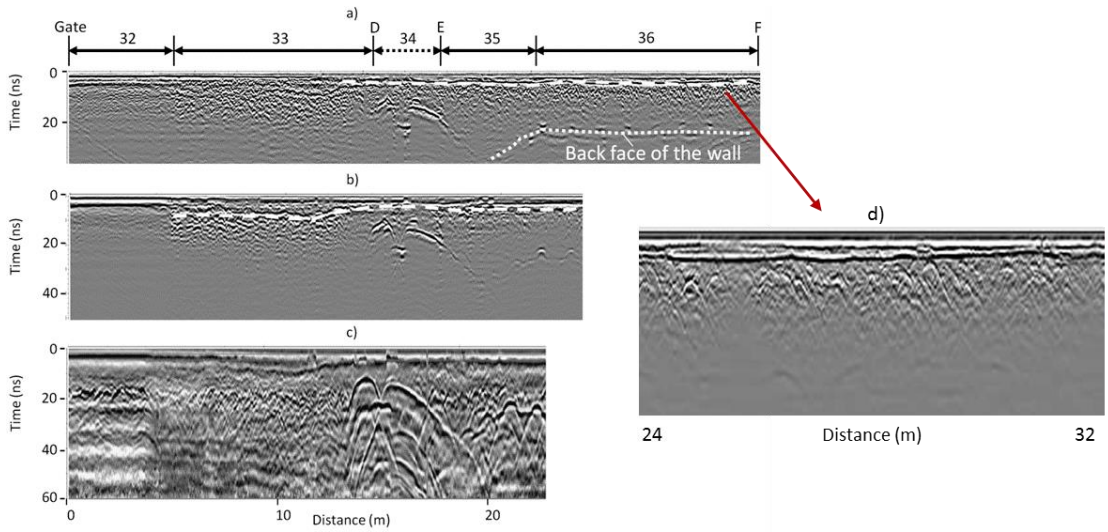


*Figure 1.7: GPR profiles acquired on the right wall along the Gate-D section in Fig. 1.3, using 900 (a), 600 (b) and 200 MHz (c) antennas. The white dotted lines represent the location of the back face of the wall, while the mortar/concrete discontinuity is marked with a dashed line (enlarged image in d)*

Figures 1.6 and 1.7 show the results of GPR investigation on the right wall of the passage. There is a better penetration in the first part of the passage than in the second one. Through the first sub-profile (C-Gate, Fig. 1.6), only reflections from one pillar are detected (zone no. 26), comparable to the evidences of Fig. 1.4 (no. 16). The low signal penetration in the remaining zones prevents the identification of clear anomalies, so the equivalent of the zone. n. 18 is not found on the right wall.

The GPR profile of Fig. 1.7 has been performed on the Gate-D sub-section and partially in the outer part of the passage (EF section), although only with the 900 MHz antenna. There is a good correspondence in terms of shape and position (about 50 cm laterally) between the reflection identified in zone no. 33 (white dotted line in Fig. 1.7) and the respective on the left wall (Fig. 1.5 no. 23). Then the DE segment (zone no. 34) depicts the external retaining wall of the foundation including the sewer (strong reflection at 25 ns). The zone no. 35 is on the sharp bend of the tunnel, while the zone no. 36 is related to the external part of the passage, parallel to the outside ring of the foundation. In this part the mortar-concrete discontinuity is well detected (Fig. 1.7d), On the rear face of the wall (reflection at 30 ns), equally-spaced (1.4 m) diffraction hyperbolas are present, maybe related to structural elements or to recent reinforcements of the passage. The calculated thickness of the wall outside the foundation is around 1 m.

Definitively, GPR response show that the foundation consists of laterally inhomogeneous materials. Some zones (no. 15-17-19 in Fig. 1.4, no. 21-22-24 in Fig. 1.5, no. 28-30 in Fig. 1.6 and no. 32 in Fig. 1.7) are characterized by a strongly attenuated signal, probably due to the high heterogeneity of the construction material. Instead, a higher signal penetration is shown in Fig. 1.5-1.6 where we clearly detect reflections resulting from the extension of the pillars in depth, and therefore characterized by a less attenuating material. This examples demonstrate that data interpretation can be difficult in cases where the signal penetration changes significantly depending on the type of material and on the surface roughness.

### ✓ 1.3.3 Colle Oppio (Rome)

In the following we report the performance of GPR in characterizing three different typologies of archaeological walls of Trajan and pre-Trajan age. The investigated walls

are located under the Cryptoporticus of the "Baths of Trajan", discovered during the latest archaeological campaign (2012) at the Colle Oppio (Rome historical centre), near the Domus Aurea complex, by the Sovrintendenza Comunale ai Beni Architettonici (Major of Rome-Authority of Cultural Heritage).

The three investigated walls, characterized by different types of materials are:

- the "Mosaics" wall (travertine) (Fig. 1.8a)
- the "Nymphaeum" wall (bricks) (Fig. 1.8b)
- the "Trajan" wall (*opus caementicium*) (Fig. 1.8c)

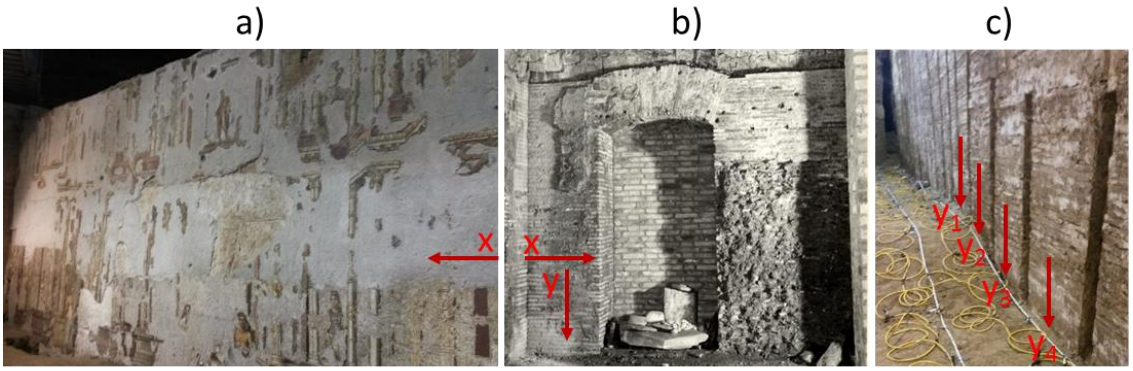


*Figure 1.8: The three investigated walls: a) "Mosaics" wall, b) "Nymphaeum" wall, c) "Trajan" wall*

Ground Penetrating Radar (GPR) was selected for reconstructing the inner geometry of the walls, as well as characterizing its building materials and its quality, with the additional purpose of mapping fractures in order to give safety indications, evaluating the electromagnetic response as a function of different materials, and the coupling between walls and antenna. Dataset was processed using the standard procedure described for the above mentioned examples.

- "Mosaics" wall

The radargrams obtained with 200, 600, 900 and 2000 MHz antennas are presented in Figs. 1.9. For the low frequency antennas (200-600 MHz) the air-wall interface is detected (around 20 ns), while a diffraction hyperbola (in the middle of the radargrams in Fig. 1.9) is probably due to a fracture within the wall. Through a time-depth conversion obtained by using an estimated velocity equal to 9 cm/ns, the thickness of the wall can be estimated in 0.9 m.

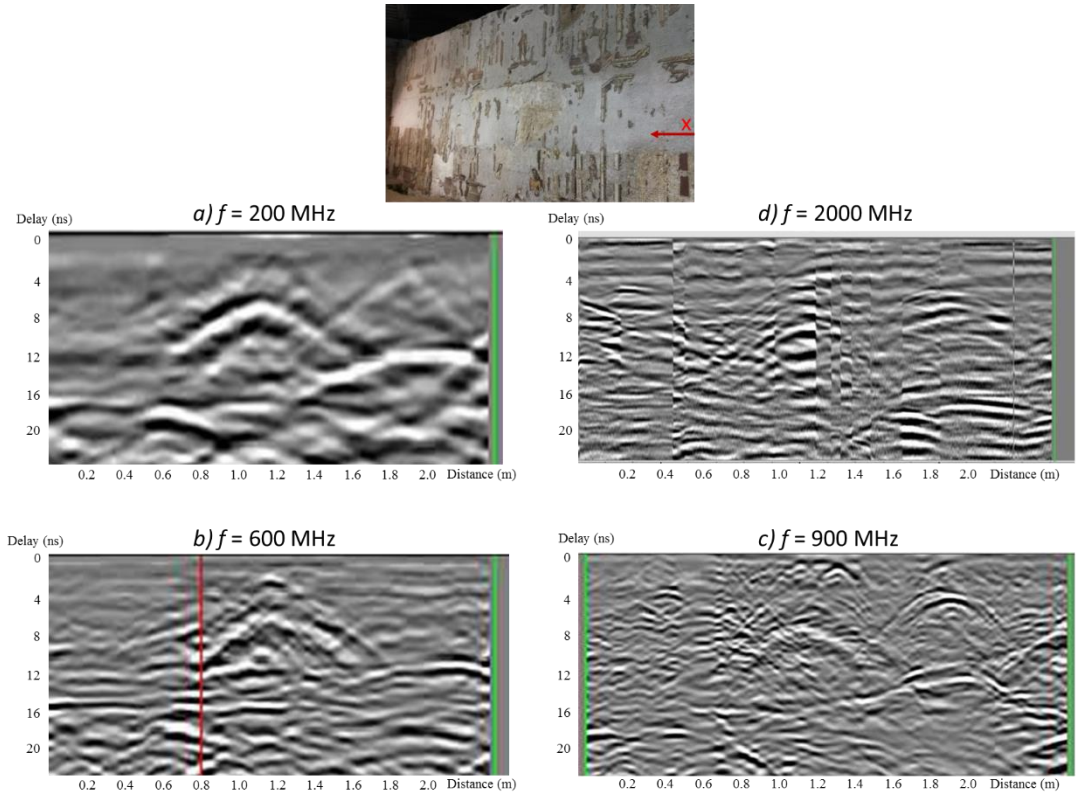


*Figure 1.9: GPR profiles acquired with different frequency antenna, relative to the "Mosaics" wall*

The 2000 MHz antenna in our opinion gives the best trade-off between resolution and depth of investigation, even though the radargram of Fig. 1.9d shows a non-optimal wall-antenna coupling due to the roughness of the surface with consequent limitations of the odometer, which leads to an underestimation of the profile length.

As the frequency increases, the resolution increases together with the scattering signal due to smaller objects, making difficult the interpretation of the 2 GHz radargram.

- "Nymphaeum" brick wall

In Fig. 1.10 we present the x-directed radargrams for the four different frequencies (200, 600, 900, 2000 MHz) acquired on the "Nymphaeum" wall, made of bricks.

Here the GPR signal is highly attenuated and strongly scattered, due to the high conductivity and small dimensions of the bricks, respectively. The high conductivity is due both to material forming the bricks and to the rising damp, clearly visible on the surface.

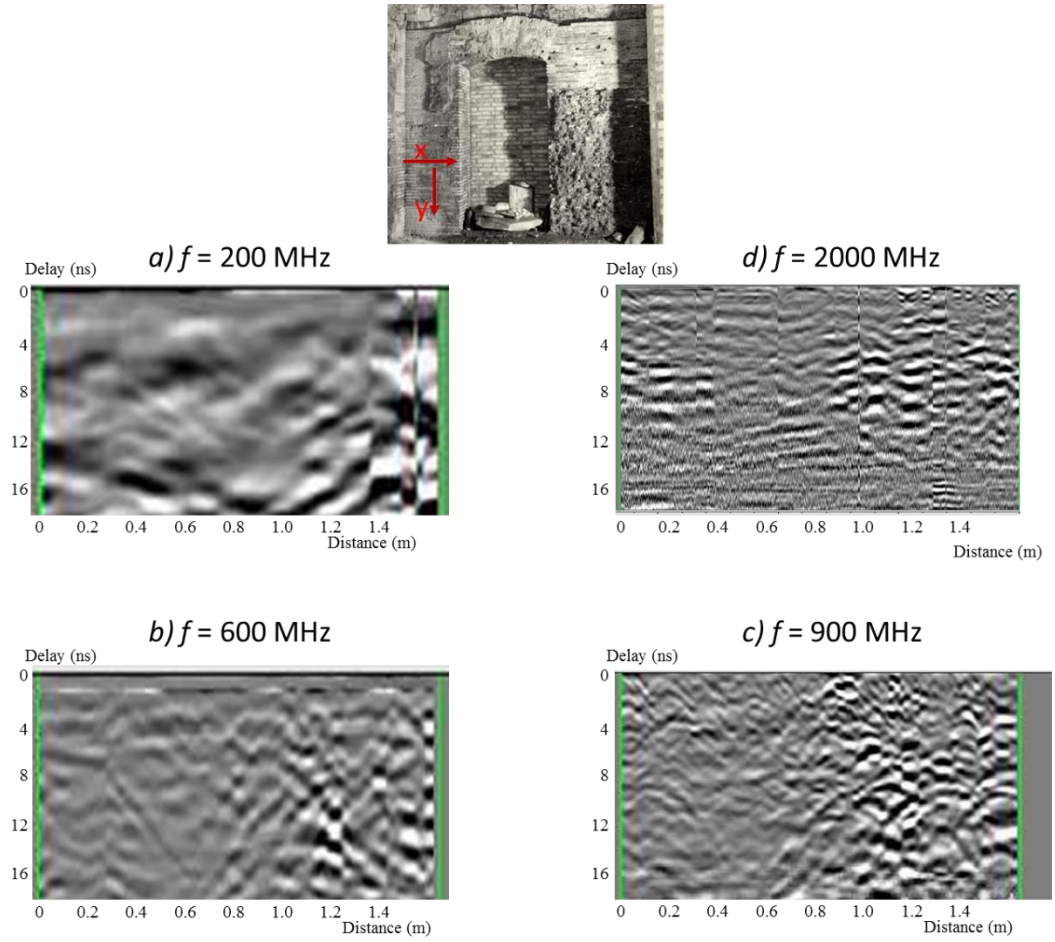


*Figure 1.10: GPR profiles acquired with different frequency antenna for the Nymphaeum wall*

- "Trajan" wall

On the Trajan wall (bricks) we acquired data on y-directed profiles, using the four frequencies seen in the previous case (Fig. 1.11).

Radargrams are not able to identify the rear wall-air interface, and consequently it was not possible to infer the effective thickness of the wall. In fact the high signal scattering and the high conductivity of material induce a higher signal attenuation in the shallower part of the wall (0-40 cm).

The lower frequency (200-600 MHz) profiles (Fig.1.11a,b) show a main diffraction hyperbolae and few other diffractions, probably related to the geometry of the wall, and a high degree of heterogeneity.

The high attenuation and the small size of the objects with respect to the frequency antenna are the main restrictions in the data interpretation, also in this case.

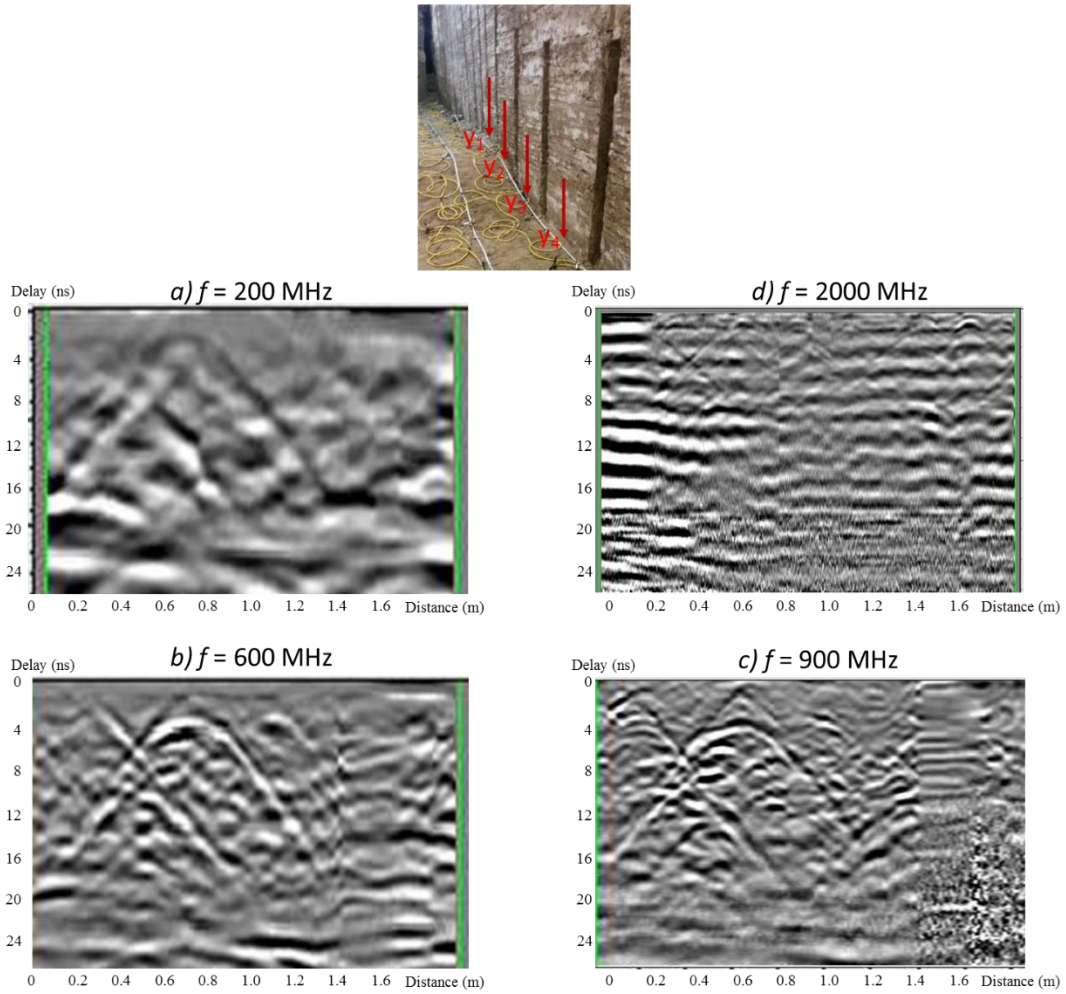


*Figure 1.11: GPR profiles acquired with different frequency antennas on the y1 path, relative to the bricks wall*

## 1.4 Concluding remarks

Field examples highlighted different GPR responses according to the different types of material and frequency antennas because the attenuation is directly correlated to the building material and resolution to antenna frequency and object dimension. In detail the case of the Pyramid, where wall blocks of compact and homogeneous material are investigated, represents the *optimum* with high resolution and signal penetration. On the contrary the Nymphaeum wall displays a more complex interpretation resulting from a non-optimal antenna-wall coupling and the roughness of the wall. Moreover, even by increasing the frequency, we do not have an evident increase of the resolution in the

superficial layer. Nevertheless, the frequency increase corresponds to a higher scattering for the smaller objects, making more complex the interpretation of GPR sections.

Starting from these considerations, in the following sections we aim to:

- evaluate an improve of GPR response in terms of horizontal and vertical resolution as a function of frequency of the antenna and the type of materials;
- improve the wall-antenna coupling particularly for rough surfaces;
- understand the detectability of critical elements (fractures, slackening, etc.) and of thicknesses and geometries of the masonry.

In light of this, the interposition, between the surface of the investigated medium and the GPR antenna of a dielectric material (e.g. Plexiglas) can theoretically improve the vertical resolution of the shallow subsurface, avoiding the direct wave overlapping, despite losing horizontal resolution. This add-on to the classical GPR system is evaluated in the following sections by means of synthetic models, based on simulations on small-scale masonry samples, for the evaluation of the possible benefit of this system and then of laboratory survey on the same samples, before and after the application of a combined shear-compression load.

# 2. GPR Theory

Maxwell's equations mathematically describe the physics of EM fields, while constitutive relationships quantify material properties. Combining the two provides the foundations for quantitatively describing GPR signals. In mathematical terms, EM fields and relationships are expressed as follows:

$$\overline{\nabla} \times \overline{E} = -\frac{\partial \overline{B}}{\partial t} \tag{2.1}$$

$$\overline{\nabla} \times \overline{H} = \bar{J} + \frac{\partial \overline{D}}{\partial t} \tag{2.2}$$

$$\overline{\nabla} \cdot \overline{D} = q \tag{2.3}$$

$$\overline{\nabla} \cdot \overline{B} = 0 \tag{2.4}$$

Where respectively:

- $\overline{E}$ is the electric field strength vector [V/m];
- q is the electric charge density [C/m$^3$];
- $\overline{B}$ is the magnetic flux density vector [T];
- $\bar{J}$ is the electric current density vector [A/m$^2$];
- $\overline{D}$ is the electric displacement vector ([C/m$^2$];
- t is time [s];
- $\overline{H}$ is the magnetic field intensity [A/m].

From these relationships, all classic EMs (induction, radio waves, resistivity, circuit theory, etc.) can be derived when combined with formalism to characterized material electric properties (Annan, 1996).

Constitutive relationships are the means of describing a material's response to EM fields. For GPR, the electrical and magnetic properties are of importance. The following constitutive equations provide a macroscopic (or average) description of how electrons, atoms, and molecules respond to the application of an EM field.

$$\overline{J} = \tilde{\sigma}\, \overline{E} \tag{2.5}$$

$$\overline{D} = \tilde{\varepsilon}\,\overline{E} \tag{2.6}$$

$$\overline{B} = \tilde{\mu}\,\overline{H} \tag{2.7}$$

Electrical conductivity $\tilde{\sigma}$ characterizes free charge movement when an electric field is present. Resistance to charge flow leads to energy dissipation. Dielectric permittivity $\tilde{\varepsilon}$ characterizes displacement of charge constrained in a material structure due to the presence of an electric field. Charge displacement (polarization) results in energy storage in the material. Magnetic permeability $\tilde{\mu}$ describes how intrinsic atomic and molecular magnetic moments respond to a magnetic field. For simple materials, distorting intrinsic magnetic moments store energy in the material. In the general case $\tilde{\sigma}$, $\tilde{\varepsilon}$, and $\tilde{\mu}$ are tensor quantities and can also be nonlinear (Jol H. M., 2009).

Material properties can also depend on the history of the incident field. Time history dependence manifests itself when the electrical charges in a structure have a finite response time, making them appear as fixed for slow rates of field change and free to move for faster rates of field change. To be fully correct, Equations (2.5), (2.6) and (2.7) should be expressed in the following form, relative to equation 2.5:

$$\bar{J}(t) = \int_0^{\infty} \tilde{\sigma}(\beta) \cdot \overline{E}\,(t-\beta)\,d\beta \tag{2.8}$$

This more complex form of the constitutive equations must be used when physical properties are dispersive. For most GPR applications, assuming the scalar constant form for μ, ε, σ suffices (Jol H. M., 2009).

For GPR, the relative dielectric permittivity or “dielectric constant” is used and defined as follow:

$$\varepsilon_r = \frac{\varepsilon}{\varepsilon_0} \tag{2.9}$$

Where $\varepsilon_0$ is the permittivity of vacuum equal to $8.89 \times 10^{-12}$F/m.

In most GPR applications, variations in $\varepsilon$ and σ are most important, while variations in μ are often negligible.

Earth materials are invariably composite of many materials or components, therefore understanding the physical properties of the mixture is a key factor in the interpretation of a GPR response. Mixture of materials seldom exhibit properties directly in proportion

to the volume fraction of the constitute components, that can make quantitative analysis of GPR data impossible without additional information.

## 2.1 Properties of materials

Many researchers have extensively studied the dielectric properties of earth materials and showed how the attenuation of electromagnetic radiation rises with frequency and, at a given frequency, wet materials exhibit a higher loss than dry ones. This is true for any material since higher frequency does mean more oscillations within a reference time and in turn higher attenuation.

These considerations are priority for understand how those characteristics of materials affect both the velocity of propagation and attenuation and therefore to optimize the performance of a surface-penetrating radar system.

An order of magnitude indication of the basic dielectric characteristics of various materials can be gauged from Table 2.1, which shows their conductivity and relative permittivity measured at a frequency of 100 MHz (Daniels, 2004).

| ***Material*** | ***Conductivity [S/m]*** | ***Relative permittivity*** |
|---|---|---|
| Air | 0 | 1 |
| Asphalt dry | $10^{-2} : 10^{-1}$ | $2 - 4$ |
| Asphalt wet | $10^{-3} : 10^{-1}$ | $6 - 12$ |
| Clay dry | $10^{-1} : 10^{-0}$ | $2 - 6$ |
| Clay wet | $10^{-1} : 10^{-0}$ | $5 - 40$ |
| Coal dry | $10^{-3} : 10^{-2}$ | 3.5 |
| Coal wet | $10^{-3} : 10^{-1}$ | 8 |
| Concrete dry | $10^{-3} : 10^{-2}$ | $4 - 10$ |
| Concrete wet | $10^{-2} : 10^{-1}$ | $10 - 20$ |
| Freshwater ice | $10^{-4} : 10^{-3}$ | 4 |
| Granite dry | $10^{-8} : 10^{-6}$ | 5 |
| Granite wet | $10^{-3} : 10^{-2}$ | 7 |
| Limestone dry | $10^{-8} : 10^{-6}$ | 7 |
| Limestone wet | $10^{-2} : 10^{-1}$ | 8 |
| Permafrost | $10^{-5} : 10^{-2}$ | $4 - 8$ |
| Rock salt dry | $10^{-4} : 10^{-2}$ | $4 - 7$ |
| Sand dry | $10^{-7} : 10^{-3}$ | $2 - 6$ |
| Sand wet | $10^{-3} : 10^{-2}$ | $10 - 30$ |
| Sandstone dry | $10^{-6} : 10^{-5}$ | $2 - 5$ |
| Sandstone wet | $10^{-4} : 10^{-2}$ | $5 - 10$ |
| Sea water | $10^{2}$ | 81 |
| Sea-water ice | $10^{-2} : 10^{-1}$ | $4 - 8$ |

| | | |
|---|---|---|
| Shale dry | $10^{-3} : 10^{-2}$ | $4 - 9$ |
| Shale saturated | $10^{-3} : 10^{-1}$ | $9 - 16$ |
| Snow firn | $10^{-6} : 10^{-5}$ | $6 - 12$ |
| Soil clay dry | $10^{-2} : 10^{-1}$ | $4 - 10$ |
| Soil clay wet | $10^{-3} : 10^{-0}$ | $10 - 30$ |
| Soil loamy dry | $10^{-4} : 10^{-3}$ | $4 - 10$ |
| Soil loamy wet | $10^{-2} : 10^{-1}$ | $10 - 30$ |
| Soil sandy dry | $10^{-4} : 10^{-2}$ | $4 - 10$ |
| Soil sandy wet | $10^{-2} : 10^{-1}$ | $10 - 30$ |

*Tab. 2.1: Typical range of dielectric characteristics of various materials measured at 100 MHz (Daniels, 2004)*

At low microwave frequencies, including the range over which surface-penetrating radar systems operate, water has a relative permittivity of ~80, the solid constituents of most soils and man-made materials have, when dry, a relative dielectric constant $\varepsilon_r$ in the range 2 to 9. When they are "partially water saturated", such as for the building materials, the measured values of $\varepsilon_r$ lie mainly in the range 4 to 40. Hence the relative permittivity of a material, and therefore the velocity of propagation, is firstly depended upon its water content. The absolute permittivity also varies with frequency, but is generally sensibly constant for most materials over the range of frequencies utilised for surface-penetrating radar work (Daniels, 2004).

The physical models which are used to predict the propagation of electromagnetic waves in dielectric materials have two main sources: electromagnetic wave theory and geometrical optics. The latter method is only relevant when the wavelength of the electromagnetic radiation employed is considerably shorter than the dimensions of the object or medium being illuminated and when the materials involved can be considered to be electrical insulators. Optical theory is therefore most relevant to dry materials. Materials containing appreciable amounts of moisture will behave as conducting dielectrics, especially if the water contains ions, and the variability of material parameters and local geological conditions that could be encountered in real life cause great difficulty in accurate prediction of propagation behaviour (Daniels, 2004).

## 2.2 Propagation of electromagnetic waves in dielectric materials

In free space the magnetic susceptibility and electric permittivity are constants; that is, they are independent of frequency and the medium is not dispersive. In a perfect dielectric

(free space) no propagation losses are encountered and hence there is no consideration of the attenuation, which occurs in real dielectric media.

Plane waves are good approximations to real waves in many practical situations, such as in low loss and resistive media, while more complicated electromagnetic wave fronts can be considered as a superimposition of plane waves.

Electromagnetic wave propagation can be represented by a one-dimensional wave equation of the following form, with propagation along the z-axis and perpendicular electric *(E)* and magnetic *(H)* fields as shown in Figure 2.1.

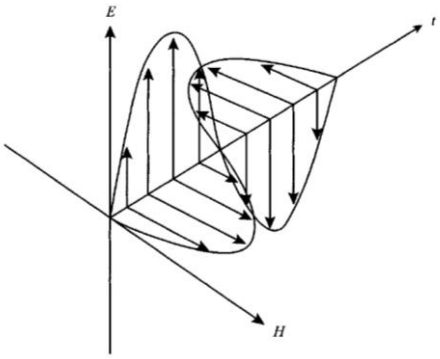


*Figure 2.1: Propagation of electromagnetic waves in free space (Daniels, 2004)*

Where the velocity of propagation is:

$$v = \frac{1}{\sqrt{\varepsilon \cdot \mu}} \tag{2.10}$$

The velocity of light in free space is:

$$c = \frac{1}{\sqrt{\varepsilon_0 \cdot \mu_0}} \tag{2.11}$$

Hence,

$$v = \frac{c}{\sqrt{\varepsilon_r}} \tag{2.12}$$

With:

- absolute magnetic susceptibility of free space, $\mu_0 = 1.26 \times 10^{-6}$ Hm$^{-1}$
- absolute magnetic susceptibility of medium, $\mu = \mu_0 \mu_r$
- $\mu_0$ is relative magnetic susceptibility, being 1 for nonmagnetic geologic materials.

The intrinsic impedance (the ratio of the electric to the magnetic field) of the medium is:

$$\eta = \sqrt{\frac{\mu}{\varepsilon}} \tag{2.13}$$

In the case of a perfect dielectric, the wave propagating in the positive z-direction can be described as:

$$E(z) = E_0 e^{-jkz} \tag{2.14}$$

Where the phase constant, known as the wave number, describes the change in phase per unit length for each wave component and it may be considered as a constant of the medium for a particular frequency:

$$k = \frac{\omega}{v} = \omega\sqrt{\mu\varepsilon}\, m^{-1} \tag{2.15}$$

The wavelength, λ, is defined as the distance the wave propagates in one period of oscillation:

$$k\lambda = 2\pi \tag{2.16}$$

Hence:

$$\lambda = \frac{2\pi}{\omega\sqrt{\mu\varepsilon}} = \frac{v}{f} \tag{2.17}$$

This is the common relationship between wavelength, phase velocity and frequency.
In optics it is common to utilise a refractive index, $\eta$, given by:

$$\eta = \frac{c}{v} = \sqrt{\mu_r \varepsilon_r} \tag{2.18}$$

With $\mu_r = 1$ and $\eta = \sqrt{\varepsilon_r}$ for the frequency being considered.
Electromagnetic waves propagating through natural media experience losses, causes attenuation of the original electromagnetic wave, both to the electric *(E)* and magnetic *(H)* fields. For most materials of interest in surface-penetrating radar the magnetic response is weak and need not be considered as a complex quantity, unlike the permittivity and conductivity (Daniels, 2004).
For dielectrically lossy materials, with a complex conductivity and permittivity (but non-complex magnetic permeability), a real effective conductivity and real effective permittivity can be used in place of the specific constituent parameters (King & Smith, 1981), where:

- Complex permittivity

$$\underline{\varepsilon^*} = \underline{\varepsilon'} + j\underline{\varepsilon''} \tag{2.19}$$

- Complex conductivity

$$\sigma^* = \sigma' + j\sigma'' \tag{2.20}$$

- Real effective permittivity

$$\underline{\varepsilon}^{\mathrm{e}} = \underline{\varepsilon}' - \frac{\sigma''}{\omega} \tag{2.21}$$

- Real effective conductivity

$$\sigma^{\mathrm{e}} = \sigma' + \omega\underline{\varepsilon}'' \tag{2.22}$$

These effective parameters describe the combined EM energy loss and storage mechanism of conductivity/permittivity relaxation and represent currents that are either in phase ($\sigma^{\mathrm{e}}$) or out phase ($\underline{\varepsilon}^{\mathrm{e}}$) with the electric field during the polarization and relaxation processes. These parameters are usually determined during experimental measurements (Turner & Siggins, 1994; Cassidy, 2007) and can be inserted in the velocity and attenuation equations to determine the true velocity and attenuation characteristics of the lossy materials at any given frequency. In most cases the conductivity component is considered independent of frequency, real-valued and relates only to the ionic conductivity of internal fluids and/or the surface charge conductivity of clay minerals. As such the two components can be combined to give a complex effective permittivity expression that describes the total loss and storage effects of the material as a whole (Reynolds, 1997).

$$\underline{\varepsilon_e}^* = \underline{\varepsilon}' - j\left[\underline{\varepsilon}'' + \frac{\sigma_s}{\omega\underline{\varepsilon_0}}\right] \tag{2.23}$$

Where:

- $\sigma_s$ is the bulk static (DC) conductivity of the material [S/m]

If we consider a single-frequency, linearly polarized, EM plane wave traveling in the z direction in a lossy medium, we can derive, from Maxwell's equations, the following expressions for the complex electric E and magnetic B field vectors:

$$E(z,t) = E_0 e^{-\alpha z} e^{i(\omega t - \beta z)} \tag{2.24}$$

$$B(z,t) = B_0 e^{-\alpha z} e^{i(\omega t - \beta z)} \tag{2.25}$$

Where $E_0$ and $B_0$ are the initial complex amplitudes, ω is the angular frequency, while the first exponential function is the attenuation term and the second the propagation term. From the first exponential function it is seen that at a distance $z = 1/\alpha$ the attenuation is *1/e.* This distance is known as the *skin depth*, $\delta$, and provides a rough indication of the penetration depth of a surface-penetrating radar system. Another useful parameter is the loss tangent or *loss factor* P.

$$\text{a)} \quad P = \left(\frac{\sigma' + \omega\underline{\varepsilon}''}{\omega\underline{\varepsilon}' - \sigma''}\right) \qquad \text{and} \qquad \text{b)} \quad \delta = \frac{1}{\alpha} \tag{2.26}$$

These practically useful parameters help us to assess how "lossy" a lossy dielectric is and, therefore, they can provide a guide to the physical effect of attenuation on the GPR wave. The skin depth $\delta$ is the distance (m) that a plane wave has to travel before its amplitude has reduced by factor of 1/e, approximately 37% (Reynolds, 1997). It is helpful in evaluating the penetration distance of GPR waves and the likely amplitude of any reflections (Jol H. M., 2009).

However, there are a number of other factors which influence the effective penetration depth, notably the strength of reflection from the target sought and the degree of clutter suppression of which the system is capable. These may reduce the calculated performance and must also be considered.

Instead, the loss factor can be used as a limiting expression for the appropriateness of low-loss assumptions and describes the ratio of EM energy loss factor $\left(\sigma' + \omega\underline{\varepsilon}''\right)$ to energy storage $\left(\omega\underline{\varepsilon}' - \sigma''\right)$. For low conductivity materials, this will be much less than 1 and the loss factor can then be approximated (Daniels, 1996) to:

$$P \cong \left(\frac{\sigma'}{\omega\underline{\varepsilon}'}\right) \tag{2.27}$$

For GPR applications the most important parameters are the attenuation and the velocity of wave propagation.

In the case of conducting dielectric the phase constant is complex and it is:

$$k = \omega\sqrt{\mu(\varepsilon' - j\varepsilon'')} \tag{2.28}$$

Through the separation of the wave number into real and imaginary parts:

$$jk = \alpha + j\beta = j\omega\sqrt{\mu\varepsilon'\left(1 - j\frac{\varepsilon''}{\varepsilon'}\right)} \tag{2.29}$$

And it is possible obtain the following expression for the attenuation factor $\alpha$ and for the phase constant $\beta$, by relating them to $\sigma$ and j$\omega\varepsilon$*:*

$$\alpha = \omega \sqrt{\left[\frac{\mu\varepsilon'}{2}\sqrt{1+\left(\frac{\varepsilon''}{\varepsilon'}\right)^2}-1\right]} \tag{2.30}$$

$$\beta = \omega \sqrt{\left[\frac{\mu\varepsilon'}{2}\sqrt{1+\left(\frac{\varepsilon''}{\varepsilon'}\right)^2}+1\right]} \tag{2.31}$$

The dimension factor $\varepsilon''/\varepsilon'$ is more commonly termed the material loss tangent.

The attenuation constant of a material is, to a first order, linearly related (in dB/m) to frequency. In the case of a dry material and relatively lossless, it may be reasonable to consider that tan $\delta$ is constant over that frequency range $1.10^7$ to $1.10^{10}$ Hz. However, for wet materials and lossy such an approximation is invalid, as:

$$\tan\delta = \frac{\sigma' + \omega\varepsilon''}{\omega\varepsilon' - \sigma''} \tag{2.32}$$

In general for lossy earth materials $\tan\delta$ is large at low frequencies, and increases to a maximum at several GHz, remaining constant thereafter.

The complex dielectric constant and the loss factor of a soil are affected by both temperature and water content. The general effect of increasing the temperature is to reduce the frequency of the dielectric relaxation, while increasing the water content also increases the value of the loss factor while shifting its peak frequency down (Daniels, 2004).

Tan $\delta$ can increase with frequency over the range $1 \times 10^8$ to $1 \times 10^{10}$ Hz as the dipolar losses associated with the water content of the material become more significant and the conductivity losses reduce.

$$\tan\delta = \text{conductivity losses} + \text{dipolar losses}$$

$$\tan\delta = \frac{\sigma_{dc}}{\omega\varepsilon_0\varepsilon_r} + \frac{\varepsilon''}{\varepsilon'} \tag{2.33}$$

For low values of $\sigma$ an indication of the order of magnitude can be obtained:

$$\tan\delta \approx \frac{\sigma'}{\omega\varepsilon'} \tag{2.34}$$

A graph of dielectric losses for a medium loss soil in Figure 2.2 is showed, with an accuracy limited to that frequency range. However, it gives a good insight into the wideband characteristics of soils. A graph of attenuation versus frequency for such a material is shown in Figure 2.3 (Daniels, 2004).

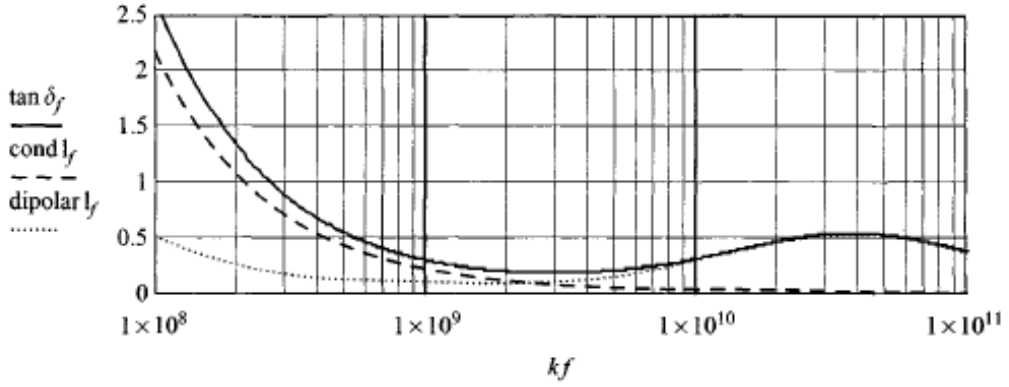


*Figure 2.2: Dielectric losses as a function of frequency in Hz for a medium loss soil (Daniels, 2004)*

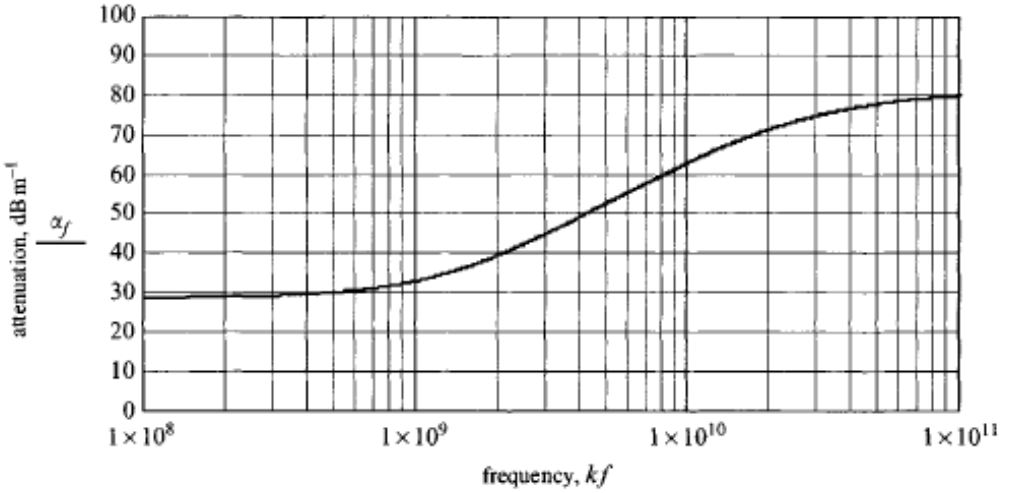


*Figure 2.3: Material attenuation as a function of frequency for a medium loss soil (Daniels, 2004)*

The velocity of propagation is also slowed by an increase of loss tangent, as well as relative dielectric constant:

$$v = c\left[\frac{\varepsilon'_e}{2\varepsilon_0}\left(\sqrt{(1+tan^2\delta)}+1\right)\right]^{\frac{1}{2}} \tag{2.35}$$

However, $\tan\delta$ must be significantly greater than 1 for any slowing to occur, and it is reasonable to assume that for $\tan\delta < 1$ (Daniels, 2004):

$$v = \frac{c}{\sqrt{\varepsilon_r}} \tag{2.36}$$

It can easily be recognized that if the propagation velocity can be measured, or derived, an absolute measurement of depth or thickness can be made. For homogeneous and isotropic materials, if the dielectric constant is known, the relative propagation velocity can be calculated from the previous relation (2.36) and the depth so calculated:

$$d = v\frac{t}{2} \tag{2.37}$$

where *t* is the transit time to and from the target.

In most practical cases the relative permittivity will be unknown, therefore the velocity of propagation must be measured in situ, estimated by means of direct measurement of the depth to a physical interface or target (i.e. by trial holing), or by calculation by means of multiple measurements.

## 2.3 EM Wave polarization

Key wave field properties are velocity, *v*, attenuation α, and EM impedance η (Z) (Annan, 2003). Wave properties for a homogeneous and isotropic medium with fixed permittivity, conductivity and permeability are most easily expressed if a sinusoidal frequency (*f*) are shown in Figure 2.4.

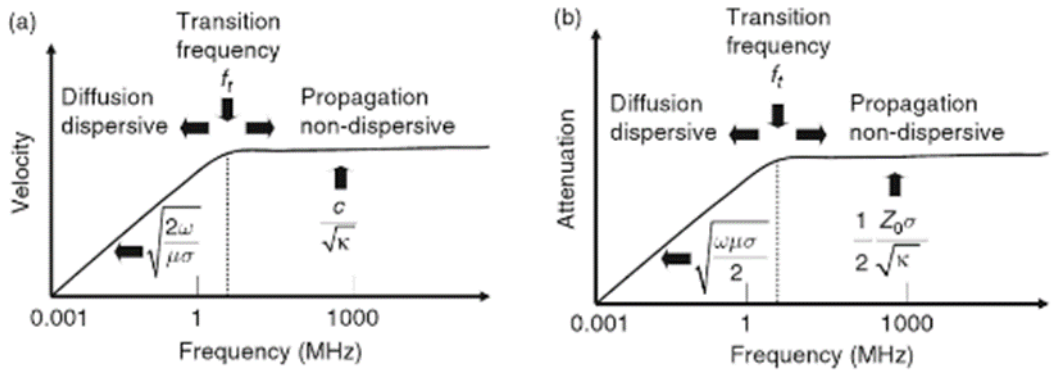


*Figure 2.4: Variation in velocity and attenuation in a simple medium with non-dispersive physical properties. c and Zo ($\eta_o$) are the velocity and impedance of free space (Annan, 2003). k does mean epsilon in this figure (Jol H. M., 2009)*

All the wave properties have similar behaviour: at low frequencies, the wave properties indicate a diffusive field behaviour; at high frequencies, the properties become frequency-independent (i.e. the material is not dispersive). The transition from the two behaviour occurs when the electric currents change from conduction-dominant to displacement

current-dominant behaviour (Annan, 1996). For a simple material the transition frequency is equal to:

$$f_t = \frac{\sigma}{2\pi\varepsilon} \tag{2.38}$$

Above $f_t$, in the high frequency plateau, all frequency components travel at the same phase velocity and suffer the same attenuation, and an impulsive signal will travel without dispersion, maintaining the intact shape (Annan, 1996). Hence, the velocity, attenuation and impedance can be expressed as:

$$v = \frac{1}{\sqrt{\mu\varepsilon}} = \frac{c}{\sqrt{\varepsilon_r}} \tag{2.39}$$

$$\alpha = \sqrt{\frac{\mu}{\varepsilon}} \cdot \frac{\sigma}{2} = \eta_0 \cdot \frac{\sigma}{2 \cdot \sqrt{\varepsilon_r}} \tag{2.40}$$

$$\eta = \sqrt{\frac{\mu}{\varepsilon}} = \frac{\eta_0}{\sqrt{\varepsilon_r}} \tag{2.41}$$

Under the hypothesis of negligible magnetic properties variations: $\mu = \mu_0 = 1.25 \times 10^{-6} H/m$ and with the impedance of free space $\eta_0$ equal to:

$$\eta_0(\Omega) = \sqrt{\frac{\mu_0}{\varepsilon_0}} = 377 \tag{2.42}$$

The "GPR plateau" normally exhibits a gradual increase in velocity and attenuation with frequency, because of the water adsorbs more strongly energy with frequency increases (in the 10-20 GHz range (Hasted, 1972)) and also because scattering losses are extremely higher frequency-dependent (Jol H. M., 2009).

### ✓ 2.3.1 GPR source near an interface

Generally, GPR is conducted with the source on the ground, where the transmitted signal divides into two parts, a spherical wave and a planar wave-front traveling at the critical angle, which links the direct spherical air wave and the spherical ground wave. Near the interface, the spherical ground wave extends into the air as an evanescent field.

The various wave fields are clearly separate in space and time when distances from the source are large compared to the wavelength or the pulse spatial length. For short distances from the source, the separation of the events becomes blurred but the essential concepts are valid.

Energy radiated from a surface antenna generates a strong electromagnetic field around the antenna within a radius of about 1.5 wavelengths of the center frequency. Within this

zone, coupling of the radar energy is occurring with the ground, generating and advancing wave front of propagating waves in the standard conical transmission pattern. About 1.5 wave-lengths of a standard dipole antenna is technically "part of antenna" in that no radiation is occurring within this zone and therefore technically no waves propagation. This near-field zone is usually visible in GPR profiles as a region of little or few reflections beginning at the ground surface and continuing to some depths. In the GPR literature this zone is sometimes incorrectly called near surface zone of interface. For the 10, 100 and 1000 MHz antennas, the near-field zones are approximately 30, 3 and 0.3 m, respectively, but vary depending on the down-loaded frequency (Conyers, 2013).

If low-frequency antennas are used, the near-field zone where few significant reflections are generated can be between 2.5 and 5 m of the ground surface, losing the information of eventual target located within the near-field zone and therefore a higher-frequency antenna should be used.

Due to the wide band-width of radar transmission, some high frequency (shorter-wavelenght) energy will still be generated even from a lower-frequency antenna, which will couple with the ground at a much shallower depth, and some shallow reflections can still be generated and visible in profiles within what is broadly defined as the near-field zone. If these reflections are high enough in amplitude, they will still appear as weak reflections within the otherwise reflection-free near-surface layer. Some subtle reflections in the near-field may never be noticeable in standard two-dimensional profiles but can become visible after the data are processed to produce amplitude slice maps (Conyers, 2013).

### ✓ 2.3.2 Reflected, refracted and transmitted waves

In any estimation of received signal amplitude it is necessary to consider the coefficients of reflection and transmission as the wave passes through the dielectric to the target. The Fresnel reflection and transmission coefficients quantify how the amplitudes of the EM fields vary across an interface between two materials (Jackson, 1962; Born & Wolf, 1980), as depicted in Figure 2.5.

Vector-field EM waves separate into two independent components, transverse electric field (TE) and transverse magnetic field (TM), defined by field orientation with respect to the boundary.

The incident (I), reflected (R) and transmitted (T) field strengths are related by the following equation:

$$I + R \cdot I = T \cdot I \tag{2.43}$$

Where R and I are determined by requiring Snell's law to be satisfied, the electric and magnetic fields in the plane of the interface to be continuous, and the electric current and magnetic flux density crossing the interface must be equal on both sides (Jol H. M., 2009).

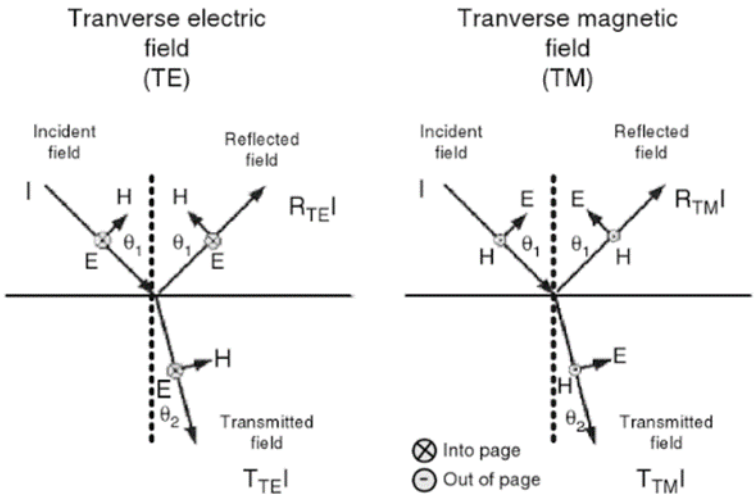


*Figure 2.5: EM waves are transverse vector waves field. Transverse Electric (TE): electric field in the interface plane; Transverse Magnetic (TM): magnetic field vector in the interface plane (Jol H. , 1995)*

According to the Snell's law also the direction of travel changes, such as:

$$\frac{\sin\theta_1}{v_1} = \frac{\sin\theta_2}{v_2} \tag{2.44}$$

At the boundary between two media, a part of the energy will be reflected and the remainder transmitted. The reflected field strength is described, in the case of vertical incidence, by the reflection coefficient, *r:*

$$r = \frac{\eta_2 - \eta_1}{\eta_2 + \eta_1} \tag{2.45}$$

Where $\eta_1$ and $\eta_2$ are the impedances of medium 1 and 2 respectively.

In a non-conducting medium and when considering only a single frequency of radiation, the above expression may be simplified and rewritten as:

$$r = \frac{\sqrt{\varepsilon_{r2}} - \sqrt{\varepsilon_{r1}}}{\sqrt{\varepsilon_{r2}} + \sqrt{\varepsilon_{r1}}} \tag{2.46}$$

Where $\varepsilon_{r1}$ and $\varepsilon_{r2}$ are the relative permittivity of the medium 1 and 2, respectively.

The reflection coefficient has a positive value when $\varepsilon_{r2} > \varepsilon_{r1}$ such as, where an air-filled void exists in a dielectric material. The effect on a pulse waveform is to change the phase of the reflected wavelet so that targets with different relative dielectric constants to the host material show different phase patterns of the reflected signal. However, the amplitude of the reflected signal is affected by the propagation dielectric of the host material, the geometric characteristics of the target and its dielectric parameters (Daniels, 2004).

### ✓ 2.3.3 Polarization: linear, elliptical, circular

According to the IEEE Standard Definitions for Antennas (Balanis, 2005), the polarization of a radiated wave is defined as *"that property of a radiated electromagnetic wave describing the time-varying direction and relative magnitude of the electric field vector; specifically, the figure traced as a function of time by the extremity of the vector at a fixed location in space, and the sense in which it is traced, as observed along the direction of propagation."* In other words, polarization is the curve traced out, at a given observation point as a function of time, by the end point of the arrow representing the instantaneous electric field (Balanis, 2012). The field must be observed along the direction of propagation. A typical trace as a function of time is shown in Figure 2.6.

An infinite number of polarizations exits, but the most common may be classified into three categories: linear, circular, and elliptical. If the vector that describes the electric field at a point in space as a function of time is always directed along a line, which is normal to the direction of propagation, the field is said to be linearly polarized. In general, however, the figure that the electric field traces is an ellipse, and the field is said to be elliptically polarized. Linear and circular polarizations are special cases of elliptical, and they can be obtained when the ellipse becomes a straight line or a circle, respectively.

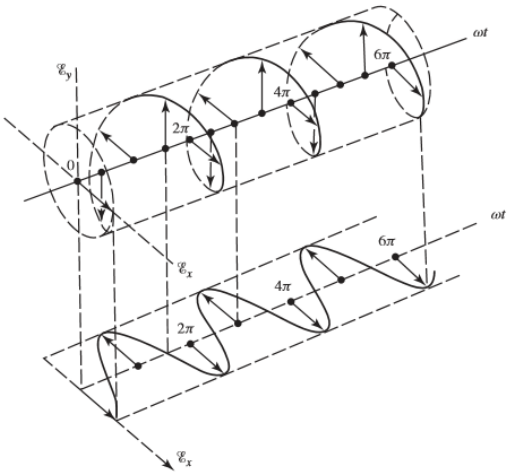


*Figure 2.6: Rotation of a plane electromagnetic wave at z =0 as a function of time (Balanis, 2005)*

The figure of the electric field is traced in a clockwise (CW) or counterclockwise (CCW) sense. Clockwise rotation of the electric field vector is also designated as right-hand polarization and counterclockwise as left-hand polarization (Balanis, 2012). In Figure 2.7 the figure traced by the extremity of the time-varying field vector for linear, circular, and elliptical polarizations are showed.

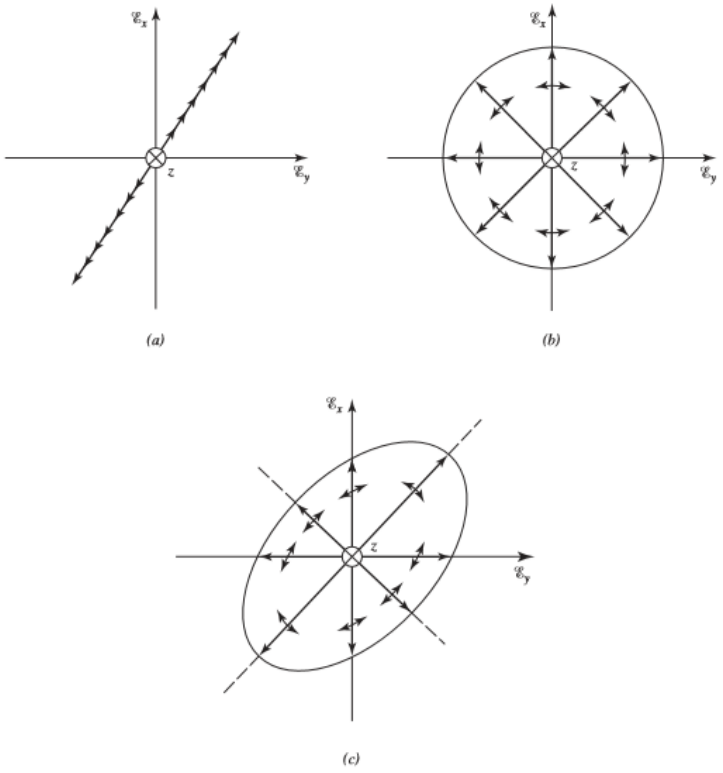


*Figure 2.7: Polarization figure traces of an electric field extremity as a function of time for a fixed position. (a) Linear. (b) Circular. (c) Elliptical.*

Where target is, for example, a planar surface, the linear polarization is the choice for the system designer. However, where the target is a linear like buried pipe or cable, then the backscatter field exhibits a polarization characteristic, which is independent of the state of polarization of the incident field. For linear targets, it is possible to use orthogonally disposed transmit and receive antennas as a means of preferential detection. Essentially the received signal varies sinusoidally with angle between antenna pair and target.
Definitely, the choice of polarization-dependent schemes should thus be considered very carefully as it may not be possible to cover all possible sizes of targets with just one antenna/polarization scheme (Daniels, 2004).

## 2.4 GPR survey

Before starting a geophysical survey there are several factors must be considered. The selection of a range of frequency operations, a particular modulation scheme, and the type of antenna and its polarization depends on a number of factors, including the size and shape of the target, the transmission properties of the intervening medium, and the operational requirements defined by the economics of the survey operation, as well as the characteristics of the surface. The specification of a particular type of system can be prepared by examining the various factors which influence detectivity and resolution.
To operate successfully, GPR must achieve (Daniels, 2004):

- an adequate signal to clutter ratio;
- an adequate signal to noise ratio;
- an adequate spatial resolution of the target;
- an adequate depth resolution of the target.

A GPR system comprises several main components: a signal generator, transmitting and receiving antennae, data digitizer, computer and a display module (Fig. 2.8).
The timing unit controls the generation and detection of signals. Most GPRs operate in the time domain; however, frequency domain measurements are now being used to synthetize the time domain response.

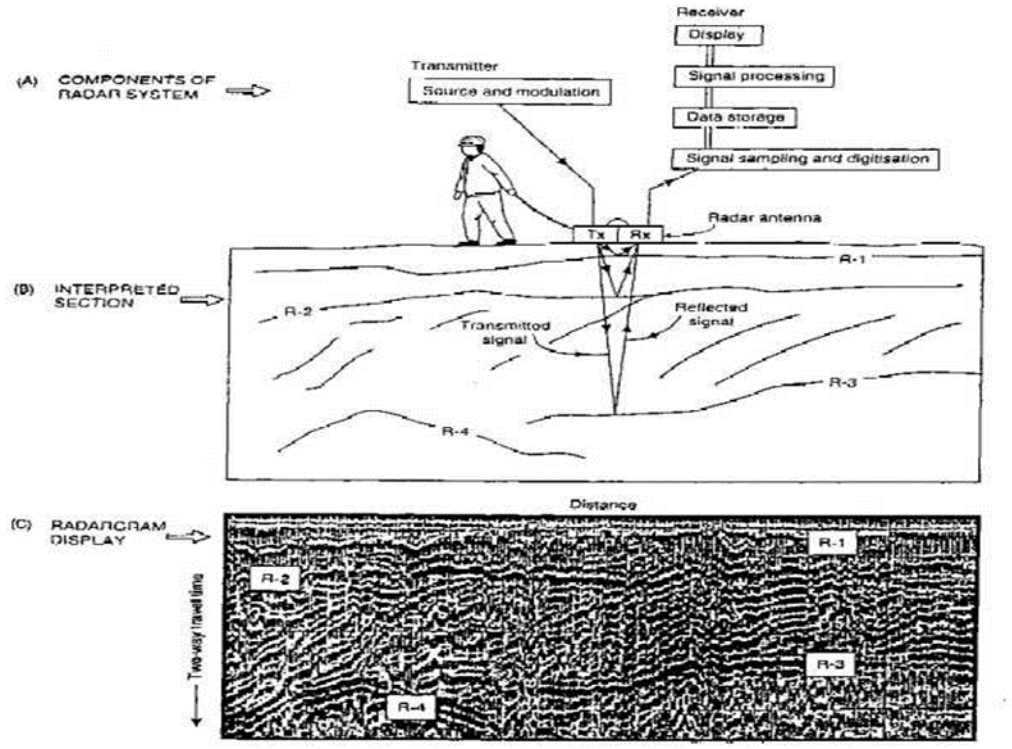


*Figure 2.8: Simplified diagram of (A) the constituent of a radar diagram (B) with the interpreted section (C). Adapted from Butler et al. (1991) and Daniels et al. 1988 (Reynolds, 1997)*

GPR fall in three categories, reflection profiling (using either monostatic and bistatic system); wide angle reflection and refraction (WARR) or common-midpoint (CMP) sounding; and transillumination or radar tomography (Reynolds, 1997).

Geophysical reflection data are of four main types: common offset, common mid (or depth) point, common source and common receiver Fig. 2.9.

Common-offset surveys (Fig. 2.9a) are the most frequently used in GPR studies, with commercial radar systems consisting of either a single transmitting and receiving antenna (monostatic) or two, separate, transmitting and receiving antennae (bistatic). In the latter systems, a fixed spacing (offset) is employed between the antennae, typically with both orientated in the same direction (i.e. copolarised). The antenna pair is moved over the surface, with the measured travel times to radar reflectors being displayed on the vertical axis while the distance the antenna has travelled is shown on the horizontal axis (Neal, 2004).

The WARR antenna configuration scheme is shown in Figure 2.9c. The transmitter is kept at fixed location and the receiver is towed at increasing offset. The location of WARR sounding should be over an area where the principal reflectors are planar and

either horizontal or dipping only at very shallow angles. It is also assumed that the material properties are uniform and that the reflector characteristics are the same over the sub-surface area on which the WARR sounding is undertaken. This assumption may not be true in all cases, and to avoid to make this assumption, a valid alternative is the common midpoint (CMP) sounding (Fig. 2.9b). In this case, both the transmitter and receiver are moved away from each other so that the midpoint between them stayed at fixed location. Therefore, the point of reflection on each sub-surface reflector is used at each offset, and thus areal consistency at depth is not a requirement (Reynolds, 1997). Two benefits are that the CMP stacking can improve signal-to-noise ratio (Fisher et al., 1992) and that a fully velocity cross section can be derived (Greaves et al., 1996).

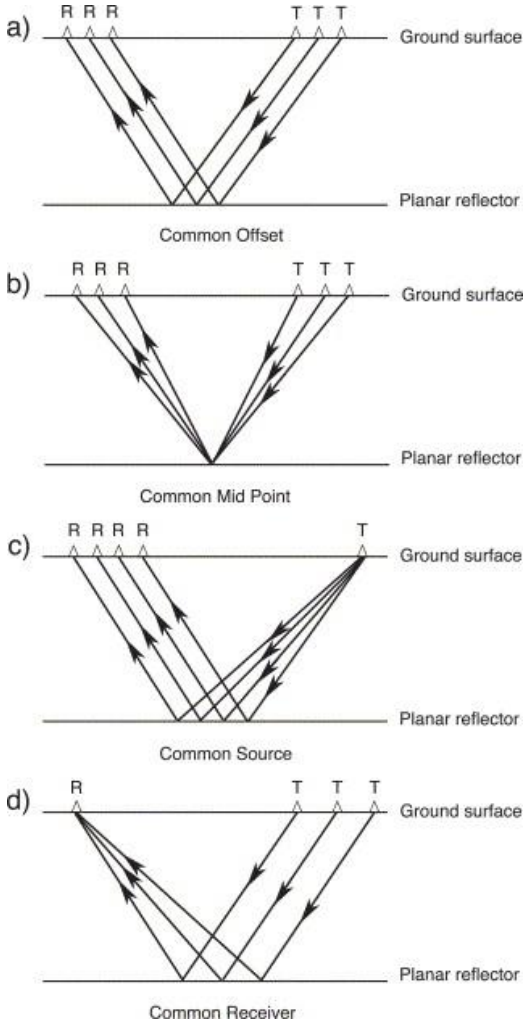


*Figure 2.9: The four main types of geophysical reflection survey. T=transmitter, R=receiver. Modified from Daniels (1996)*

The transillumination mode of deployment is where the transmitter and receiver are on opposite sides of the medium under investigation. The method is used underground within

mines, for example, where the transmitter is located in one gallery and the receiver is either in a gallery to one side of the transmitter, or in a gallery above or below. Alternatively, the radar antennae can be located down boreholes and the radar signals are then propagated from one, through the medium in between, to the other. The transillumination mode is also common in non-destructive testing (NDT) investigations of man-made structures, particularly using very high frequency and hence small antennae (e.g. 900 MHz centre frequency). Examples include testing concrete columns and masonry pillars (Reynolds, 1997).

During surveying, antennae are either dragged along the ground and horizontal distances recorded on a time-base, which can be converted to a distance-base through manual marking, or they are moved in a stepwise manner at fixed horizontal intervals (the 'step size') in order to obtain a better antenna-ground coupling.

GPR systems have the ability to collect data through two different modalities:

- continuously (continuous mode): the GPR pulses are continuously acquired at regular time intervals while an operator drags the antennas along the profile at a constant speed.
- for points (step mode): the progress is discontinuously conducted and for every step a track is recorded.

Step-mode operation generates more coherent and higher amplitude reflections, as antennae are stationary during data acquisition. This allows more consistent coupling between antennae and the ground, with the added benefit of better trace stacking (Annan & Davis, 1992).

As data are recorded during surveying, several subsequent traces build up a radar reflection profile. Each trace results from the GPR system emitting a short pulse of high-frequency electromagnetic energy, typically in the MHz range, that is transmitted into the ground. As the electromagnetic wave propagates downwards it experiences materials of differing electrical properties, which alter its velocity. If velocity changes are abrupt with respect to the dominant radar wavelength, some energy is reflected back to the surface. The reflected signal is detected by the receiving antenna. In systems with a single antenna, it switches rapidly from transmission to reception. The time between transmission, reflection and reception is referred to as two-way travel time (TWT) and is measured in nanoseconds ($10^{-9}$ s). Reflector TWT is a function of its depth, the antenna spacing (in

systems with two antennae), and the average radar-wave velocity in the overlying material (Neal, 2004).

Reflections from subsurface discontinuities are not the only signals recorded on a radar trace. The first pulse to arrive is the airwave (Fig. 2.10), which travels from transmit to receive antenna at the speed of light (0.2998 m/ns). The second arrival is the ground wave (Fig. 2.10), which travels directly through the ground between the transmit and receive antennae. The air and ground waves mask any primary reflections in the upper most part of a radar reflection profile. Lateral waves can also be present (Fig. 2.10) and result from shallow reflections that approach the surface at the appropriate critical angle and are subsequently refracted along the air–ground interface (Clough, 1976). It should be noted that reflections associated with lateral waves are not correctly placed in time (depth) with respect to the interface that generated them (Neal, 2004).

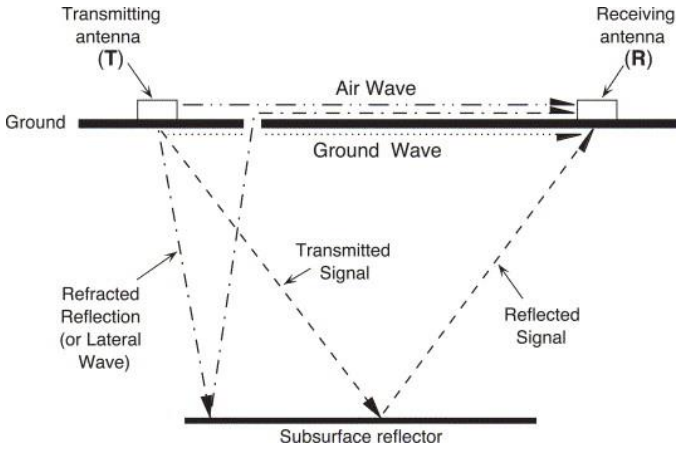


*Figure 2.10: Ray paths between transmitting and receiving antenna for the airwave, the ground wave, a lateral wave and a reflected wave. Modified from Fisher et al. (1996)*

### ✓ 2.4.1 Resolution

GPR signals propagating through complicated media encounter heterogeneous electrical and magnetic properties at many different scales. The heterogeneities can capture the energy and scatter it in all directions, often generating weak or undetectable responses (Annan, 2005, 2009). The most suitable antenna frequency is chosen by taking into account the desired lateral and vertical resolution, the target depth and the electromagnetic properties of the materials. The effectiveness of a GPR investigation, depends on the interaction of many factors that are often not simple to analyse. An important factor is the relation of the signal frequency to the dimension and shape of the target, and the heterogeneity of the hosting material.

The complexities associated with the interaction between waves radiating from dipole antennas placed near a dielectric half-space and the electrical heterogeneities within the dielectric medium often assume the far field approximation to model propagation phenomena.

As an antenna emits a broad band of frequencies, it is possible that, during signal propagation, a fraction of the high-frequency energy is diffracted and a fraction of the low-frequency energy is reflected, depending on the size, shape and orientation of the buried target (Balanis, 1989; Daniels et al., 1988; Knapp, 1991; Radzevicius and Daniels, 2000). Moreover, the re-emitted energy also depends on the incident energy (which is controlled by the transmitter power, directivity and distance away). In most civil engineering cases the host material is heterogeneous and the backscattered energy fall into the Rayleigh and resonance regions (Mie), depending on the dominant wavelength of the pulse. In this case, the amount of scattered energy can change rapidly with the signal wavelength for a given target. The inappropriate choice of antenna frequency may reduce the ability to detect the target.

The ability of a radar to resolve between two closely spaced targets in terms of position and geometrical attribute, is called resolution.

The resolution is normally divided into two components, namely vertical or radial and lateral or angular resolutions (Yilmaz, 2001), both of which are controlled by the signal wavelength, as depicted in Fig. 2.11.

Considering a system that generates a pulse, the consequently reflections may arrive simultaneously, overlap or separated in time. Pulses are clearly visible when $T >> W$ (Fig. 2.12), while are not distinguishable when $T << W$. Otherwise, two pulses are said to be distinguishable until $T \approx W$.

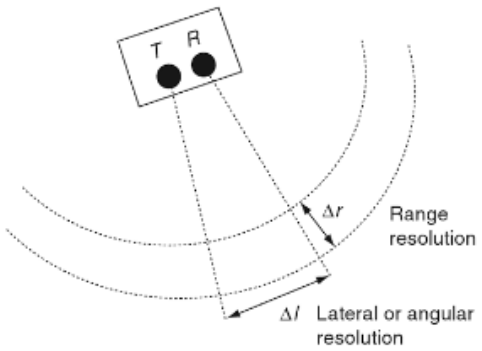


*Figure 2.11: Resolution of Ground Penetrating Radar: Range resolution and lateral resolution (Jol H. M., 2009).*

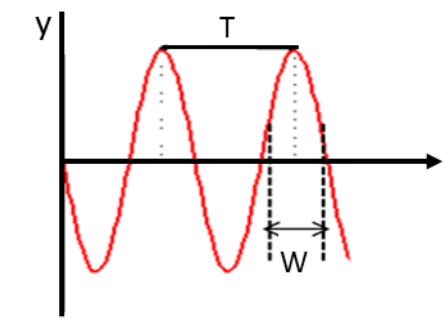


*Figure 2.12: Temporal pulse with half width W, in the case of two pulses clearly separable: T >> W*

The radial resolution length is expressed as:

$$\Delta r \geq \frac{\tau_p v}{4} = \frac{W}{4} \tag{2.47}$$

The pulse width and the velocity in the material dictate resolution length, while it is independent from the distance from the source.

The vertical resolution is controlled by the dominant wavelength (λ) of the signal and defines how close two layers can be vertically distinguished.

$$\lambda = \frac{v}{f} \tag{2.48}$$

Generally, the threshold for vertical resolution is a quarter of the dominant wavelength (λ/4). With equal bandwidth, resolution increases upon increasing the dominant frequency. In real applications the resolution also depends on data noise.

Lateral resolution refers to how close two reflecting points must be separated horizontally to be detected as follows:

$$\Delta l \geq \sqrt{\frac{vrW}{2}} \tag{2.49}$$

where r is the distance to the target.

The lateral resolution depends on the velocity, the pulse width, as well as the distance from the system.

This resolution depends on the first Fresnel zone radius (Fr), given by:

$$Fr \cong \sqrt{(\left(h + \frac{\lambda}{4}\right)^2 - h^2)} \tag{2.50}$$

where λ is the wavelength, and h is the depth of the target (Yilmaz, 2001).

With GPR, the pulse width W, in time is directly related to the bandwidth, B, which is also directly related to the center frequency, $f_c$ (Jol H. M., 2009), hence:

$$W = \frac{1}{B} = \frac{1}{f\mathrm{c}} \tag{2.51}$$

Considering that the center frequency wavelength is:

$$\lambda_c = \frac{f\mathrm{c}}{v} \tag{2.52}$$

Therefore the lateral resolution length can be expressed with the following relation:

$$\Delta l = \sqrt{\frac{\lambda_c h}{2}} \tag{2.53}$$

Lateral resolution decreases with increasing depth, and therefore the depth of the target is also important in the choice of antenna frequency. In civil engineering applications, the target is often not far from the measurement point, and the condition $\lambda << h$ is not fulfilled.

### ✓ 2.4.2 Scattering

GPR are invariably transmitted through complicated media since they encounter heterogeneous electrical and magnetic properties at different scales. Smaller-scale heterogeneities generate weak responses but their presence has an impact on the signals as they pass by. The heterogeneities extract energy as the EM field passes and scatter it in all directions.

Figure 2.13 show the scattering from an energy viewpoint.

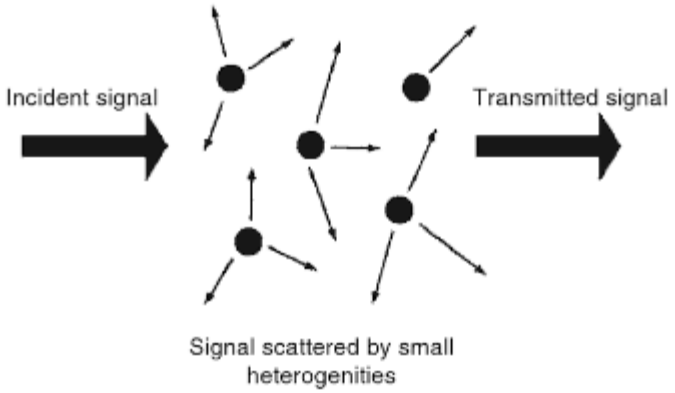


*Figure 2.13: Ground penetrating radar (GPR) signals are scattered by heterogeneities in material properties, which reduce the transmitted signals (Jol, 2009)*

On a wavefront, the incident signal with power per unit area impinges any point on local, small-scale scatters, which are characterized by spatial size, a, and number per unit volume, N (Jol H. , 1995).

The electric or magnetic fields are attenuated with a scattering attenuation coefficient $\alpha_s$ (Annan, 2005), namely the electric field decreases with distance r as:

$$\mathrm{E} = E_0 e^{-\alpha_s r} \tag{2.54}$$

Where:

$$\alpha_s = \frac{NA}{2} \tag{2.55}$$

And A is the scattering cross section, which in relation to the small scatters the Rayleigh scattering cross section of a pulse is:

$$\mathrm{A} = Ca^6 f^4 \tag{2.56}$$

Where C is the constant with units of $1/\mathrm{m}^4\ \mathrm{Hz}^4$, $a$ is the sphere radius, and f is the frequency.

Therefore the scattering attenuation is highly frequency-depending.

In order to determinate the full attenuation, scattering must be added to the ohmic or material loss attenuation, the GPR signal will see as it travels through a heterogeneous lossy dielectric medium (Jol H. M., 2009).

$$\alpha_{total} = \alpha_{ohmic} + \alpha_{scattering} \tag{2.57}$$

The effect of volume scattering was recognized as a limiting factor in temperate ice sounding, resulting more important in ice because the ohmic attention is much smaller than in most soil and rock materials (Watts & England, 1976).

In order to increase the resolution, the frequency of the generated EM pulse must be increased. Whereas, in order to increase the depth of investigation, occur choose lower frequency antennas, and therefore longer wavelengths. But this choice comes at the expense of the image resolution of the medium investigated.

As far as the experiments in the laboratory conducted on small-sized samples are concerned, since it is not necessary to reach high depth, using high frequency antennas is certainly the best choice. However, the main objective is rather to obtain high-resolution images of the investigated medium and therefore in order to minimize the noise and eventual external interference the use of shielded antennas was considered.

# 3. ELECTROMAGNETIC MODELLING AND SIMULATIONS

## 3.1 Introduction

The inability of interpreting GPR data quantitatively is partly due on the lack of understanding of how they have been created (i.e., understanding of the complex interactions between electromagnetic fields and targets), as well as on the lack of advanced processing tools that can process GPR data beyond the simple filtering procedures employed by most users. In order to improve our ability to understand GPR data, we need more sophisticated tools and a better understanding of the physical phenomena occurring in the subsurface.

GPR modelling plays a central role in advancing our understanding of GPR, as well as providing the means for testing new data processing techniques and interpretation software, giving researchers the opportunity to numerically "experiment" with GPR on their computers without incurring a substantial cost by creating expensive physical models, at least at an initial stage of a project. Simulating what if scenarios can save money and time providing data to support project proposals that could employ GPR.

Alternatively, a number of different analyses can be carried out to determine which result most closely resembles the field results obtained from a survey to evaluate the size or properties of the feature under investigation.

In the past few years, advanced GPR processing, modelling and interpretation methods have lead to more sophisticated approaches to data analysis and the ability to 'extract' material property information from the GPR sections, such as water content, porosity, etc. (Galagedara et al., 2005, Reppert et al., 2000).

In particular, as regards of the structures, numerical modelling have been applied in order to simulate a full and a hollow pier reinforced with iron bars and a pier with an oblique fracture (Orlando et al., 2009), for studying models of nonhomogeneous building walls (Honcharenko & Bertoni, 1994), for analyse the attenuation in brick and double reinforced concrete walls (Pena et al., 2003), to modelling the propagation of a radar signal through concrete (Shaari et al., 2004), etc.

For the GPR forward modeling, the method of moments (MoM) and, more specifically, the finite-difference time-domain (FDTD) technique have become the most popular simulation tools with both approaches being used to replicate practical near-surface GPR surveys in arrange of environments (Cassidy, 2007a; Giannopoulos, 2009).

The choice of the finite difference time-domain (FDTD) method lies in some its peculiarity, such as: its ease of implementation in a computer program and its good scalability when compared with other popular electromagnetic modelling methods such the finite-element and integral techniques (Millard et al., 1998). The main drawbacks of the FDTD technique are: the need to discretize the volume of the problem space, which could lead to excessive computer memory requirements and the staircase representation of curved interfaces.

In this study, the application of the FDTD technique for GPR wave propagation modeling is presented.

## 3.2 FDTD method

As extensively treated by Giannopoulos (2005), the finite difference time-domain (FDTD) method is a numerical technique for solving Maxwell's equations expressed in differential form. The method, introduced by Yee (1966), is very general and applicable to a wide range of electromagnetic problems. The basis of the FDTD method is the use of a central difference approximation for the evaluation of the partial derivatives of the governing differential equations.

To obtain the FDTD solution to a given problem, both space and time are discretized. Space is modeled as a grid constructed of "Yee cells" in which the components of the electromagnetic field vectors are located in a manner suitable for the implementation of a central difference approximation to Maxwell's equations. The 3D Yee cell is illustrated in Fig. 3.1.

The 2D FDTD cell is easily obtained as a simplification of the 3D Yee cell. The direction of wave propagation and of the magnetic field vector *H* have now been generalized to lie anywhere in the *x*-*z* plane. The field configuration for this 2D model is of the transverse magnetic (TM) mode and the reduced set of Maxwell's equations involves only the *Ey*, *Hx*, and *Hz* components of the electromagnetic fields.

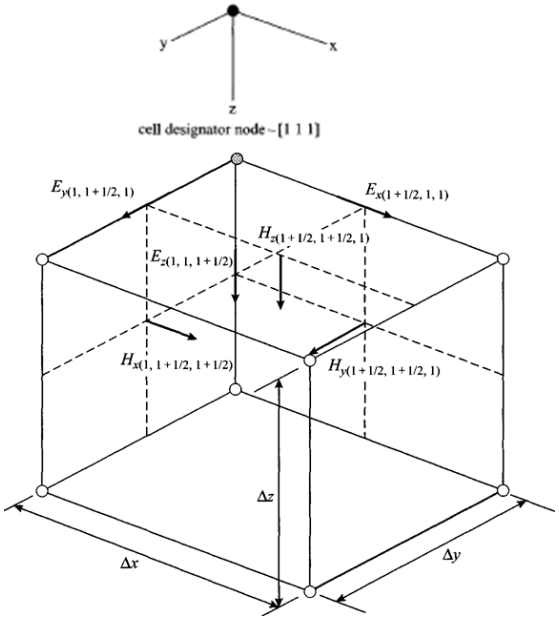


*Figure 3.1: Individual 'Yee cell' geometry with component Cartesian electric (E) and magnetic (M) field vectors staggered in space (Daniels, 2004)*

In the Yee cell, in order to apply the central finite difference approximation to the spatial derivatives of the governing equations, the points where the electric and magnetic field components are evaluated are placed half a spatial step apart. In these locations of the field components appropriate values of the constitutive parameters (permittivity, conductivity, and permeability) of the media present in the problem under study are assigned. A consequence of the construction of the Yee cell in a Cartesian coordinate system is that objects, whose geometry does not conform to the Yee cell's coordinate system, are modeled using a staircase approximation to their real boundary, such as objects with curved boundaries. This approximation introduces errors into the calculation and artifacts in the simulation. In order to minimize these errors, the wavelength of the electromagnetic fields should be large compared with the dimensions of the individual Yee cells, and the object must be adequately represented by Yee cells.

The FDTD numerical solution is obtained directly in the time domain by using a discretized version of Maxwell's curl equations that are applied in each FDTD cell, through an iterative process in which the values of the field components at the Yee cells are updated using the FDTD equations. In each iteration the electromagnetic fields advance in the FDTD grid and each iteration corresponds to a time step $\Delta t$. Hence by

specifying the number of iterations it is possible simulate the fields for a given time window.

The price one has to pay for obtaining a solution directly in the time domain using an explicit numerical method like FDTD is that the values of the temporal discretization step *Δt* cannot be assigned arbitrarily, but it is related to the spatial discretization *Δx*, *Δy* and *Δz*, by the Courant stability condition that should be satisfied for the FDTD solution to be stable.

The stability condition known as the CFL condition (after the initials of Courant, Freidrichs and Lewy) is:

$$\Delta t \leq \frac{1}{c\sqrt{\frac{1}{\Delta x^2}+\frac{1}{\Delta y^2}+\frac{1}{\Delta z^2}}}$$

where *c* is the speed of light.

The stability condition for the 2D case is obtained by letting $\Delta z \to \infty$.

In the FDTD algorithm the values of the electric and magnetic field components are obtained for each new time step from the values of the nearest neighbors' field components (according to Maxwell's equations) at the previous time step.

Therefore, matrix inversion is not required, and FDTD is characterized as an explicit method in both space and time. The stability condition is a result of this explicit nature of the FDTD method and is a direct result of the requirement that information cannot propagate, from one cell to each of its neighbors, faster than the speed of light (Millard et al., 1998).

An important issue in modelling open boundary problems like GPR is the truncation of the FDTD grid of the computational domain at a finite distance from the sources and targets where the values of the electromagnetic fields cannot be calculated directly by the numerical method.

Therefore, approximate conditions known as absorbing boundary conditions (ABCs) are applied at a sufficient distance from the source to truncate and therefore limit the computational space, in order to simulate an open space. The role of these ABCs is to absorb any waves impinging on them, hence simulating an unbounded space.

The computational space limited by these ABCs should contain all important features of the problems geometry, such as all sources and output points and important targets.

In cases, where the host medium cannot be assumed to be of infinite extent (e.g., a finite concrete slab) the assumption can still be made as far as the slabs actual size is large enough that any reflected waves that will originate at its termination will not affect the solution for the required time window (Giannopoulos, 2005).

## 3.3 GprMax

GprMax is an open-source software that simulates electromagnetic wave propagation for numerical modelling of GPR. It solves Maxwell's equations in 3D using the Finite-Difference Time-Domain (FDTD) method. From the origin of its develop (Giannopoulos, 2005), gprMax has been successfully used for diverse range of applications in academia and industry, such as for the assessment of GPR in magnetically lossy materials (Cassidy & Millington, 2009), rebar location in concrete structures (Orlando, 2012), for the asphalt pavement compaction monitoring (Shangguan & Al-Qadi, 2015), for the structural evaluation of masonry bridges (Solla et al., 2012), for the soil moisture estimation (Tran et al., 2014), etc..

GprMax is cross-platform and was originally written using the C programming language. In order to facilitate the implementation of new advanced features the code was rewritten in an object-orientated language: Python.

Python is an interpreted language that is object-oriented and features dynamic typing and automatic memory management. It is also intended to be highly readable and extensible. However, the ease and flexibility of Python comes at a cost of speed when compared to statically typed languages such as C. This loss of speed has been mitigated with the new version of gprMax, that was written using a combination of Python, NumPy, and Cython with OpenMP, which keeps the benefits of Python with most of the speed of C (Warren et al., 2015).

GprMax consists of two simulators – GprMax2D, which solves the transverse-magnetic mode with respect to z (TMz) in 2D, and GprMax3D which solves the full FDTD algorithm in 3D. Both simulators are command-line-driven programs that do not feature a graphical user interface (GUI).

Some of their key features are: an easy to use command interface; user-definable materials; user-specifiable excitation functions; simulation of thin wires; an unsplit implementation of higher order perfectly matched layers (PMLs) using a recursive

integration approach; the ability to model dispersive media using multiple Debye, Drude or Lorenz expressions; improved soil modeling using a semi-empirical formulation for dielectric properties and fractals for geometric characteristics; rough surface generation; and the ability to embed complex transducers and targets (Warren et al., 2016).
Moreover, GprMax3D allows the simulation of GPR antennas and even the introduction of their feeding transmission lines into the model.
Both GprMax2D and 3D programs use a simple ASCII (text) input file to define the models parameters for the simulation, such as model size, discretization, time window, geometry, materials, and excitation pulse.

## 3.4 Preliminary models

As seen in Chapter 1, the field surveys highlighted different GPR responses according to the types of material and frequency antennas because the attenuation is directly correlated to the building material and resolution to antenna frequency and object dimension. In particular, the Nymphaeum wall displays low resolution resulting from a non-optimal antenna-wall coupling due to the roughness of the wall. Moreover, even by increasing the frequency, we do not always have an evident increase of the resolution in the superficial layer.
Starting from the consideration, in the following sections we aim to:

- evaluate an improve of GPR response in terms of horizontal and vertical resolution as a function of frequency of the antenna and the type of materials;
- improve the wall-antenna coupling particularly for rough surfaces;
- understand the detectability of critical elements (fractures, slackening, etc.) and of thicknesses and geometries of the masonry.

In light of this, the interposition, between the surface of the investigated medium and the GPR antenna of a dielectric material (e.g. Plexiglas) was theoretically studied through synthetic models.
Firstly a model composed by stone blocks containing a micro-pile was set up and then models simulating laboratory samples were calculated with the aim of evaluating the theoretical answer and the changes in the GPR response due to the interposition of a Plexiglas layer between the antenna and the sample.

### ✓ 3.4.1 Geometry and materials

The synthetic model shown in Fig. 3.2a depicts a wall built with four lines of rock blocks different in size, a near-surface concrete layer and a micro-pile built into a borehole 0.19 m in diameter, including a 6 mm thick iron casing having a diameter of 0.13 m. The borehole and casing are filled with concrete.

The minimum and maximum spacing between bricks, are 1 cm and 15.2 cm horizontally and 0.3 cm and 2 cm vertically, respectively.

The 2D modelling was performed using a Ricker wavelet with unit amplitude (1.0) and two different peak frequencies (800 and 1100 MHz), chosen as they cover the range usually adopted for high-resolution investigation of structures.

In fact, increasing the antenna frequency resolution is enhanced and consequently anomalies due to the heterogeneity of the construction material are visible in the GPR section. These anomalies affect the backscattered signal by obscuring and/or reducing the target detection and causing a loss of transmitted energy by means of an increase of scattering, as seen for example at the "Nymphaeum" wall. Both phenomena are extremely frequency-dependent and can become even more important than electrical loss (Annan, 2003). In general, the backscattered electromagnetic energy depends on the electromagnetic properties of the background medium and of the desired target, the ratio between the size of the target and the signal wavelength, the incident and the reflected angle of the signal, the strength of the radar transmitter and the distance between transmitter–target–receiver.

Polarization directions may either be in x or y orientations.

In the presented model the EM wave is polarized in the x-direction.

The recording time was set equal to 30 ns, in order to that the two-way travel time for radar waves propagating from one end of the surface to the bottom of the sample could be recorded.

According to the CFL condition a space discretization of 2.5 mm was set.

In order to simulate GPR profiles with a sampling compatible with a field survey, model runs must be repeated, moving transmitting and receiving antennas pair at 0.01 m increments.

The electromagnetic parameters relative to the materials used in the model are showed in Table 3.1 (Orlando, 2012; Akhter & Akhtar, 2016). The values for the air layer are those of free space.

| *Medium* | $\varepsilon_r$ | $\sigma$ *(S/m)* | $\mu_r$ |
|---|---|---|---|
| Concrete | 6.0 | 0.01 | 1.0 |
| Rock | 4.0 | 0.06 | 1.0 |
| Filling material | 8.25 | 0.02 | 1.0 |
| Iron (PEC) | - | $10^7$ | 1.02 |
| Plexiglas | 3.4 | - | 1.0 |

*Table 3.1: Relative permittivity ($\varepsilon_r$), conductivity ($\sigma$) and relative permeability ($\mu_r$) of materials used in the forward model of Fig. 3.2-3.3*

The main goal of the preliminary synthetic simulation is to assess the added value of the Plexiglas interposition, considering different thicknesses, namely: 2.5 mm, 5.0 mm and 10 mm.

Therefore, using GprMax v.2 we obtained radargrams for each frequency and for the different Plexiglas thicknesses.

### ✓ 3.4.2 Results

The results are shown in Figs. 3.2b-f for the 800 MHz and in Figs. 3.3b-f for the 1100 Hz frequencies, respectively, as a function of the Plexiglas thickness. For the sake of simplicity, only a comparison between two configurations (0 vs. 2.5 mm in Fig. 3.2 and 0 vs. 10 mm in Fig. 3.3) is reported.

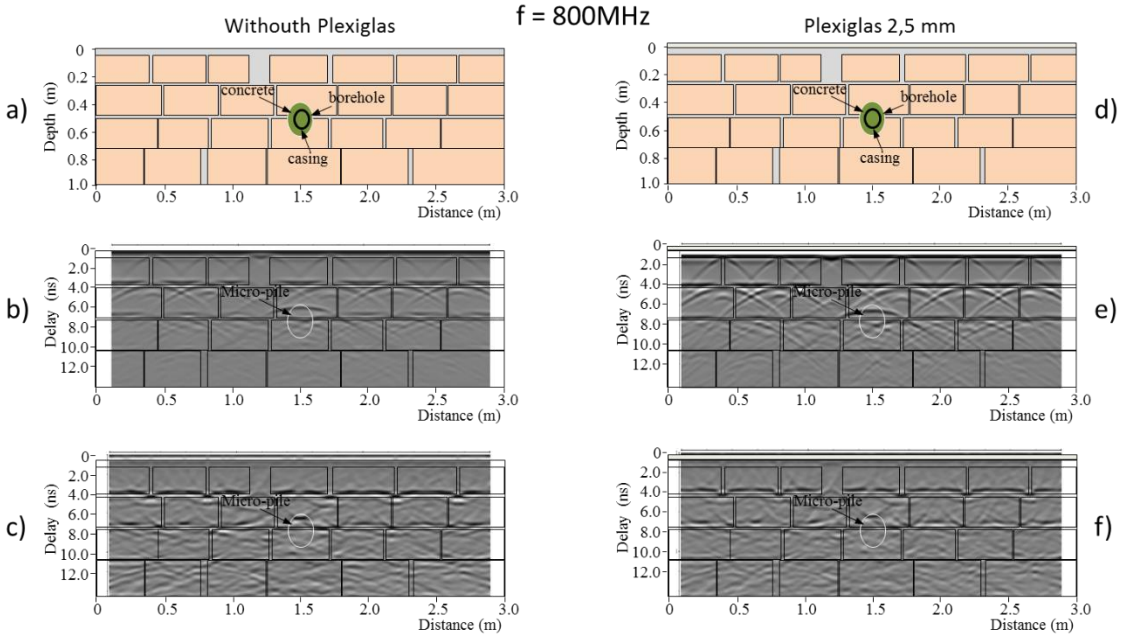


*Figure 3.2: Synthetic model of the preliminary sample at 800 MHz peak frequency, without Plexiglas a) and with 2.5 mm of Plexiglas d). GPR processed profile b), e); GPR migrated processed profile (Stolt algorithm) c), f) respectively without and with 2.5 mm of Plexiglas*

Although GprMax outputs results of the six components of the electromagnetic fields (Ex, Ey, Ez, Hx, Hy, and Hz) as well as the currents (Ix, Iy, and Iz) calculated as the curl of the magnetic fields at each electric field location, only the Ex values are mapped. These values are the same as those collected in the field with both standard shielded antennas oriented in the x-direction while recording along the y-direction.

The synthetic results provided by GprMax were exported to ReflexW and filtered using a very similar processing sequence to that used for the field data. In particular, this standard processing encompasses an application of a AGC-gain and a running average. The corresponding radargrams are given in Fig. 3.2b,e and 3.3b,e. Then, a Stolt migration was applied using a constant velocity of 12.5 cm/ns and results of this are shown in Figs. 3.2c,f. and 3.3c,f.

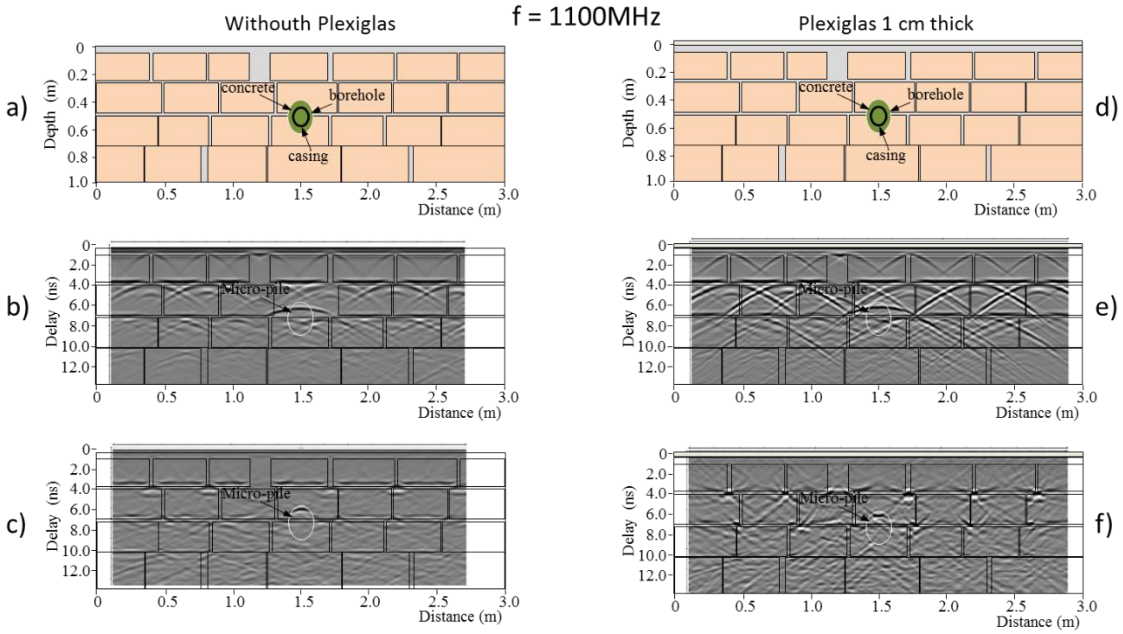


*Figure 3.3: Synthetic model of the preliminary sample at 1100 MHz peak frequency, without Plexiglas a) and with 1 cm of Plexiglas d). GPR processed profile b), e); GPR migrated processed profile (Stolt algorithm) c), f) respectively without and with 1 cm of Plexiglas*

The radargrams show a very similar response in the different configurations: for increasing depths the imaging of the bricks borders become more difficult and for the deepest brick layer the targets are difficult to be detected, due to the high set frequencies. For the same target, the hyperbolic shapes of the backscattered signals slightly differ in width, depending on signal frequency. The borehole produces a signature very similar to a diffraction hyperbola.

The migrated sections (Fig. 3.3e and f) give a negligible improvement with respect to the unmigrated ones (Fig. 3.3b and d) because also the diffracted energy of multiple diffraction hyperbola are focused, giving rise to several anomalies which are not related to any actual object.

A better imaging of the first part of the wall, often hidden from the direct wave presence, was obtained thanks to the presence of the Plexiglas layer; this is more evident for the greater thickness of the Plexiglas layer.

In light of this, the comparative analysis related to the benefit of the Plexiglas layer has been further developed on synthetic models related to masonry samples built up in the laboratory, for the a priori evaluation of the possible advantages of this system with reference to the monitoring of a static load test.

## 3.5 Synthetic modeling

Given the above mentioned open problems, models regarding structures that are typically encountered in real cases have been reproduced, trying to get information on the response of geophysical surveys to changes in the survey configuration. Therefore, undisturbed and fractured brick and tuff small-scale panels were built up, in order to evaluate the influence of the fractures on the GPR response, and its theoretical capability in the anomalies reconstruction. Furthermore, as estimated in the preliminary phase, the modeling was carried also assuming to interpose a Plexiglas with different thickness between the masonry surface and geophysical instrument.

The main goal of the synthetic simulation is to assess the added value of the Plexiglas interposition and to evaluate the capability of the GPR system to detect fractures on these construction materials.

Simulations were carried out through gprMax 3.0 (Giannopoulos, 2005).

### ✓ 3.5.1 Geometry and materials

The masonry panels are built of tuff blocks (33 x 11 x 24 cm) and bricks (22.5 x 5 x 10 cm). Overall, the tuff sample is 1 m long, 1 m high and 0.25 m wide (Fig. 3.4a), while the bricks sample is 0.95 x 0.95 x 0.25 m (Fig. 3.4b).

The spacing between the blocks of tuff are 1.7 cm horizontally and 1.8 cm vertically, while between the bricks are 1.5 and 2.0 cm horizontally and 1.5 cm vertically. Bricks are disposed in one or two rows, depending on their particular orientation (Fig. 3.4b).

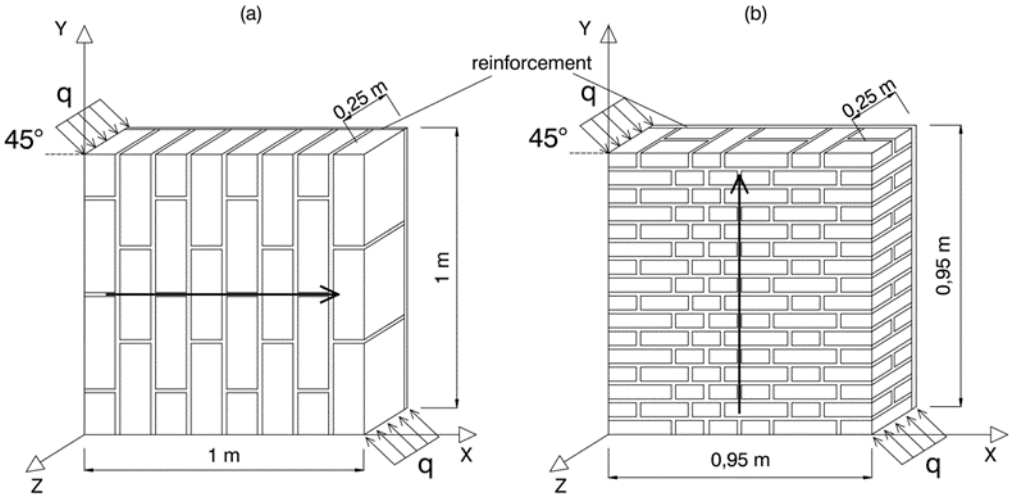


*Figure 3.4. Tuff (a) and bricks (b) laboratory panels*

For both construction types, the physical parameters for the concrete and for the Plexiglas, are the same of the preliminary models.

As a result of bibliographic research, the tuff with a relative permeability ($\mu_r$) equal to 1 and conductivity ($\sigma$) of 0.002 S/m was setting (Martinez & Byrnes, 2001). While, the relative permittivity ($\varepsilon_r$) and the conductivity ($\sigma$) of the bricks are 6.0 and 0.00125 S/m respectively (Peña et al., 2003). Furthermore, in order to confirm this values, the resistivity 1D Electrical measurements were performed on the single brick and tuff block. The resulting resistivity values are equal to 300 and 500 Ωm, respectively.

The complex fracturing patterns hypothesized after the load application was simulated by adding a series of rectangular and/or triangular thin zones (thickness = 4 mm) in which the free space condition ($\varepsilon_o = 8.854187\times10^{-12}$ F/m, $\mu_0 = 1.256637\times10^{-6}$ H/m) is imposed.

Antenna specifications chosen for the models are a reasonable approximation of a 2 GHz shielded antenna. In the GprMax program this is chosen by selecting model parameters of a Hertzian dipole loaded with unit amplitude (1.0) and a center frequency of a Ricker wavelet of 1100 MHz. This command technically simulates an infinitesimal dipole, which is an acceptable approximation of the shielded systems (Gooch, 2010). The Ricker peak frequency of 1100 MHz was taken into account on the basis of a spectral analysis of the actual data acquired on the laboratory samples before and after the stress application.

The transmitter–receiver offset is equal to 0.04 m, such as the real 2 GHz antennas.

According to the CFL condition, a space discretization of 4 mm was chosen, in order to strike a balance between the resolution need and the computational costs (about 36 hours using a CPU with a 2.70 GHz processor and 16 GB of ram). GPR longitudinal and transversal profiles spaced of 0.1 m were simulated, with model runs repeated, moving transmitting and receiving antennas pair, about 207 times for the bricks models and 226 times for the tuff models, at 4 mm increments, for each profile. The total recording time was set equal to 7 ns. The synthetic results provided by gprMax were exported to Matlab and processed as GPR sections and time slices.

An example of GprMax input file is reported below.

```
#domain: 0.95 0.5 0.95
#dx_dy_dz: 0.004 0.004 0.004
#time_window: 7e-9

#material: 4.5 0.01 1 0 concrete
#material: 6 0.00125 1 0 mattone
#material: 3.4 0 1 0 plexiglass
```

```
#waveform: ricker 1 1.1e9 my_ricker
#hertzian_dipole: z 0.1 0.435 0.040 my_ricker
#rx: 0.1 0.435 0.080
#hertzian_dipole: z 0.2 0.435 0.040 my_ricker
#rx: 0.2 0.435 0.080
#hertzian_dipole: z 0.3 0.435 0.040 my_ricker
#rx: 0.3 0.435 0.080
#hertzian_dipole: z 0.4 0.435 0.040 my_ricker
#rx: 0.4 0.435 0.080
#hertzian_dipole: z 0.5 0.435 0.040 my_ricker
#rx: 0.5 0.435 0.080
#hertzian_dipole: z 0.6 0.435 0.040 my_ricker
#rx: 0.6 0.435 0.080
#hertzian_dipole: z 0.7 0.435 0.040 my_ricker
#rx: 0.7 0.435 0.080
#hertzian_dipole: z 0.8 0.435 0.040 my_ricker
#rx: 0.8 0.435 0.080
#hertzian_dipole: z 0.9 0.435 0.040 my_ricker
#rx: 0.9 0.435 0.080
#src_steps: 0.0 0.0 0.004
#rx_steps: 0.0 0.0 0.004

#box: 0.0 0.0 0.0 0.94 0.20 0.94 free_space
#box: 0.0 0.20 0.0 0.94 0.425 0.94 concrete
#box: 0.0 0.20 0.0 0.225 0.3 0.05 mattone
#box: 0.24 0.20 0.0 0.34 0.425 0.05 mattone
#box: 0.36 0.20 0.0 0.46 0.425 0.05 mattone
#box: 0.475 0.20 0.0 0.575 0.425 0.05 mattone
#box: 0.59 0.20 0.0 0.815 0.3 0.05 mattone
#box: 0.83 0.20 0.0 0.94 0.425 0.05 mattone
#box: 0.0 0.20 0.065 0.1 0.425 0.115 mattone
#box: 0.115 0.20 0.065 0.285 0.3 0.115 mattone
#box: 0.3 0.20 0.065 0.4 0.425 0.115 mattone
#box: 0.415 0.20 0.065 0.64 0.3 0.115 mattone
#box: 0.655 0.20 0.065 0.755 0.425 0.115 mattone
#box: 0.77 0.20 0.065 0.94 0.3 0.115 mattone
#box: 0.0 0.20 0.13 0.225 0.3 0.18 mattone
#box: 0.24 0.20 0.13 0.34 0.425 0.18 mattone
#box: 0.36 0.20 0.13 0.46 0.425 0.18 mattone
#box: 0.475 0.20 0.13 0.575 0.425 0.18 mattone
#box: 0.59 0.20 0.13 0.815 0.3 0.18 mattone
#box: 0.83 0.20 0.13 0.94 0.425 0.18 mattone
#box: 0.0 0.20 0.195 0.1 0.425 0.245 mattone
#box: 0.115 0.20 0.195 0.285 0.3 0.245 mattone
#box: 0.3 0.20 0.195 0.4 0.425 0.245 mattone
#box: 0.415 0.20 0.195 0.64 0.3 0.245 mattone
#box: 0.655 0.20 0.195 0.755 0.425 0.245 mattone
#box: 0.77 0.20 0.195 0.94 0.3 0.245 mattone
#box: 0.0 0.20 0.26 0.225 0.3 0.31 mattone
#box: 0.24 0.20 0.26 0.34 0.425 0.31 mattone
#box: 0.36 0.20 0.26 0.46 0.425 0.31 mattone
#box: 0.475 0.20 0.26 0.575 0.425 0.31 mattone
#box: 0.59 0.20 0.26 0.815 0.3 0.31 mattone
#box: 0.83 0.20 0.26 0.94 0.425 0.31 mattone
#box: 0.0 0.20 0.325 0.1 0.425 0.375 mattone
#box: 0.115 0.20 0.325 0.285 0.3 0.375 mattone
#box: 0.3 0.20 0.325 0.4 0.425 0.375 mattone
#box: 0.415 0.20 0.325 0.64 0.3 0.375 mattone
#box: 0.655 0.20 0.325 0.755 0.425 0.375 mattone
#box: 0.77 0.20 0.325 0.94 0.3 0.375 mattone
#box: 0.0 0.20 0.39 0.225 0.3 0.44 mattone
#box: 0.24 0.20 0.39 0.34 0.425 0.44 mattone
#box: 0.36 0.20 0.39 0.46 0.425 0.44 mattone
#box: 0.475 0.20 0.39 0.575 0.425 0.44 mattone
```

#box: 0.59 0.20 0.39 0.815 0.3 0.44 mattone
#box: 0.83 0.20 0.39 0.94 0.425 0.44 mattone
#box: 0.0 0.20 0.455 0.1 0.425 0.505 mattone
#box: 0.115 0.20 0.455 0.285 0.3 0.505 mattone
#box: 0.3 0.20 0.455 0.4 0.425 0.505 mattone
#box: 0.415 0.20 0.455 0.64 0.3 0.505 mattone
#box: 0.655 0.20 0.455 0.755 0.425 0.505 mattone
#box: 0.77 0.20 0.455 0.94 0.3 0.505 mattone
#box: 0.0 0.20 0.52 0.225 0.3 0.57 mattone
#box: 0.24 0.20 0.52 0.34 0.425 0.57 mattone
#box: 0.36 0.20 0.52 0.46 0.425 0.57 mattone
#box: 0.475 0.20 0.52 0.575 0.425 0.57 mattone
#box: 0.59 0.20 0.52 0.815 0.3 0.57 mattone
#box: 0.83 0.20 0.52 0.94 0.425 0.57 mattone
#box: 0.0 0.20 0.585 0.1 0.425 0.635 mattone
#box: 0.115 0.20 0.585 0.285 0.3 0.635 mattone
#box: 0.3 0.20 0.585 0.4 0.425 0.635 mattone
#box: 0.415 0.20 0.585 0.64 0.3 0.635 mattone
#box: 0.655 0.20 0.585 0.755 0.425 0.635 mattone
#box: 0.77 0.20 0.585 0.94 0.3 0.635 mattone
#box: 0.0 0.20 0.65 0.225 0.3 0.7 mattone
#box: 0.24 0.20 0.65 0.34 0.425 0.7 mattone
#box: 0.36 0.20 0.65 0.46 0.425 0.7 mattone
#box: 0.475 0.20 0.65 0.575 0.425 0.7 mattone
#box: 0.59 0.20 0.65 0.815 0.3 0.7 mattone
#box: 0.83 0.20 0.65 0.94 0.425 0.7 mattone
#box: 0.0 0.20 0.715 0.1 0.425 0.765 mattone
#box: 0.115 0.20 0.715 0.285 0.3 0.765 mattone
#box: 0.3 0.20 0.715 0.4 0.425 0.765 mattone
#box: 0.415 0.20 0.715 0.64 0.3 0.765 mattone
#box: 0.655 0.20 0.715 0.755 0.425 0.765 mattone
#box: 0.77 0.20 0.715 0.94 0.3 0.765 mattone
#box: 0.0 0.20 0.78 0.225 0.3 0.83 mattone
#box: 0.24 0.20 0.78 0.34 0.425 0.83 mattone
#box: 0.36 0.20 0.78 0.46 0.425 0.83 mattone
#box: 0.475 0.20 0.78 0.575 0.425 0.83 mattone
#box: 0.59 0.20 0.78 0.815 0.3 0.83 mattone
#box: 0.83 0.20 0.78 0.94 0.425 0.83 mattone
#box: 0.0 0.20 0.845 0.1 0.425 0.895 mattone
#box: 0.115 0.20 0.845 0.285 0.3 0.895 mattone
#box: 0.3 0.20 0.845 0.4 0.425 0.895 mattone
#box: 0.415 0.20 0.845 0.64 0.3 0.895 mattone
#box: 0.655 0.20 0.845 0.755 0.425 0.895 mattone
#box: 0.77 0.20 0.845 0.94 0.3 0.895 mattone
#box: 0.0 0.20 0.91 0.225 0.3 0.94 mattone
#box: 0.24 0.20 0.91 0.34 0.425 0.94 mattone
#box: 0.36 0.20 0.91 0.46 0.425 0.94 mattone
#box: 0.475 0.20 0.91 0.575 0.425 0.94 mattone
#box: 0.59 0.20 0.91 0.815 0.3 0.94 mattone
#box: 0.83 0.20 0.91 0.94 0.425 0.94 mattone
#box: 0.0 0.325 0.0 0.225 0.425 0.05 mattone
#box: 0.59 0.325 0.0 0.815 0.425 0.05 mattone
#box: 0.115 0.325 0.065 0.285 0.425 0.115 mattone
#box: 0.415 0.325 0.065 0.64 0.425 0.115 mattone
#box: 0.77 0.325 0.065 0.94 0.425 0.115 mattone
#box: 0.0 0.325 0.13 0.225 0.425 0.18 mattone
#box: 0.59 0.325 0.13 0.815 0.425 0.18 mattone
#box: 0.115 0.325 0.195 0.285 0.425 0.245 mattone
#box: 0.415 0.325 0.195 0.64 0.425 0.245 mattone
#box: 0.77 0.325 0.195 0.94 0.425 0.245 mattone
#box: 0.0 0.325 0.26 0.225 0.425 0.31 mattone
#box: 0.59 0.325 0.26 0.815 0.425 0.31 mattone
#box: 0.115 0.325 0.325 0.285 0.425 0.375 mattone
#box: 0.415 0.325 0.325 0.64 0.425 0.375 mattone

```
#box: 0.77 0.325 0.325 0.94 0.425 0.375 mattone
#box: 0.0 0.325 0.39 0.225 0.425 0.44 mattone
#box: 0.59 0.325 0.39 0.815 0.425 0.44 mattone
#box: 0.115 0.325 0.455 0.285 0.425 0.505 mattone
#box: 0.415 0.325 0.455 0.64 0.425 0.505 mattone
#box: 0.77 0.325 0.455 0.94 0.425 0.505 mattone
#box: 0.0 0.325 0.52 0.225 0.425 0.57 mattone
#box: 0.59 0.325 0.52 0.815 0.425 0.57 mattone
#box: 0.115 0.325 0.585 0.285 0.425 0.635 mattone
#box: 0.415 0.325 0.585 0.64 0.425 0.635 mattone
#box: 0.77 0.325 0.585 0.94 0.425 0.635 mattone
#box: 0.0 0.325 0.65 0.225 0.425 0.7 mattone
#box: 0.59 0.325 0.65 0.815 0.425 0.7 mattone
#box: 0.115 0.325 0.715 0.285 0.425 0.765 mattone
#box: 0.415 0.325 0.715 0.64 0.425 0.765 mattone
#box: 0.77 0.325 0.715 0.94 0.425 0.765 mattone
#box: 0.0 0.325 0.78 0.225 0.425 0.83 mattone
#box: 0.59 0.325 0.78 0.815 0.425 0.83 mattone
#box: 0.115 0.325 0.845 0.285 0.425 0.895 mattone
#box: 0.415 0.325 0.845 0.64 0.425 0.895 mattone
#box: 0.77 0.325 0.845 0.94 0.425 0.895 mattone
#box: 0.0 0.325 0.91 0.225 0.425 0.94 mattone
#box: 0.59 0.325 0.91 0.815 0.425 0.94 mattone
#triangle: 0.0 0.275 0.764 0.474 0.275 0.254 0.472 0.275 0.304 0.15 free_space
#box: 0.474 0.275 0.240 0.640 0.425 0.254 free_space
#box: 0.640 0.275 0.191 0.654 0.425 0.240 free_space
#box: 0.654 0.275 0.187 0.94 0.425 0.191 free_space
#box: 0.0 0.425 0.0 0.94 0.435 0.94 plexiglass
#geometry_view: 0 0 0 0.95 0.50 0.95 0.004 0.004 0.004 example model n
```

### ✓ 3.5.2 Results

Results of simulations are shown in Figs. 3.5 and 3.6 in terms of GPR sections for both panels before and after the load application, while in Figs. 3.7 and 3.8 the respective time-slices drawn at a depth of 5 cm considering a window of 0-10 cm for the same configurations are shown.

The tuff radargrams (Fig. 3.5) show that the added value of the Plexiglas interposition is negligible for simulations performed. However, we have a loss of resolution using Plexiglas, that reduce the capability to detect the mortar joints between the blocks (black arrows), while the back face of the panel (dashed line) and the fracture are always discriminated (white arrow).

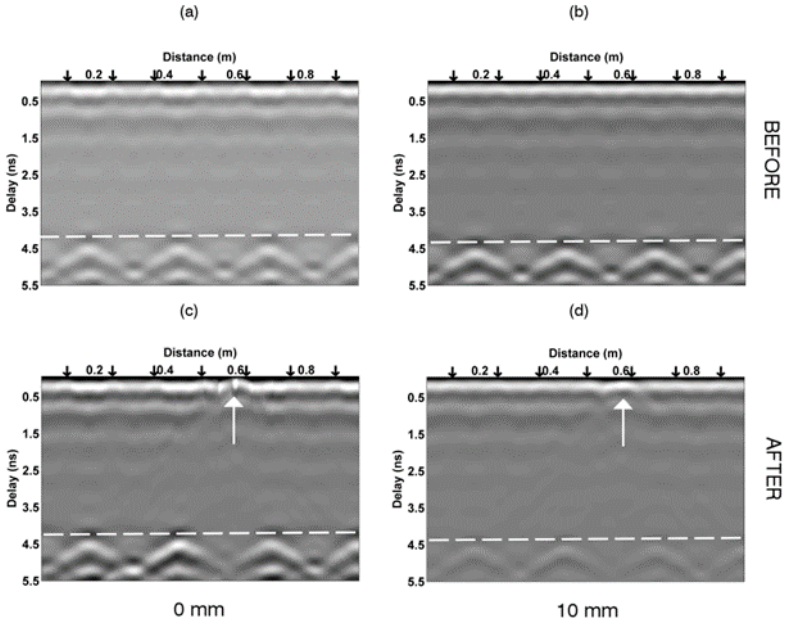


*Figure 3.5: Synthetic model of the tuff sample. GPR x-directed profile at y=0.5 m of the undisturbed sample, without (a) and with 10 mm of Plexiglas (b). GPR x-directed profile at y=0.5 m of the fractured sample, without (c) and with 10 mm of Plexiglas (d). The white dashed line indicates the reinforced face of the wall, the white arrow the presence of the fracture.*

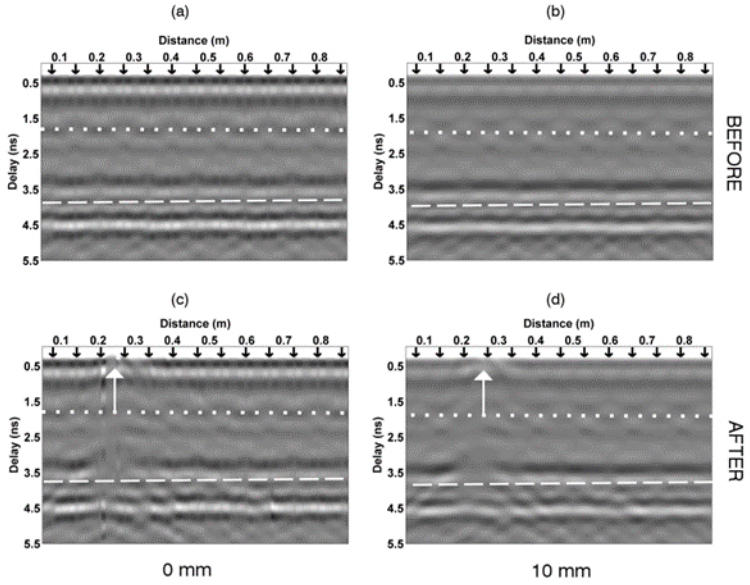


*Figure 3.6: Synthetic model of the laboratory bricks sample. GPR y-directed profile at x=0.5 m of the undisturbed sample, without (a) and with 10 mm of Plexiglas (b). GPR y-directed profile at x=0.5 m of the fractured sample, without (c) and with 10 mm of Plexiglas (d). The white dashed line indicates the reinforced face of the wall, the dotted line the end of the first row of bricks and the white arrow the presence of the fracture.*

Similar results were obtained for the bricks panel (Fig. 5), where joints (blacks arrows) are almost undistinguishable using Plexiglas, while the discontinuity between the two rows of bricks (dotted line) and the fracture are clearly visible in all GPR sections.

However, a better imaging of the superficial part of the wall was obtained thanks to the presence of the Plexiglas layer, as shown in particular in the synthetic model relative to the fractured models (Figs. 3.5-3.6c-d).

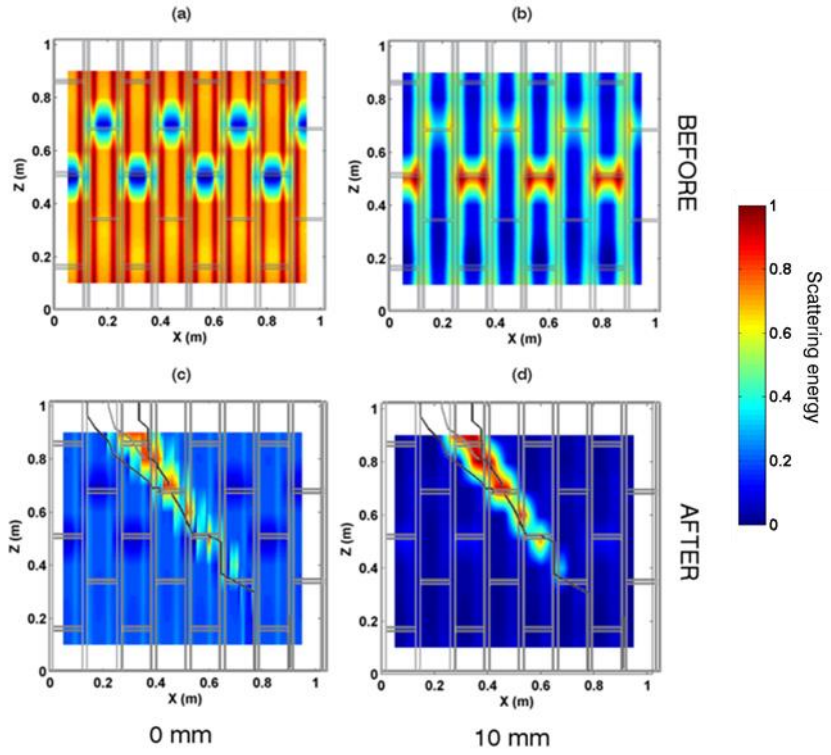


*Figure 3.7: Synthetic model of the laboratory tuff sample. GPR time-slice of the undisturbed sample, without (a) and with 10 mm of Plexiglas (b). GPR time-slice of the fractured sample, without (c) and with 10 mm of Plexiglas (s). Time-slices are drawn at a depth of 5 cm considering a thickness of 10 cm*

The respective time-slices confirm the evidences early revealed by GPR profiles. In fact we have for the tuff sample a higher resolution without using Plexiglas (Figs. 3.7a,c); otherwise (Figs. 3.7b,d) the joints remains visible anyway, even though with less amplitude compared to that of the fracture (Fig. 3.7d). In fact, the fractured sample image with Plexiglas (Fig. 3.7d) highlights more clearly the simulated fracture. Whereas, the amplitude of the GPR signal seen on the undisturbed configuration (Fig. a,b) strongly depends on the position of the profile: in fact signal is stronger where joints are exactly superimposed with GPR profile (e.g. y = 0.5 m and 0.7 m). as far as Fig. 3.7d),

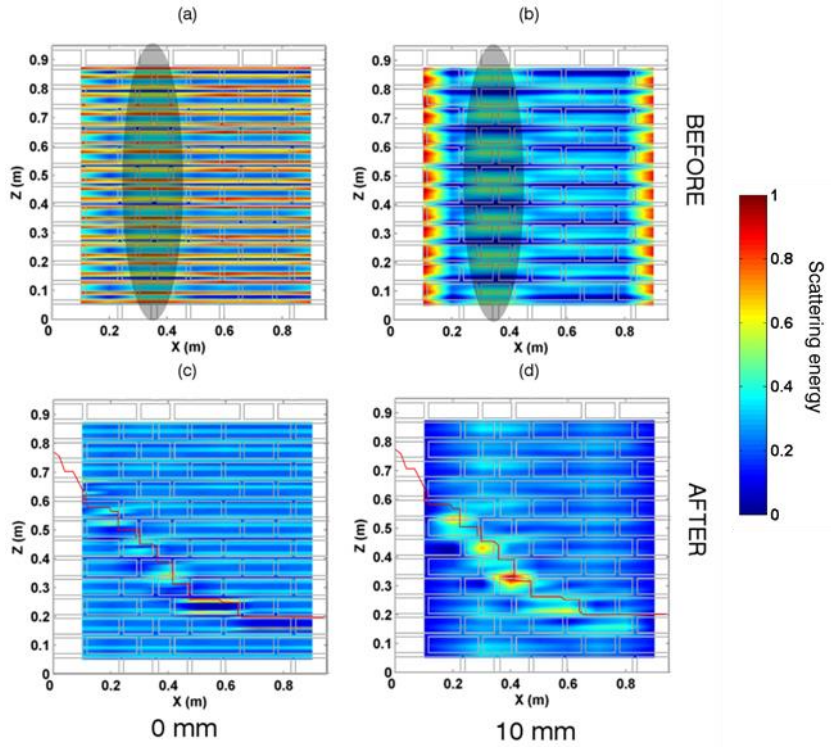


*Figure 3.8. Synthetic model of the laboratory bricks sample. GPR time-slice of the undisturbed sample, without (a) and with 10 mm of Plexiglas (b). GPR time-slice of the fractured sample, without (c) and with 10 mm of Plexiglas (d). The grey ellipses indicate the location of the single row of bricks. Time-slices are drawn at a depth of 5 cm considering a thickness of 10 cm*

In the bricks panel (Fig. 3.8), more heterogeneous then the tuff, this effect is enhanced, because of the large number of discontinuities between the bricks. In particular, we can see a different response according to the geometry of the sample: in the zone where the bricks are elongated in the z-direction (only one row of bricks, grey ellipse) and juxtaposed both in the x- and in the y- directions the response proves to be less scattered (Fig. 3.8 b).

The time slices are always able to discriminate the main fracture; and, where a Plexiglas layer is present, the response is more scattered in correspondence of the fracture and the cracks pattern is more clearly detected.

## 3.5 Summary

The synthetic models show a good resolution, since the modelling does not take into account the antenna-sample coupling and real smooth surface, as well as noise. In fact, in presence of rough surfaces, the coupling between antenna and artefact takes over, with

possible dragging problems of the antenna, that therefore may influence the GPR response.

As seen in the preliminary model, thanks to the presence of the Plexiglas, a better discretization of the superficial part of the wall was obtained, since this part is often hidden from the direct wave presence. The same advantage in the GPR radargrams relative to the bricks and tuff panels was observed, where a Plexiglas layer is present.

Therefore, given these synthetic simulations in the next Chapter 4 we evaluate the improvement generated by the application of the Plexiglas layer in the GPR investigation of two laboratory samples, presented above.

# 4. LABORATORY TESTS ON MANSORY SAMPLES

## 4.1 Introduction

The laboratory experiments were build up during a three years' campaign on masonry samples.

We can divide the laboratory activity into four phases:

- preliminary tests;
- design of devices and holders;
- data acquisition and processing;
- data interpretation.

The laboratory testing conducted on physical models that reproduce different types of construction, have the aims to evaluate the variation in the electromagnetic response due to the change of the structural elements, the determination of thicknesses and geometries materials and the evaluation of the state of degradation of the structures.

In order to unequivocally interpret the detected anomalies of the sample and to provide a range of variation of the parameters to be used in numerical modelling, GPR and geoelectrical methods were jointly applied.

Testing on laboratory models has the following objectives:

- to determine the advantages and drawbacks of each method to the object of study applications;
- to assess the change in the electromagnetic and electrical response of the constituent structural elements in the sample, in terms of attenuation and different degree of resolution;
- to identify and map critical elements of the structures (fractures, slackening, etc.);
- to evaluate the type of construction materials of the masonry structure;
- to determine thicknesses and geometries of the masonry.

The investigations were performed on samples before and after the application of a diagonal compressive load, in order to assess the geophysical response with reference to the most commonly encountered stresses in historical and modern structures.

The geophysical processed data are used for a joint interpretation of the panels for the detection of cracks and weakness zones.

## 4.2 Preliminary tests

The first phase, preliminary, involved samples that had already been subjected to stress in order to understand the applicability of the survey methodology to the samples under consideration and evaluate possible improvements previously evaluated through the modeling phase, in order to assess the geophysical response in identifying the most fractured areas. Therefore, the possible benefits of the Plexiglas interposition between surface and antenna is explored thoroughly with laboratory data given by the analysis of the GPR profiles acquired on the both faces of the panel.

*Figure 4.1: Image of the preliminary tests*

### ✓ *4.2.1* Samples geometry

The laboratory models object of experimentation was designed by the Structural Engineering laboratory of the "Sapienza" University of Rome. In particular, the tests focused on two masonry panels, made of bricks and tuff and having dimension of 0.95x0.95x0.24 m and 1.026x1.026x0.26 m, respectively.

The investigated panels were built up with the same configuration of Fig. 3.4, as follow:

- **Brick sample (**Fig. 4.2**).** This sample is made by bricks and mortar, where each brick has a size of 0.225 x 0.10 x 0.05 m. Bricks are disposed into one or two rows, as seen in Chapter 3. The sample is reinforced with a high-strength mixed material, made of high-conductive steel wires and high-resistive basalt fibre. Overall the reinforcement can be considered as a high-conductive material, in light of the laboratory measurement, made on small samples.

After the sample has been submitted to a diagonal load applied in correspondence of the top left and bottom right corners, we can see in Fig. 4.2 the consequent main fracture.

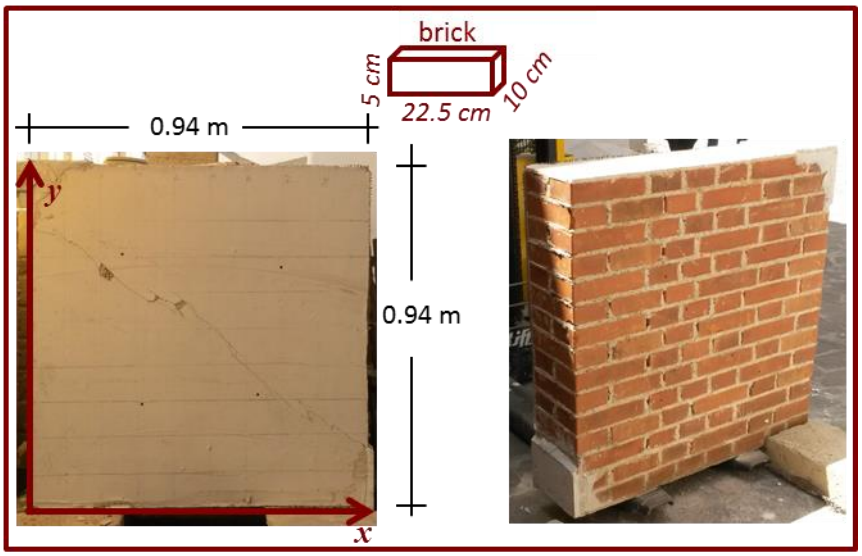


*Figure 4.2: Bricks sample. Reinforced (left) and unreinforced (right) faces.*

- **Tuff sample** (Fig. 4.3). This sample is made by block of tuff and concrete, where each block of tuff has a size of 0.33 x 0.24 x 0.11 m, and the same reinforcement seen above for the bricks is applied. In Fig. 4.3 the image of the panel surface after the application of the diagonal load is shown, where the most visibly fractured is along the direction of the straight (in the diagonal direction) and the joints between the blocks.

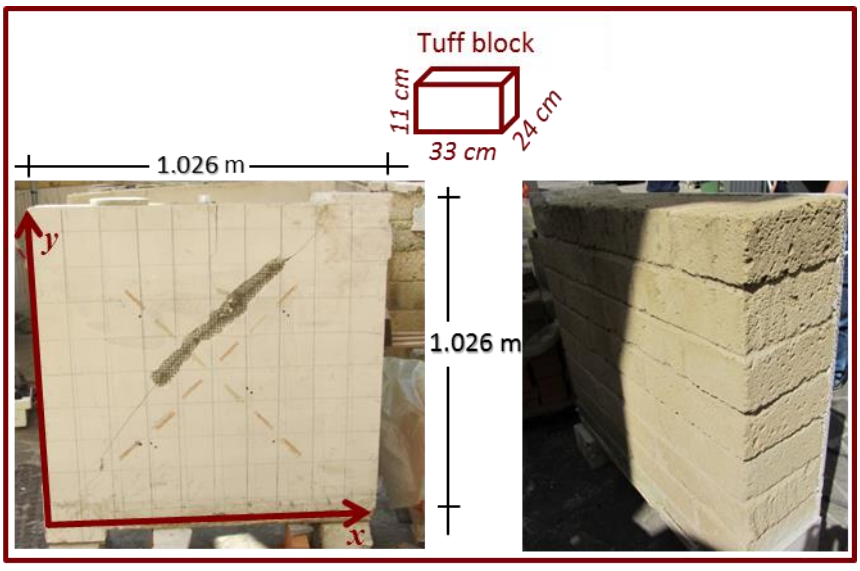


*Figure 4.3: Tuff sample. Reinforced (left) and unreinforced (right) faces.*

The reinforcement fabric (Fig. 4.4) was placed on one of the two faces for both panels in order to provide structural strengthening of masonry.

The choice of such reinforcement fits into a larger project of the Department of Structural and Geotechnical Engineering of the "Sapienza" University of Rome aimed to improve the knowledge on basalt textile-reinforced mortar BTRM reinforced walls to in-plane loads and to evaluate the effectiveness of such reinforced systems for tuff masonry system (Marcari et al, 2016). The BTRM reinforcement consisted of a balanced directional uncoated fabric made of basalt fibres and stainless steel micro-wires at a nominal spacing 10 mm x 10 mm (clear spacing between rovings of 7 mm) (Fig. 4.4).

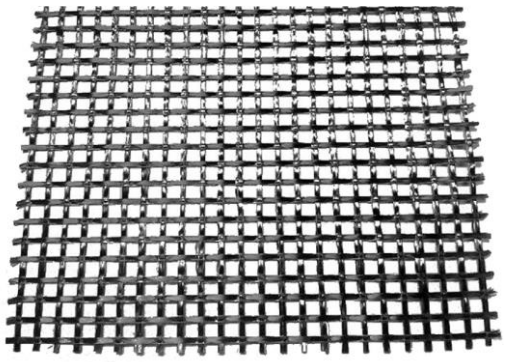

*Figure 4.4: Mixed basalt-steel reinforcement used in the current study (Marcari et al., 2016)*

In particular, apply basalt fiber reinforcing webs on cementitious, tuff or stone panels are unexpectedly easily manufactured and mainly panels obtain one or more of the following properties unexpectedly improved: tensile strength; cohesive strength; impact strength; temperature resistance; rigidity; strength uniformity; structural stability; flexural strength; resistance to water penetration and moisture degradation; uniformity of dimensions; reduced cockle; alkali resistance; surface density; surface smoothness; lower cost; nail-ability without cracking, breaking or other failure (Ritchie & Burkard, 2002). The test setup configuration and instrumentation of the diagonal compression tests are shown in Fig. 4.5. A universal MTS testing machine with a maximum load capacity of 500 kN in compression was used to test the specimens.

The servo-controlled actuator could supply ±100 mm of maximum displacement. Two steel shoes, placed on diagonally opposite corners of the specimen, transferred the force to the specimen. The space between the panel corners and the steel loading shoes was filled with high strength mortar. The load was applied using a hinge placed on the upper corner of the panel and was measured with a load cell with nominal capacity of 250 kN

in compression. All panels were tested under displacement control at 0.15 mm/min rate in order to capture post-peak softening.

Diagonal displacements were measured using 4 U strain gauges, two on each side, with a gauge length of 500 mm (Fig. 4.5).

The ASTM E 519-07 assumes that a uniform shear stress flow takes place along the loaded diagonal of the wall when subjected to diagonal compression. According to ASTM-E519, the shear stress is obtained as $\tau = 0.707\ P/An$, where P is the applied load and $A_n$ the net cross-sectional area of the panel ($A_n = 0{,}25\ m^2$) (Marcari et al., 2017).

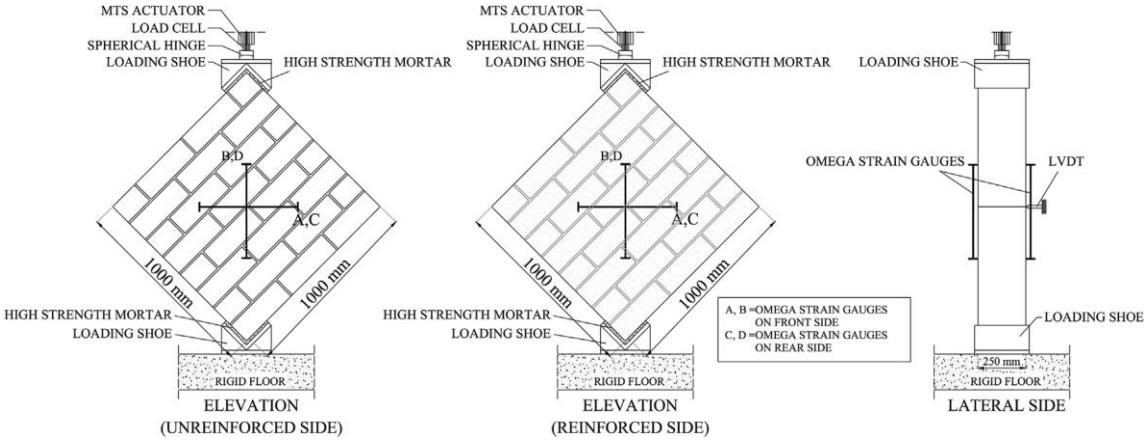


*Figure 4.5: Diagonal compression load test set up*

- ✓ 4.2.2 Data acquisition and processing
- ✓ 4.2.2.1 GPR

In the preliminary phase the GPR surveys were performed with the IDS 900 MHz and 2 GHz antenna (Fig. 4.6), in order to evaluate the frequency more suitable for the structure under examination.

*Figure 4.6: Images of the 2000 (a) and 900 (b) MHz antennas on the tuff sample.*

We consider only the results of the profiles acquired with the 2 GHz frequency antenna, since in this case most appropriate, given its higher resolution in the surface layers and the limited thickness of the samples tested, as possible see in Fig. 4.7.

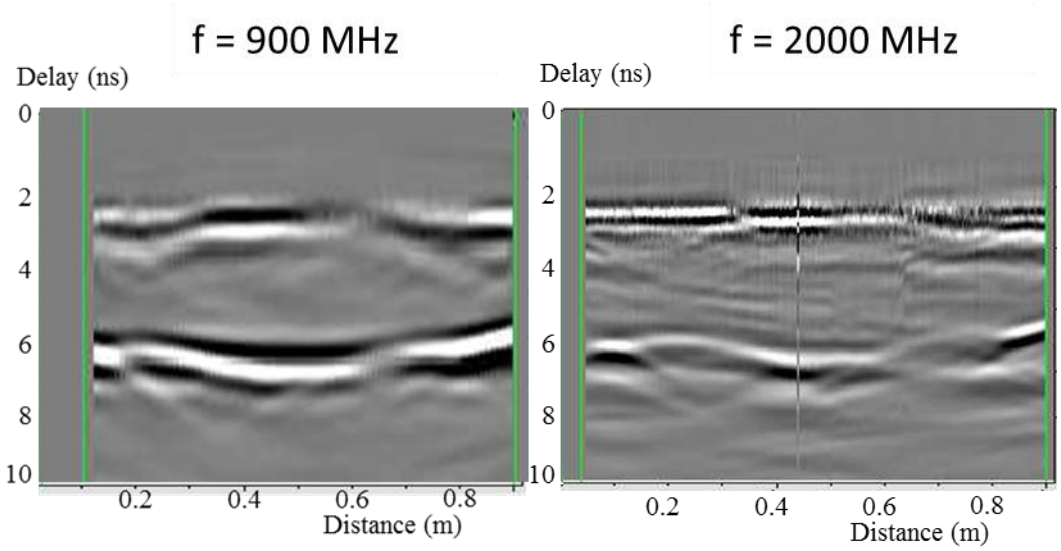


*Figure 4.7: Laboratory tuff sample. Example GPR x-directed profile at y=0.5 m acquired on the reinforced face with 10.0 mm of Plexiglas, with 900 and 2000 MHz frequency antennas*

Considering the geometry of the samples and the size of the GPR antenna, data were acquired on a regular grid, with x- and y-directed profiles spaced 10 cm apart (9 profiles for each direction). Each profile was acquired with a trace increment of 3.3 mm, within a time window of 15 ns and a sampling rate of 0.03 ns.

After the evaluation of the preliminary modeling phase, we have thus arrange 4 series of acquisitions: the first by placing the antenna directly in contact with the sample and then by interposing a dielectric material layer (Plexiglas) having different thicknesses: 2.5 mm, 5.0 mm and 10 mm.

The survey was carried out on both faces of the panels, in order to evaluate the influence of the reinforcement on the GPR data.

Acquired data were processed by means of a standard procedure (GPR profiles and time-slices) and of an advanced analysis, encompassing the picking of the EM wave arrival time and the analysis of the signal attenuation.

A standard processing of GPR data has been carried out with the software Gred, using the following functions:

- *Zero time correction:* this processing step facilitates a static correction in time direction by a given value.

- *Bandpassbutterworth* works within the frequency domain and acts on each trace independently. The filter band is specified by the setting of two frequency values. The filter band is specified by the setting of two frequency values, in this case: 200-1900 MHz. A mild filter was chosen in order to avoid the Gibbs phenomena. The first point determines the low-cut frequency, the second one the high cut frequency. The frequency spectrum below the low cut and above the high cut frequency is set to zero. By the corresponding choice of the points of the bandpass either a lowpass or a highpass can be approximately realized. Noise can be suppressed with the bandpass filter when it differs from the signal in its frequency content.

- *Background removal* to eliminate temporally coherent noise from the whole profile and to emphasize signals which vary laterally.

- *Migration* to focus the diffraction energies, obtained using the Stolt algorithm with a constant velocity of 12 cm/ns for the bricks sample and 11 cm/ns for the tuff sample

In the following sections, processed data are shown by means of profiles and time-slices. Time-slices are two-dimensional maps, made at different depths from the 3D data cube (x, y, t), by summing the scattering energy within a fixed thickness window: 5 or 10 cm. For the time to depth conversion we used a constant velocity of 12 cm/ns for the bricks sample and 11 cm/ns for the tuff sample, obtained as the mean value of the diffraction hyperbola produced by the edge of the blocks and from the picking of the EM wave arrival time.

✓ 4.2.2.2 ERT

The geoelectrical investigations were performed using 81 steel nails (diameter = 5 mm, 9 rows of 9 electrodes each) as electrodes, connected to a Syscal Iris Pro resistivimeter (Fig. 4.8). The input voltage was set to 12 V with a resulting current around 10 mA. Data were acquired using a dipole-dipole configuration on a 3D snake array, with two shifts of a set of 45 electrodes (5 rows of 9 electrodes each), where one row is therefore overlapped. In this preliminary phase the 3D data were processed through the ErtLab software (Multiphase Technology and Geostudi Astier) in order to reconstruct a 3D resistivity model. Instead, in the following load test monitoring, the 3D ERT data were processed with the VEMI algorithm (De Donno and Cardarelli, 2016).

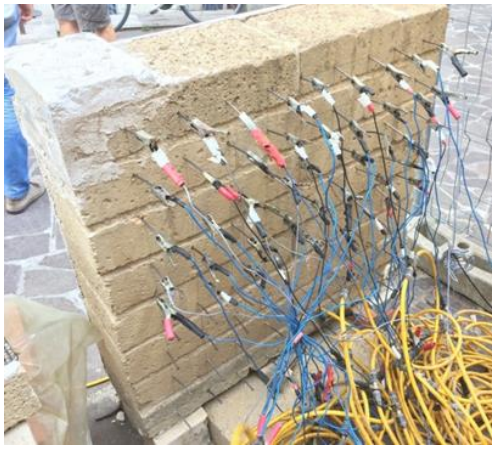

*Figure 4.8: ERT acquisition on tuff sample.*

✓ *4.2.3 Results*

Results, are analysed for the bricks and tuff sample, as a function of the four different configurations, linked to the thickness of the Plexiglas layer: 0, 2.5 mm, 5.0 mm and 10 mm. The aim of this comparative analysis is to evaluate the benefit of this add-on for detecting the structural elements and the fractures, with particular reference to the reinforced face, where a high-conductive layer may affect substantially the quality of the reconstruction.

✓ 4.2.3.1 GPR profiles

Data were acquired on a regular grid, with 9 profiles for each direction spaced 0.1 m each; only the middle x- and y-directed profiles were presented in the following, as they are the

most significant, given the position of the main fracture consequent to the load application. All the following presented profile are not migrated.

- Bricks sample

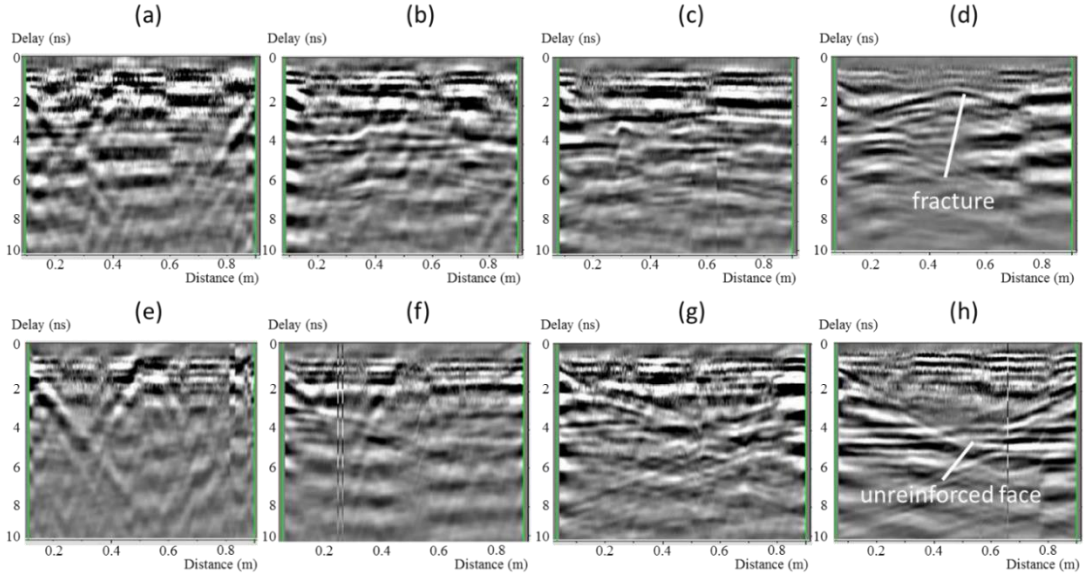


*Figure 4.9: Laboratory bricks sample. Example GPR x-directed profile at y=0.5 m acquired on the reinforced face without (a) and with 2.5 (b), 5.0 (c) and 10.0 mm of Plexiglas (d). GPR y-directed profile at x=0.5 m acquired on the reinforced face without (e) and with 2.5(f), 5.0 (g) and 10.0 mm of Plexiglas (h)*

The GPR radargrams acquired on the reinforced face show a high attenuated response due to the presence of the high-conductive material that causes a strong limitation for the signal penetration. However, by increasing the thickness of the dielectric material (Plexiglas) interposed between the sample and the GPR instrument, an improvement of the response has been achieved.

In particular, as shown in Figure 4.9d, in the longitudinal profile we are able to discriminate the diffraction hyperbolae due to the presence of the main fracture in the sample, while in the transversal profile (Fig. 4.9h) the interface between the sample and air, which were not visible in the previous configurations.

According to Liu et al., (1998), as a result of linear frequency dependence of attenuation, the spectrum centroid of a radar pulse experiences a downshift during propagation. The centroid downshift is proportional to the integral of an intrinsic attenuation coefficient with respect to length along the ray path. They studied the CFDS method, that is

applicable to subsurface radar data in the MHz to GHz frequency range when the signal bandwidth is broad enough and the attenuation is high enough to cause noticeable losses of high frequencies during propagation.

By assuming that the process of wave propagation can be described by linear system theory, if the amplitude spectrum of an incident wave is $S(f)$, and the medium and instrument response is $G(f) \cdot H(f)$, then the received amplitude spectrum $R(f)$ may be, in general, expressed as:

$$R(f) = G(f) \cdot H(f) \cdot S(f)$$

where the factor $G(f)$ includes geometric spreading, instrument response, source and receiver coupling to the medium, antenna radiation pattern, reflection and transmission coefficients, and the phase accumulation due to propagation, and $H(f)$ describes the attenuation effect on the amplitude. Frequency-dependent attenuation causes a change in the amplitude distribution of a wave's frequency spectra. For a linear model and a Gaussian spectrum, this change is simple: the difference in centroid frequency between the incident input and transmitted output waves is proportional to the integrated attenuation multiplied by a scaling factor (Liu et al., 1998).

Furthermore from the study of the coupling effects of two electric dipoles on an interface, (Slob, 2002) determined, for the H-plane receiver, a drop of the peak amplitude by more than a factor of 2 when the antenna is on the surface of a $\varepsilon_r$ = 5 half-space compared to an antenna in air. Again by a factor of 4 when changing from $\varepsilon_r$ = 5 to $\varepsilon_r$ = 10. This is all due to interference differences. For $\varepsilon_r$ = 10 the antenna separation is more than a dominant wavelength and increasing the permittivity further results in amplitude decrease that can be understood from the separate arrivals of the direct air and ground waves (Slob, 2002) .

Therefore, the interposition of a dielectric material reduces the drop of the peak amplitude and focuses the signal downwards, limiting the lateral reflections in air.

- Tuff sample

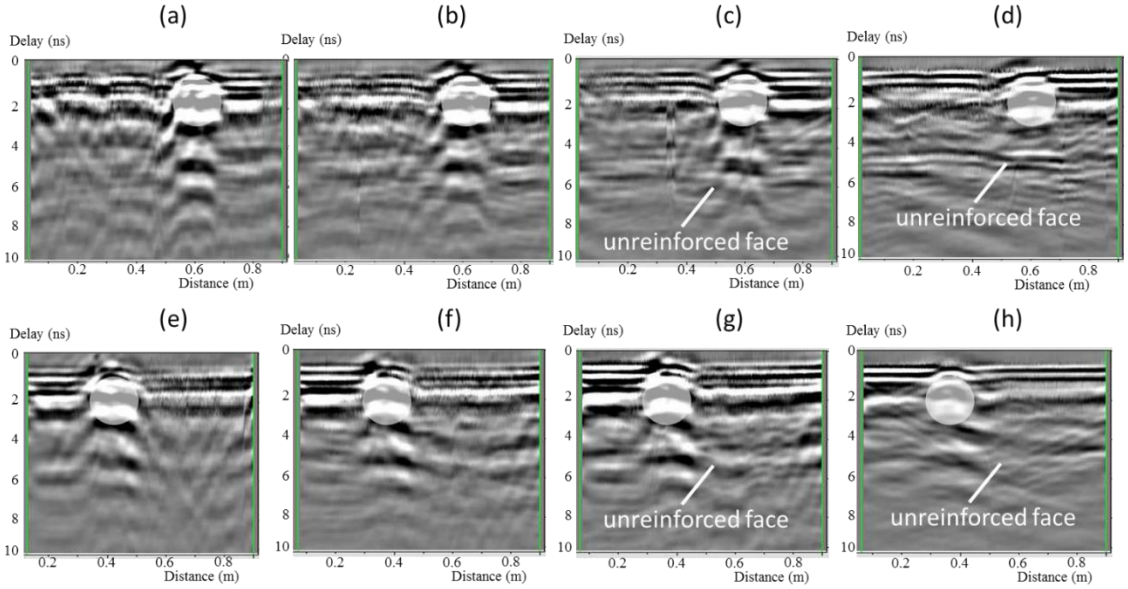


*Figure 4.10: Laboratory tuff sample. Example GPR x-directed profile at y=0.5 m acquired on the reinforced face without (a) and with 2.5 (b), 5.0 (c) and 10.0 mm of Plexiglas (d). GPR y-directed profile at x=0.5 m acquired on the reinforced face without (e) and with 2.5(f), 5.0 (g) and 10.0 mm of Plexiglas (h). The white circles indicate the zone where the antenna is directly couplet with the reinforcement*

Even in the case of tuff sample (Fig. 4.10), the GPR radargrams show a significant attenuation of the signal, where it is only possible to identify the main fracture. As in the case of bricks, with the 10 mm configuration (Fig. 4.10d-h) we obtain a significant improvement in the GRP response, and the rear sample-air interface is reached.

For the sake of completeness, the comparisons between the middle longitudinal (Fig. 4.11) and transversal (Fig. 4.11) sections acquired without and with 10 mm of Plexiglas are reported below, in order to assess the effective improvement achieved.

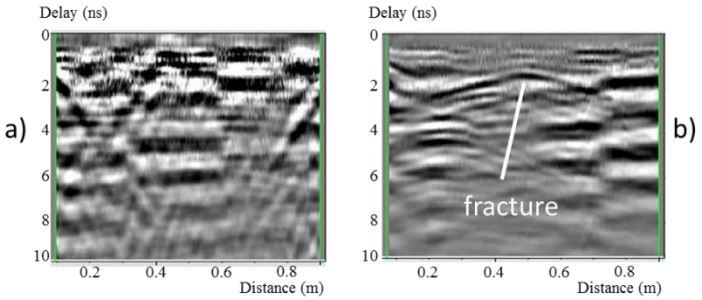


*Figure 4.11: Brick sample comparison: (a) 0 mm and (b) 10 mm configurations*

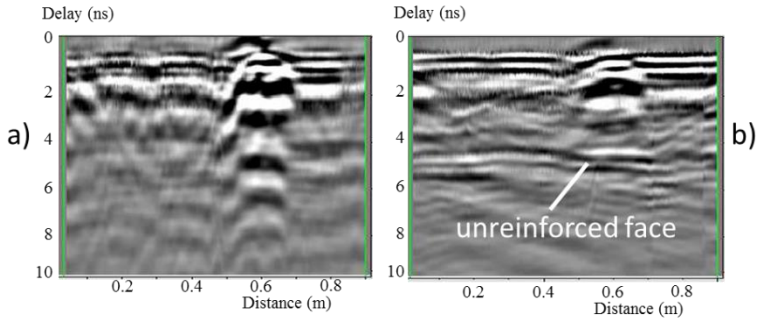


*Figure 4.12: Tuff sample comparison: (a) 0 mm and (b) 10 mm configurations*

The GPR sections analysis show that, where a dielectric material layer (Plexiglas) is interposed between the antenna and the sample, improvements were obtained both on reinforced and not reinforced face. In fact, we are able to improve the coupling, reducing the effects of the surface roughness and the attenuation due to the reinforcement, and it is also possible to discriminate the rear face sample- air- interface, together to the more "diluted" impedance contrasts between air-Plexiglas and Plexiglas-material as compared to the air-material case.

✓ 4.2.3.2 Time-slices

Time-slices are two-dimensional maps, made at different times from the 3D data cube (*x*, *y*, *t*), by summing the scattering energy within a fixed thickness window: 50 or 100 mm, suitable for the geometry of the sample.

The time-slices obtained from the profile acquired on the reinforced face, related to increasing depths (5-10 cm; 10-15 cm; 15-20 cm) for the 4 configurations (without and with Plexiglas of different thicknesses) are drawn with the aim to understand the spatial distribution of the anomalies and evaluating the resolution capability of the GPR system. The zero-depth reference is taken on the reinforced face.

- Bricks sample

Time-slices reported in Fig. 4.13 are related to the depth of 5-10 cm obtained from the profile acquired on the reinforced face, the most significant in this particular case in identifying the most stressed areas.

On the whole, there is a high scattering area in correspondence of the main diagonal, where the sample is more fractured as a result of the load. This effect is more evident

without the Plexiglas interposition, while with the dielectric layer a highly scattered area in the southern part of the sample is also highlighted.

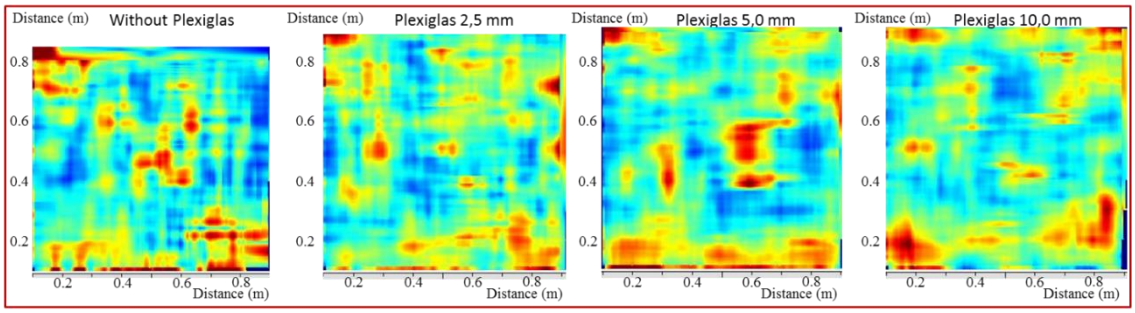


*Figure 4.13: Bricks sample: time-slices related to 5-10 cm depth drawn for the four configurations: without Plexiglas with a 2.5, 5.0 and 10.0 mm thick Plexiglas layer. Color scale in normalized units*

- Tuff sample

For the tuff sample, in Fig. 4.14 are reported the time slices related to a depth of 10-15 cm, obtained from the profile acquired on the reinforced face. These plots give homogenous results among the different configurations employed: the higher GPR scattering is indicative of the fractured zone (along the main diagonal), as a consequence of the high level of stress reached by the masonry in this zone.

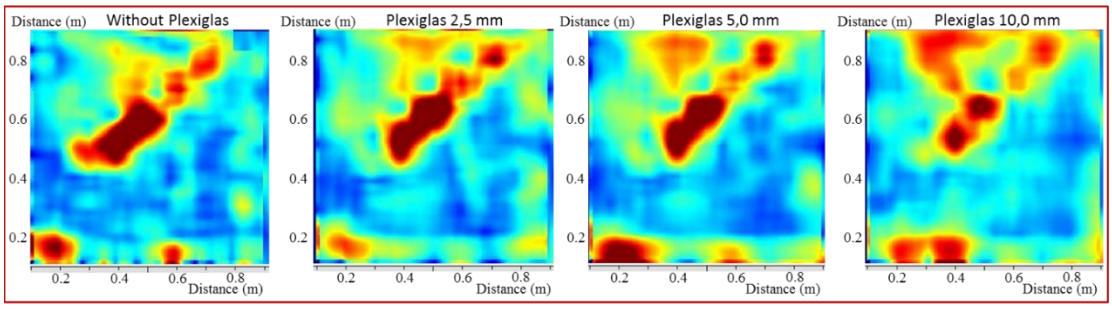


*Figure 4.14: Tuff sample: time-slices related to 5-10 cm depth drawn for the four configurations: without Plexiglas with a 2.5, 5.0 and 10.0 mm thick Plexiglas layer. Color scale in normalized units*

✓ 4.2.3.3 ERT

Since ERT acquisitions was not feasible on the reinforced face due to the high conductivity of the reinforcement, we present in Fig. 4.15 left, the results of inversion of ERT data acquired on the unreinforced face of the tuff sample, compared with the

corresponding GPR time-slice of Fig. 4.13 related to 5-10 cm depth, acquired on the reinforced face instead.

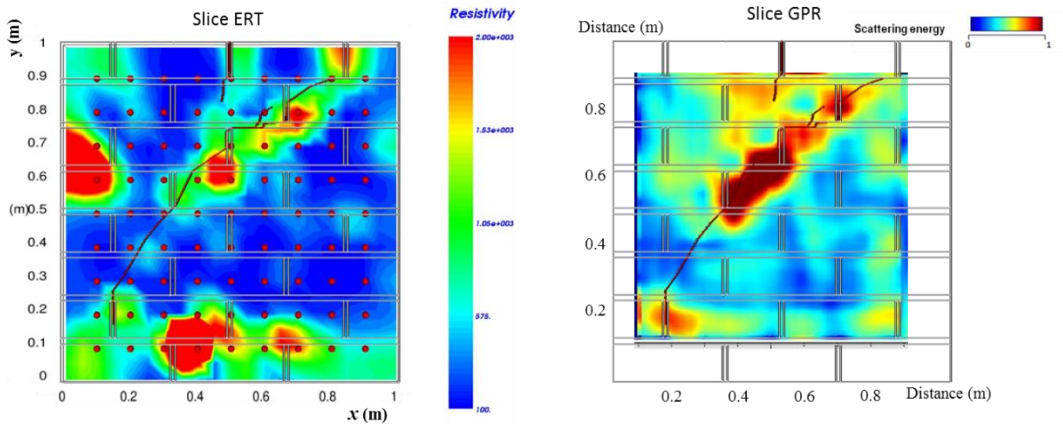


*Figure 4.15: After load application tuff sample comparison: ERT resistivity inverted model (left) GPR time slice by interposing 2.5 mm thick Plexiglas (right). GPR color scale in normalized units*

Both the investigation of the sample (ERT and GPR) gives homogeneous results among the techniques employed: good overlap between the high GPR scattering and the high ERT resistivity can be noted in the fractured zone, indicating a high level of stress of the masonry (Fig. 4.15).

### ✓ *4.2.4 Summary*

In this preliminary phase the potential of the proposed method for monitoring a static load test has been confirmed. In particular, it was demonstrated how the interposition of a dielectric material between the antenna and the masonry improved the response in terms of resolution and depth of investigation, particularly for investigations carried out on the unreinforced face of the samples.

Given these results, we plan to monitor a load test, with measurements performed both before and after the load application (under load was technically unfeasible due to safety reasons), in order to understand potential and limits of the combined use of GPR and ERT techniques for load test monitoring.

## 4.3 Load test monitoring

Both GPR and ERT data were recorded on the sample surface before and after the application of a shear-compression diagonal load. Differently from the preliminary phase,

GPR dataset was also analysed in non-conventional mode, by means of the picking of the arrival times of the EM wave on the back face of the wall samples in order to detect the effect of the fractures caused by the application of load.

From the indications obtained in the preliminary phase, we also acquired the data by interposing a dielectric medium (Plexiglas) between the investigated surface and the GPR antenna for improving the vertical resolution of the superficial layer, to avoid the direct wave overlapping in order to reduce limitations related to a non-optimal coupling and sliding between antenna and masonry and to improve the penetration and the signal strength in the presence of conductive materials according to Slob (2002).

### ✓ *4.3.2 Samples geometry*

The samples were made by the Department of Structural and Geotechnical Engineering, with the same physical and geometric characteristics of those seen at the synthetic and preliminary phases (Fig. 3.4). Although the applied load is the same of the preliminary phase (Fig. 4.5), the fracturing pattern is different, as reported in Figs. 4.16 and 4.17. As a result of the stress, the geometrical survey of the panels and the location of the fractures detected on the sample has been carried out such as in the following figures.

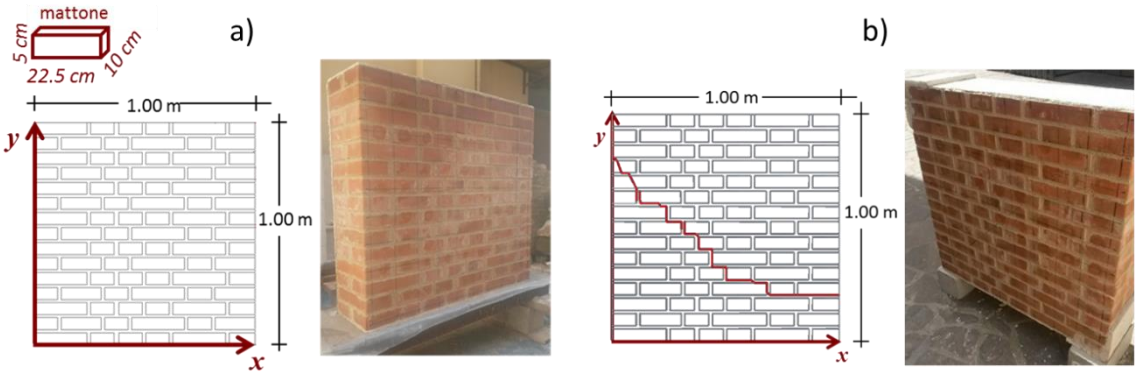


*Figure 4.16: Model of panel (left) and image of brick sample (right) both a) before and b) after the load application*

In particular, after the load application, in correspondence of the top-left and bottom-right corners, the main fracture is located for both cases mainly at the joints between adjacent bricks as shown in Fig. 4.16b for the bricks sample and in Fig. 5.17b for the tuff panel.

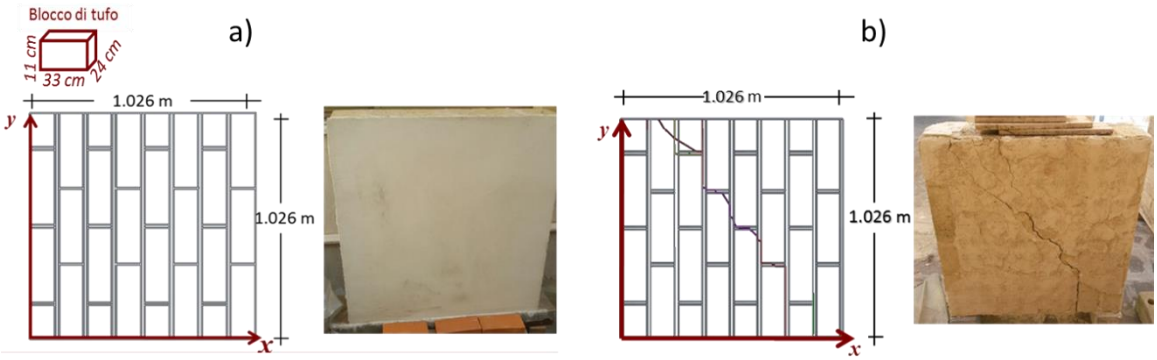


*Figure 4.17: Model of panel (left) and image of tuff sample (right) both a) before and b) after the load application*

### ✓ *4.3.3 Data acquisition and processing*

#### ✓ 4.3.3.1 GPR Data acquisition

GPR survey was performed with the IDS Aladdin 2 GHz antenna: an advanced radar for non-destructive subsurface structural analysis, particularly suitable for the required degree of resolution and for the nature of the resistive investigated media. The size of the lightweight (2 kg) antenna is 12.4 x 12.4 x 18.5 cm.

The system is equipped with a bipolar antenna (Fig. 4.18) polarized in two normal directions. The dual polarization enables to acquire four-components of the electromagnetic field.

Data acquisition encompasses the recording of the four-component electric field for each point, with parallel y-directed antennas (channel 1), parallel x-directed antennas (channel 2), y-directed source and x-directed receiver (channel 3), and x-directed source and y-directed receiver (channel 4) orientations (Orlando, 2007; Van der Kruck et al., 2003) (Fig. 4.19).

In the present study only the co-polar data with parallel broadside with y- and x-directed antennas were analysed.

Two-component data are sufficient to compute a single multicomponent image because with four-component data (two independent source components and two independent receiver components) two nominally equivalent images are obtained (Streich & Van der Kruk, 2007a). In three of the four surveys two-component data are available, but for the fourth survey only parallel broadside data were collected. It was found that the images obtained from the vector algorithm using only single component data as described in

Streich & Van der Kruk (2007b) are qualitatively comparable with the images obtained from the multicomponent algorithm applied to two-component data as described in Streich & Van der Kruk (2007a). For our data line spacing is too large to apply the imaging algorithms on the ten or six lines with a cross-line spacing of 10 cm. Streich & Van der Kruk (2007b) concluded that the quality of images obtained from vector migration algorithms are independent of the antenna orientation, provided the subsurface objects exhibit no polarimetric scattering effects.

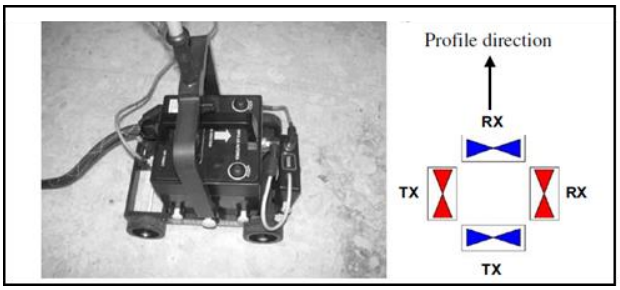


*Figure 4.18: 2 GHz bipolar antenna with dipoles placed normal to each other.*

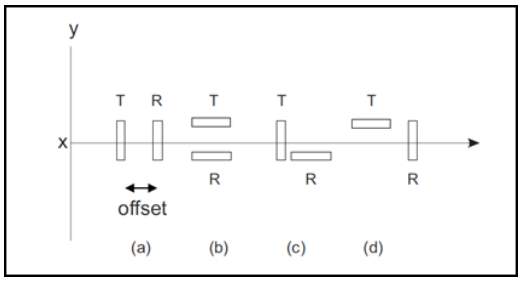


*Figure 4.19: Geometry of the four different antenna configurations. Just the data of the first two configurations are analyzed in the present work.*

Similarly to the preliminary tests, the survey was carried out on both faces of the panels, in order to evaluate the influence of the reinforcement on the GPR data.

Considering the geometry of the samples and the size of the GPR antenna, data were acquired on a regular grid, with x- and y-directed profiles spaced 0.1 m apart (9 profiles for each direction). Although a denser sampling of GPR profiles is theoretically possible, we prefer to adopt a cost-effective sampling, directly applicable for common field surveys, in order to make a trade-off between the resolution needed and the costs.

Each profile was acquired with a trace increment of 3.3 mm, with a time window of 15 ns, a sampling rate of 0.03 ns and an offset from the external boundary of 8 mm in the direction of acquisition and 10 mm in the normal direction (Fig. 4.20).

After the preliminary tests, the four different Plexiglas configurations has been re-implemented (Fig. 4.20).

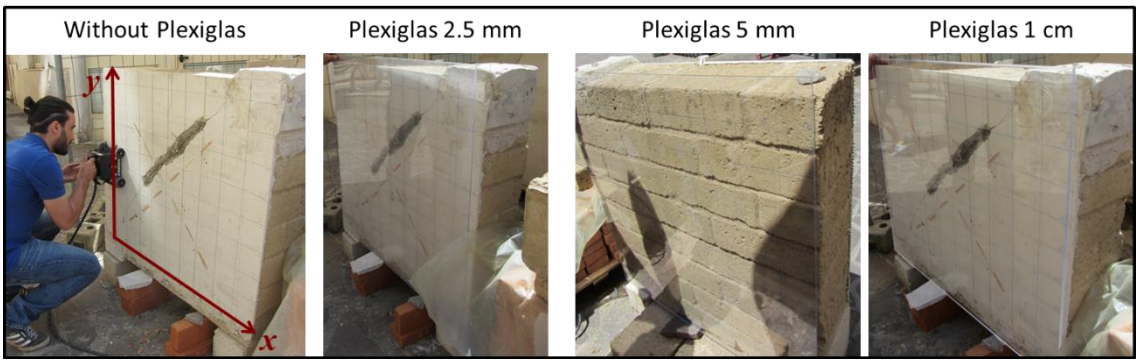


*Figure 4.20: Acquisition setup*

Therefore, we have four datasets for each face of the wall for both samples (tuff and bricks) in undisturbed and fractured configurations.

- ✓ 4.3.1.2 GPR data processing

The data were processed by means of the standard procedure seen before (GPR profiles and time-slices) and of an advanced analysis, encompassing the picking of the EM wave arrival time from the rear face of the sample and the analysis of the signal attenuation.

- ✓ 4.3.1.2.1 Standard processing

A standard processing of GPR data has been carried out using the same functions described in Chapter 4.2, for the preliminary tests: zero-time correction, band-pass filter (200-1900 MHz), background removal and a Stolt migration.

For the time to depth conversion we used a constant velocity of 12 cm/ns for the bricks sample and 11 cm/ns for the tuff sample. The velocities were obtained on analysing the diffraction hyperbola produced by the edge of the blocks and from the picking of the EM wave travel time to and from the rear face of the samples.

In the following sections, processed data are discussed by means of profiles and time-slices.

In addition to this standard processing, we aim to have an estimation of the relative dielectric constant (or relative electrical permittivity) variation within the samples, as an effect of the load test, aims to improve the response in terms of horizontal resolution in detecting sub-vertical fractures. In fact, comparing the dielectric constant calculated before and after the load application, information about the different electromagnetic

response related to the stress effect may be retrieved, in order to understand how the stress affects the material.

✓ 4.3.1.2.2 Picking of the EM wave arrival time

The effective dielectric constant variation of the different samples induced by the stress can be derived from the analysis of the reflection time from the rear face of the sample. This goal can be achieved through the picking of the EM wave travel time to and from the rear face of the sample ($t_p$) for each position *(i, j)* where *i* = 1, 2, ..., *N* and *j* = 1, 2, ..., *M*, being *N* the number of traces and *M* the number of profiles. In fact, under the hypothesis of dielectric media, that holds for $(\frac{\sigma^2}{\omega\varepsilon})^2 \ll 1$, we have:

$$\varepsilon_r{}^{(i,j)} = \left(\frac{c \cdot t_p{}^{(i,j)}}{2s}\right)^2 \tag{4.1}$$

where *c* is the speed of light and *s* the thickness of the sample (0.25 m in this case). The above mentioned hypothesis holds for resistivities > 100 Ωm. Laboratory 1D electrical measurements (single quadrupole) performed on single tuff blocks and bricks give a resistivity value around 500 and 300 Ωm, respectively. Once $t_p$ and *s* are known, we can determine the EM-wave velocity and consequently perform the time-depth conversion of the above mentioned time-slices.

Finally, the effectively sampled points for each layer have been arranged into two maps (one for each direction), in a way to obtain a matrix where each trace (*i,j*) is associated to the travel time $t_p$.

Because $t_p$ depends on the relative permittivity, by overlapping the longitudinal and transversal maps for each configuration, we were able to evaluate the effective variation of the electric permittivity of each sample, before and after the load application.

✓ 4.3.1.2.3 Mean absolute amplitude

GPR data were also analysed by means of the mean absolute amplitude (MAA) of the recorded signal, in order to understand in a first approximation, the zones where the GPR signal is more or less attenuated, as a result of the particular geometry of the sample (before the load test) and of the load application (after the load test). The MAA was calculated for each trace within a time window $t_w = (0, \frac{t_p}{2})$.

For the trace position *(i, j)* we have:

$$MAA^{(i,j)} = \frac{1}{L^{(i,j)}} \sum_{k=1}^{L^{(i,j)}} \left| A_k^{(i,j)} \right| \tag{4.2}$$

Where *A* is the signal amplitude and *L* the number of time steps for each trace *i* at the profile *j*.

- ✓ 4.3.3.2 ERT data acquisition

Similarly to the preliminary phase, GPR and ERT technique were jointly applied on the unreinforced face of the samples, because the survey on the fibre-reinforced face was unfeasible due to the high-conductivity of the steel-basalt fiber fabric that prevents the investigation of the deeper layers.

Differently to the preliminary investigation, where we used nails driven into the wall as electrodes, a completely non-invasive dedicated system was created, as seen in Fig. 4.20 in order to avoid any damage to the masonry.

In particular, the geo-electrical dataset was acquired using 36 non-invasive cylindrical copper plates as electrodes (diameter = 3 cm, thickness = 3 mm), fixed on the wall through a 1 x 1 m Plexiglas plate, while clamps and a conductive gel contribute to improve the electrodes-sample coupling (Fig. 4.21). The electrodes are organized in 4 rows of 9 electrodes each and they are progressively moved from the bottom to the top of the sample, overlapping two rows for each position shift. Data were acquired using the IRIS Syscal Pro 48 resistivimeter with a three-dimensional dipole-dipole "snake" array for each position, leading to 3426 apparent resistivity measurements for each configuration (tuff and bricks, before and after the load test).

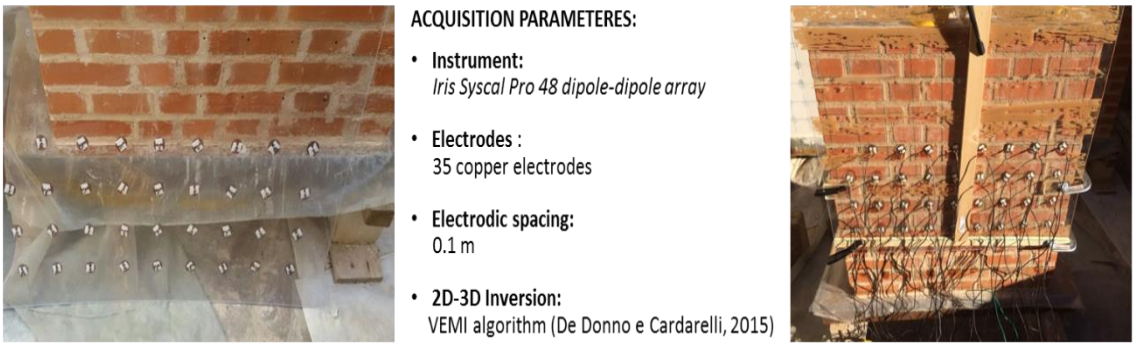


*Figure 4.21: ERT acquisition parameters*

Apparent resistivity data were inverted using the VEMI algorithm (De Donno & Cardarelli, 2016), a Matlab-based open-source algorithm included in EIDORS (Adler and Lionheart, 2006), able to invert 3D electrical data, using a finite element approach with tetrahedral elements for solving the forward problem (De Donno & Cardarelli, 2014) and a Gauss-Newton procedure with optimized damping for inversion (De Donno, 2013). A Neumann-type boundary condition was imposed on the whole faces of the panels, in order to simulate the absence of current flow through the air-panel interface, differently from a standard geo-electrical process, used for example by ERTLab in Chapter 4.2.

### ✓ *4.3.4 Results*

The GPR results, for the bricks and tuff sample are analysed below as function of the different type of configuration, before and after load application.

The benefit of the Plexiglas interposition between surface and antenna was early explored thoroughly with laboratory data by the analysis of the GPR profiles acquired on the fibre reinforced face of the panel in the preliminary phase (Figs. 4.11 and 4.12). Therefore, in this step we focus our attention only on the data acquired on the unreinforced face in order to evaluate the stress effect on the GPR response. The obtained results are directly comparable with the synthetic examples discussed in Chapter 3. On these examples we fully apply the processing procedure (radargrams, time-slices, maps of the dielectric constant and of the mean absolute amplitude).

#### ✓ 4.3.4.2 GPR Profiles

GPR x and y- directed profiles, acquired in the mid-section of the bricks sample ((y = 0.5 m and x = 0.5 m) are represented in respectively in Figs. 4.22-4.23, while the x and y-directed profile acquired on the tuff panel in Figs. 4.24-4.25.

- Bricks sample

The GPR profiles acquired on the unreinforced face of the bricks sample, without and with 2.5, 5 and 10 mm of Plexiglas before (respectively a, b, c, d) and after (respectively e, f, g and h) the load application are presented in Fig. 4.22 for the x-directed and 4.23 for the y-directed profiles, respectively.

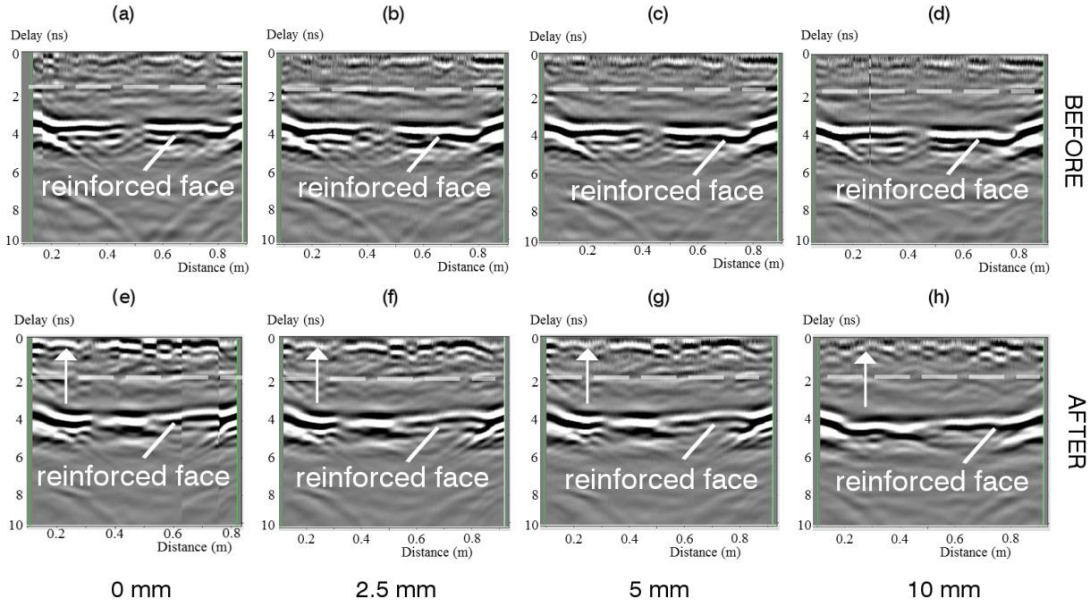


*Figure 4.22: Laboratory bricks sample. Example GPR x-directed profile at y = 0.5 m acquired on the unreinforced face before the load application without (a) and with 2.5 (b), 5 (c) and 10 mm of Plexiglas (d). GPR x-directed profile at y = 0.5 m after the load application without (e) and with 2.5(f), 5 (g) and 10 mm of Plexiglas (h). The white dashed line indicates the end of the first row of bricks. The white arrows indicate the location of the main fracture*

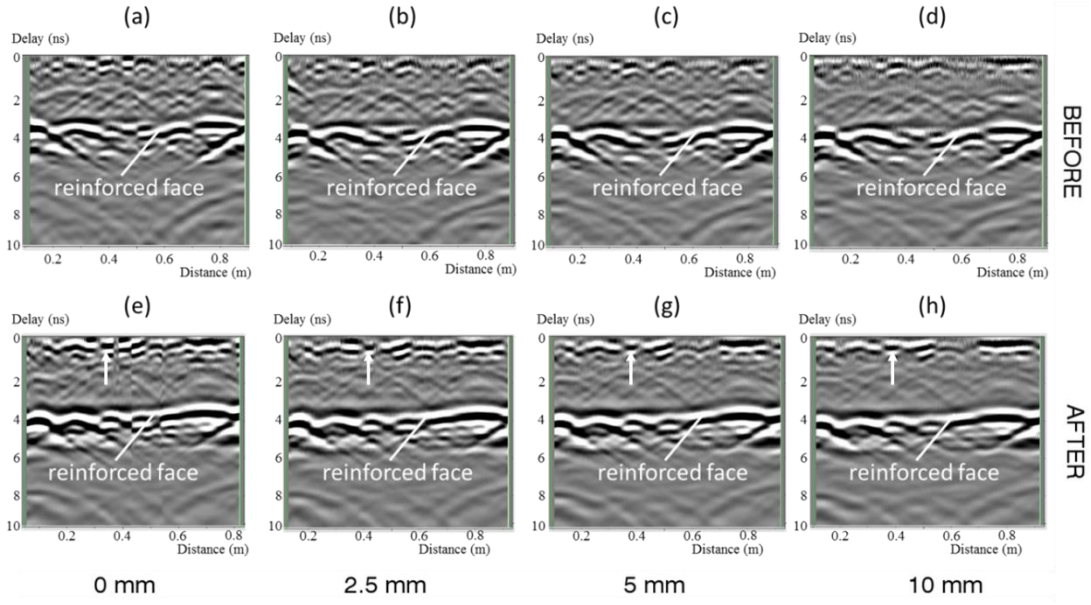


*Figure 4.23: Laboratory bricks sample. Example GPR y-directed profile at x = 0.5 m acquired on the unreinforced face before the load application without (a) and with 2.5 (b), 5 (c) and 10 mm of Plexiglas (d). GPR y-directed profile at x = 0.5 m after the load application without (e) and with 2.5(f), 5 (g) and 10 mm of Plexiglas (h). The white arrows indicate the location of the main fracture*

The GPR profiles related to the bricks panel (Figs. 4.22-4.23) highlight both the reinforced face and the interface between the two rows of bricks (dashed line) with all the four configurations.

However, before the load application, the x-directed sections are able to better discriminate the interface between the two rows of bricks (Fig. 4.22 a-d), while the y-directed profiles show more diffraction hyperbolas due to the edges of single bricks and the small dimension of bricks in that direction (Fig. 4.23 a-d).

The mortar joints remain hidden and we can notice an increase in heterogeneity where a static load has been applied (Figs. 4.22-4.23 e-h). The fracture gives a response comparable to that of a joint between bricks and therefore it is not easy to detect it in the vertical profiles.

- Tuff sample

The GPR profiles acquired on the unreinforced face of the tuff sample, without and with 2.5, 5 and 10 mm of Plexiglas before (respectively a, b, c, d) and after (respectively e, f, g and h) the load application are presented in Fig. 4.24 for the x-directed and 4.25 for the y-directed profiles, respectively.

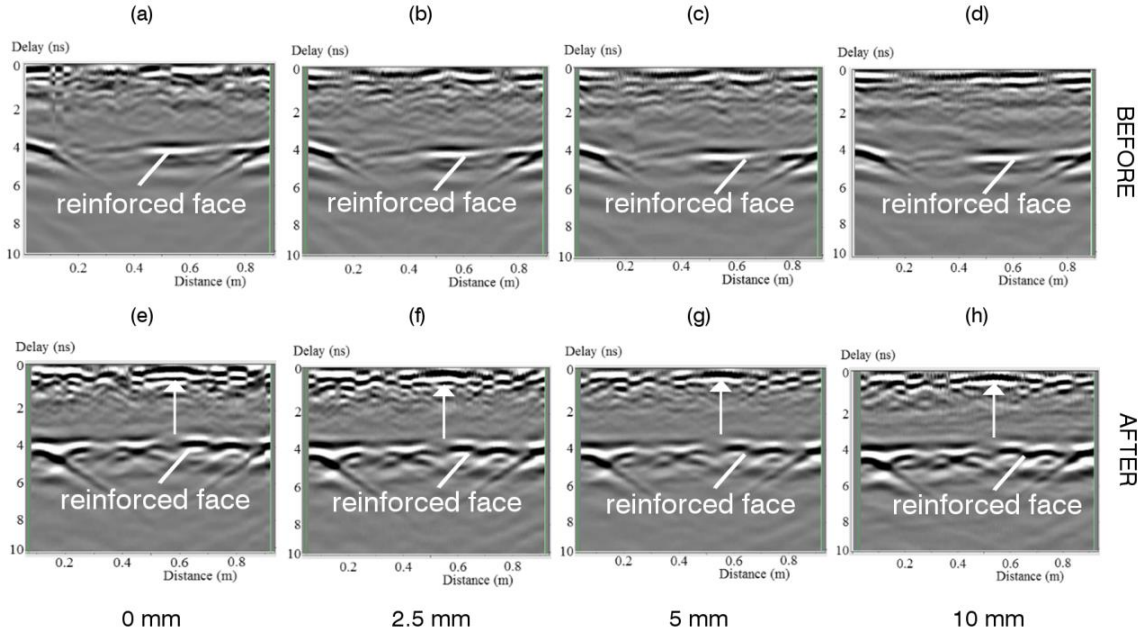


*Figure 4.24: Laboratory tuff sample. Example GPR x-directed profiles at y = 0.5 m acquired on the unreinforced face before the load application without (a) and with 2.5 (b), 5 (c) and 10 mm of Plexiglas (d). GPR x-directed profiles at y = 0.5 m after the load application without (e) and with 2.5 (f), 5 (g) and 10 mm of Plexiglas (h). The white arrows indicate the location of the main fracture*

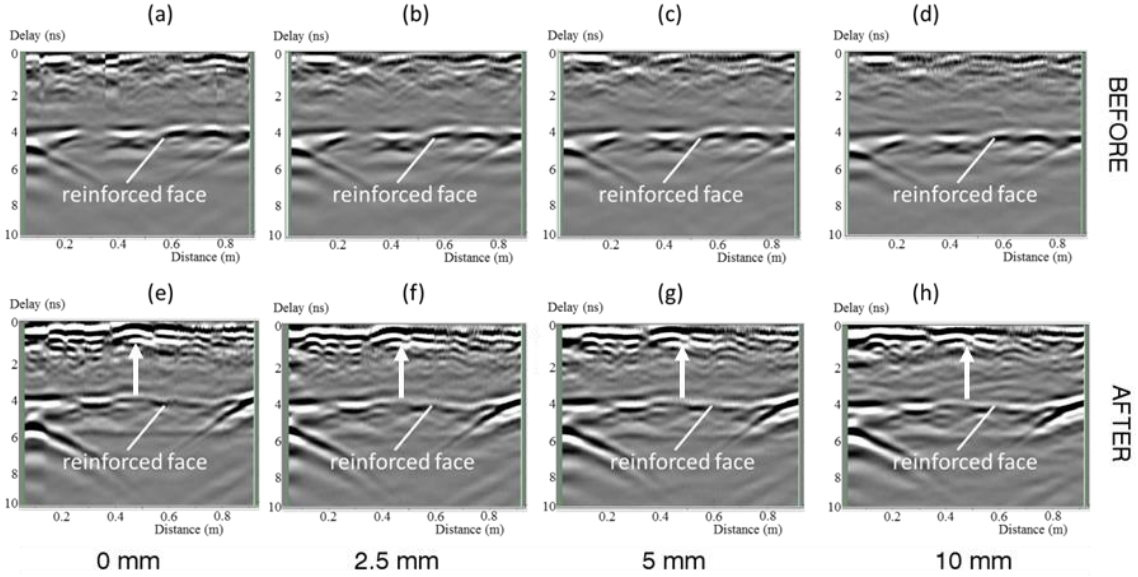


*Figure 4.25: Laboratory tuff sample. Example GPR y-directed profile at x = 0.5 m acquired on the unreinforced face before the load application without (a) and with 2.5 (b), 5 (c) and 10 mm of Plexiglas (d). GPR y-directed profile at x = 0.5 m after the load application without (e) and with 2.5 (f), 5 (g) and 10 mm of Plexiglas (h). The white arrows indicate the location of the main fracture*

The GPR profiles related to the tuff panel (Figs. 4.24-4.25) display an analogous behaviour with respect to the bricks (Figs. 4.22-4.23) and to the respective synthetic radargram of Fig. 3.6. In fact, the reinforced face is always well-detected (Fig. 4.24-4.25) without significant differences among the different Plexiglas configurations, as expected after the theoretical simulations. After the load test (Figs. 4.24-25e-h) the first part of the radargram (t = 0-2 ns) is more heterogeneous due to the presence of fractures. The joints between the blocks are not clearly detected, compared to the synthetic examples, due to the roughness of the investigated surface and heterogeneity of the sample.

However, where a dielectric material layer (Plexiglas) is interposed between the antenna and the sample, we are able to improve the coupling, and therefore reduce the roughness material effects and signal attenuation. In fact, the survey made with the antenna directly on the wall surface is strongly affected by the roughness and the surface irregularities, and the correct length of the profile is underestimated (as shown by the red arrow in Fig. 4.26a). Instead, this issue is not emerged where a Plexiglas layer was interposed (red arrow in Fig. 4.26b). Also in this case the fracture is not well detected by vertical profiles both without and with Plexiglas.

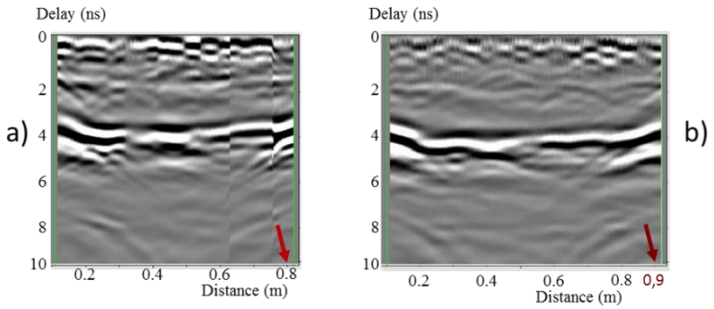


*Figure 4.26: Brick sample comparison: (a) survey with the antenna in direct contact with the sample, (b) survey with a Plexiglas layer interposed between the two objects. The red arrows highlight the different length of the two profiles*

✓ 4.3.4.2 Time-slices

We have analysed three time-slices, related to increasing depths and to the four antenna configurations (without and with Plexiglas of different thicknesses), in order to better discriminate the anomalies with the depth for the prefixed thickness window. In particular, on the basis of the size of the sample, the spatial intervals were chosen as depth of 5-10 cm; 10-15 cm; 15-20 cm.

The time-slices confirm the main issue underlined by the numerical simulations: where the antenna is place directly on the surface we have a higher resolution with higher reflectivity at the joints although signal is more scattered.

Figs. 4.27-4.29 for the brick sample and Figs. 4.32-4.34 for the tuff sample show the time-slices related to GPR data acquired before and after the load application.

- Bricks sample

The time-slices obtained from the longitudinal and transversal profile acquired on the unreinforced face, for the 4 configurations (without and with Plexiglas of different thicknesses), before (a, b, c, d) and after (e, f, g, h) the load application are drawn in Figs. 4.27, 4.28 and 4.29. They are related to a depth of 5-10 cm, 10-15 cm and 15-20 cm respectively.

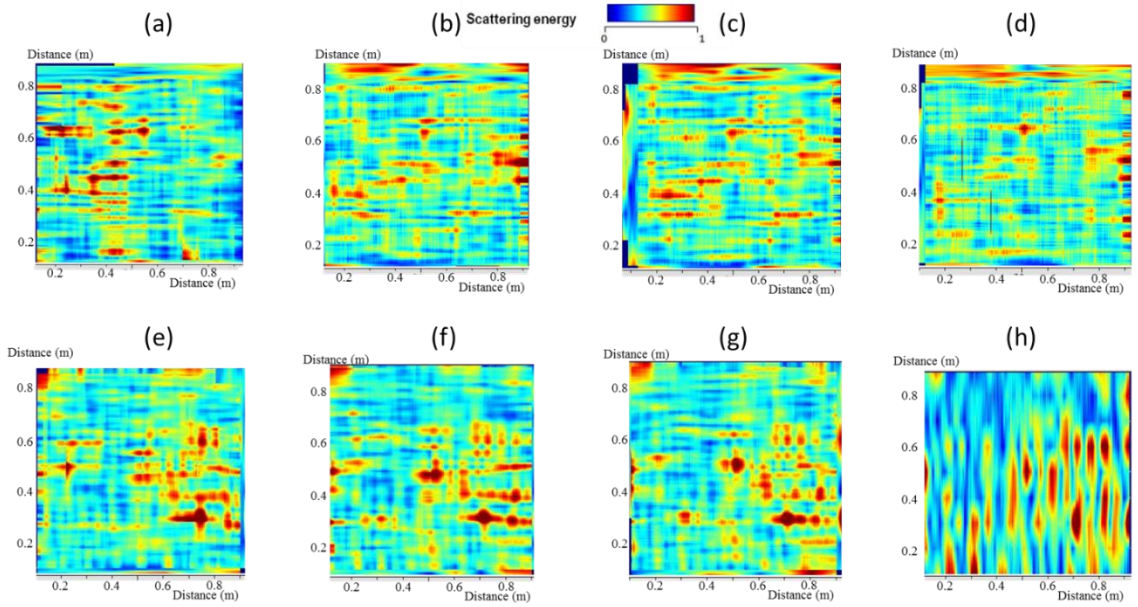


*Figure 4.27. Laboratory bricks sample. GPR time-slice at the depth 5.0-10.0 cm, before the load application without (a) and with 2.5 mm (b), 5 mm (c), 10 mm (d) of Plexiglas. GPR time-slice after the load application without (e) and with 2.5 mm (f), 5 mm (g), 10 mm (h) of Plexiglas. Time slices are drawn considering both x- and y-directed profiles (colour scale in normalised units)*

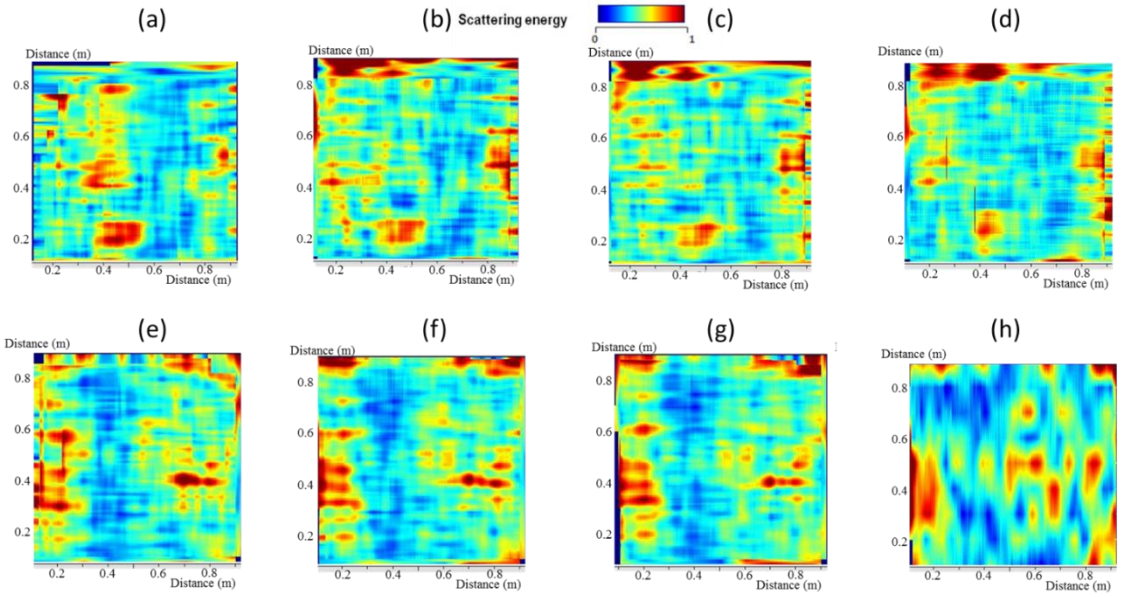


*Figure 4.28. Laboratory bricks sample. GPR time-slice at the depth 10.0-15.0 cm, before the load application without (a) and with 2.5 mm (b), 5 mm (c), 10 mm (d) of Plexiglas. GPR time-slice after the load application without (e) and with 2.5 mm (f), 5 mm (g), 10 mm (h) of Plexiglas. Time slices are drawn considering both x- and y-directed profiles (colour scale in normalised units)*

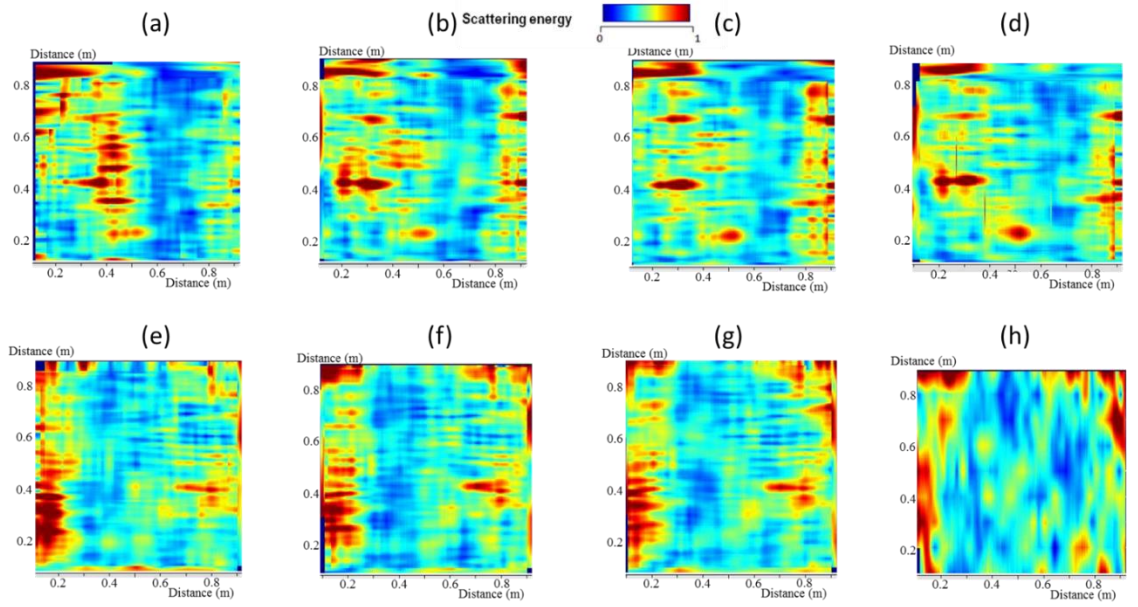


*Figure 4.29. Laboratory bricks sample. GPR time-slice at the depth 15.0-20.0 cm before the load application without (a) and with 2.5 mm (b), 5 mm (c), 10 mm (d) of Plexiglas. GPR time-slice after the load application without (e) and with 2.5 mm (f), 5 mm (g), 10 mm (h) of Plexiglas. Time slices are drawn considering both x- and y-directed profiles (colour scale in normalised units)*

Before the load application, the time slices show that the response strongly depends on the samples geometry according to the profile direction, confirming the evidence of the synthetic simulations. These results can be better analysed when the sample model is superimposed on the time slices (Fig. 4.30). In detail, as summarized in Fig. 4.30 by the time slices drawn at a depth of 5-10 cm (a), 10-15 cm (b) and 15-20 cm (c), the high-scattering area is located in correspondence of bricks arranged in a single row (red ellipse), while where the sample is built with two parallel rows of bricks the signal is less scattered (Fig. 4.30).

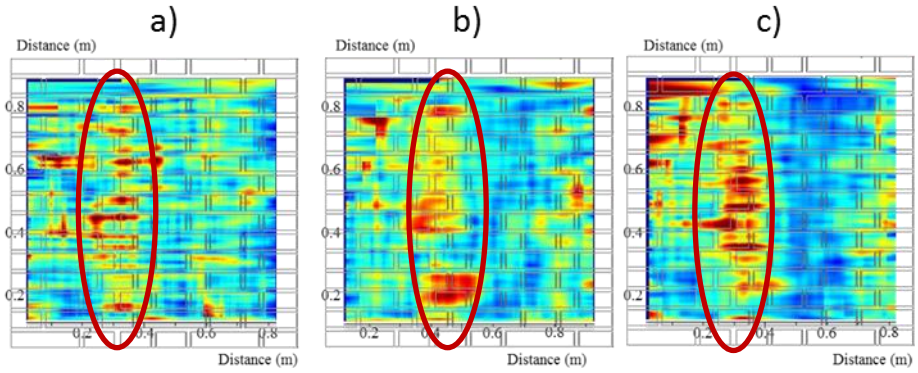


*Figure 4.30: Bricks sample: time slices at depth of 5-10 cm (a); 10-15 cm (b); 15-20 cm (c) analysis before the load application without Plexiglas*

As a result of the combined compressive and shear stress, the joints between the bricks are highly affected by the suffered stress and, differently from the undisturbed sample, the lower scattering area is located where bricks are arranged on a single row (Fig. 4.31). The high scattering seen at x=0-0.1 and at y=0.8-0.9 m is probably due to boundary effects.

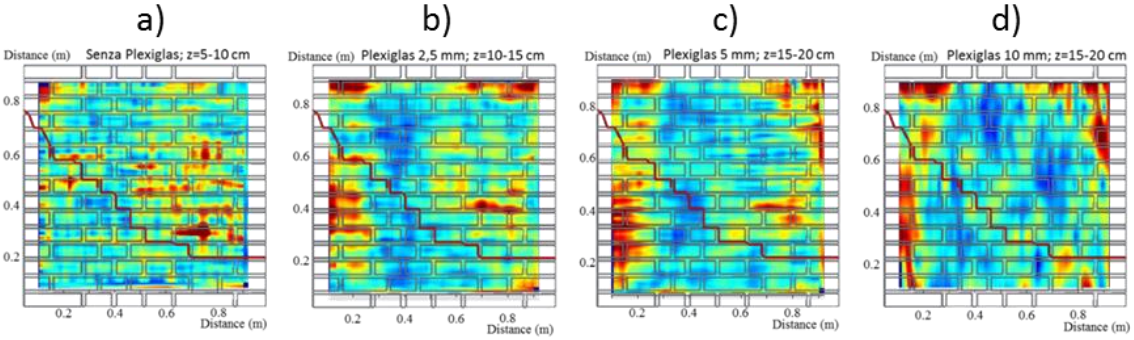


*Figure 4.31: Bricks sample: time slices analysis after the load application, with different configurations (0, 2.5, 5, 10 mm) and at different depth. Color scale in normalized units*

- Tuff sample

The time-slices related to the tuff panels are shown in Fig. 4.32 (depth=5-10 cm), Fig. 4.33 (depth=10-15 cm) and Fig. 4.34 (depth=15-20 cm) for the 4 configurations (without and with Plexiglas of different thicknesses), both before (a, b, c, d) and after (e, f, g, h) the load application.

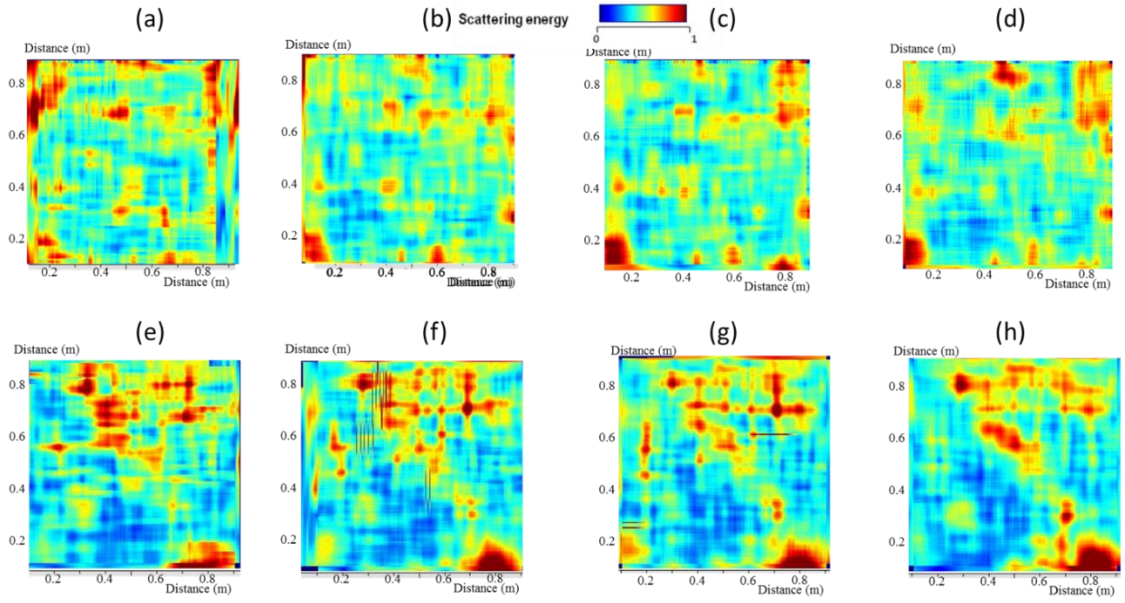


*Figure 4.32. Laboratory tuff sample. GPR time-slice at the depth 5.0-10.0 cm, before the load application without (a) and with 2.5 mm (b), 5 mm (c), 10 mm (d) of Plexiglas. GPR time-slice after the load application without (e) and with 2.5 mm (f), 5 mm (g), 10 mm (h) of Plexiglas. Time slices are drawn considering both x- and y-directed profiles (colour scale in normalised units)*

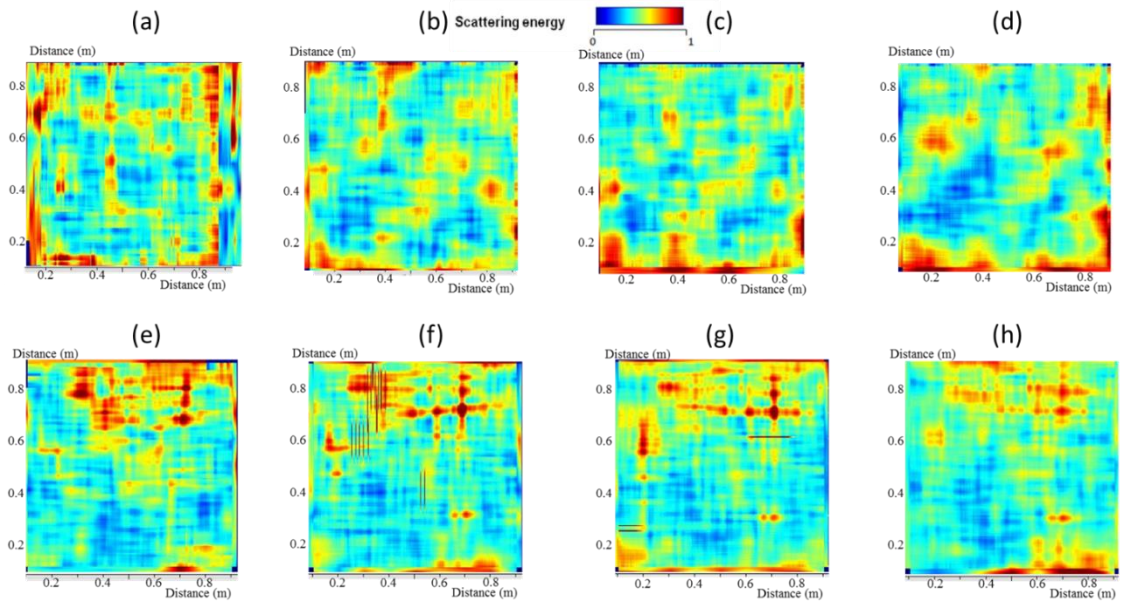


*Figure 4.33. Laboratory tuff sample. GPR time-slice at the depth of 10.0-15.0 cm before the load application without (a) and with 2.5 mm (b), 5 mm (c), 10 mm (d) of Plexiglas. GPR time-slice after the load application without (e) and with 2.5 mm (f), 5 mm (g), 10 mm (h) of Plexiglas. Time slices are drawn considering both x- and y-directed profiles (colour scale in normalised units)*

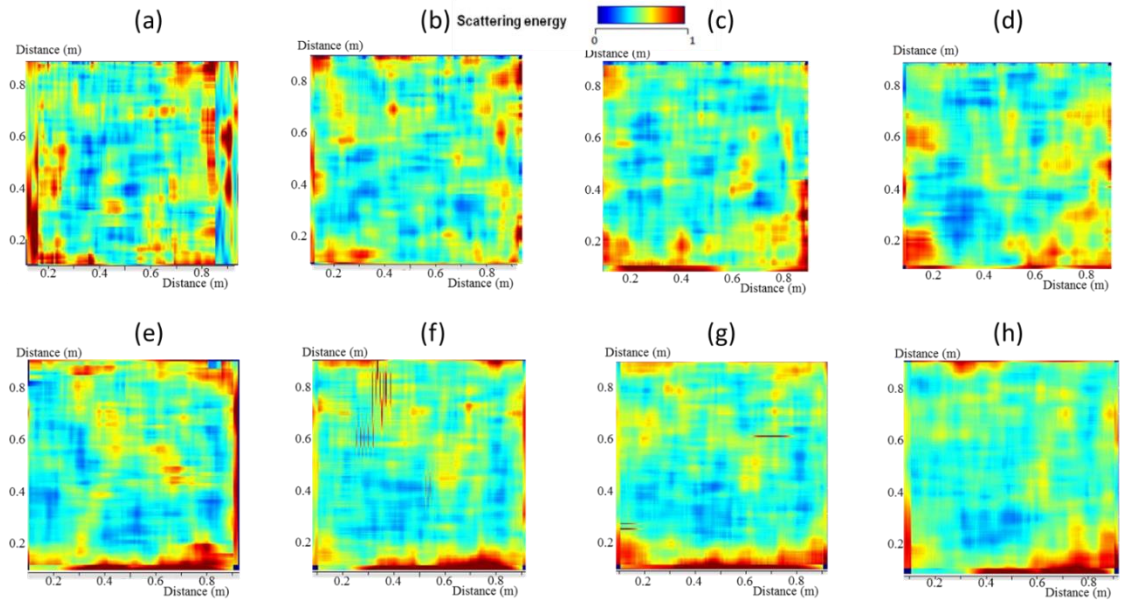


*Figure 4.34. Laboratory tuff sample. GPR time-slice at the depth 15.0-20.0 cm before the load application without (a) and with 2.5 mm (b), 5 mm (c), 10 mm (d) of Plexiglas. GPR time-slice after the load application without (e) and with 2.5 mm (f), 5 mm (g), 10 mm (h) of Plexiglas. Time slices are drawn considering both x- and y-directed profiles (colour scale in normalised units)*

The undisturbed models (Figs. 4.31a-d, 4.32a-d, 4.33a-d) show a heterogeneous behaviour, with higher reflectivity at the joints between tuff blocks.

Among the different configurations (Fig. 4.35), with or without Plexiglas, the response is quite similar, although more scattering occurs when the antenna is placed directly in contact with the sample, where we can notice a higher scattering due to the borders of the tuff blocks.

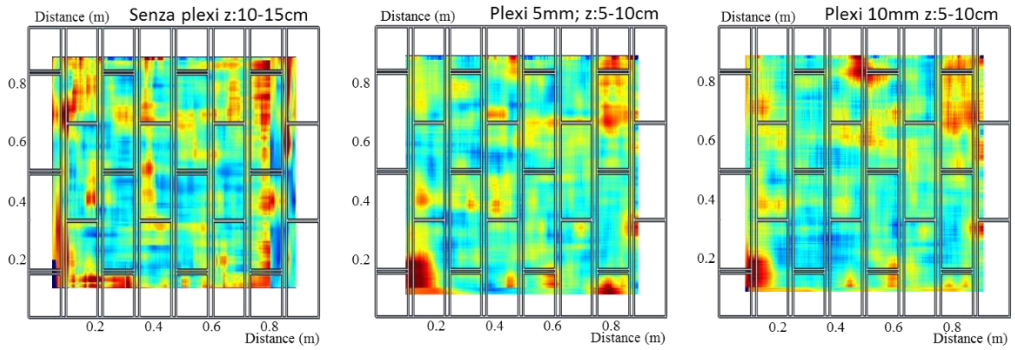


*Figure 4.35: Tuff sample: time slices analysis before the load application, with different configurations of Plexiglas (0, 5, 10 mm). Color scale in normalized units*

After the application of diagonal stress, it can be noticed two different responses between the top-right and the bottom-left parts, indicating how the stress has acted in a different way on the sample. The high intensity of scatter is probably due to a weakened zone, that is in the top-right zone of the sample.

This results are quite clear in Fig. 4.36 when the fractured sample model is superimposed on the time slices at depth 5-10 cm.

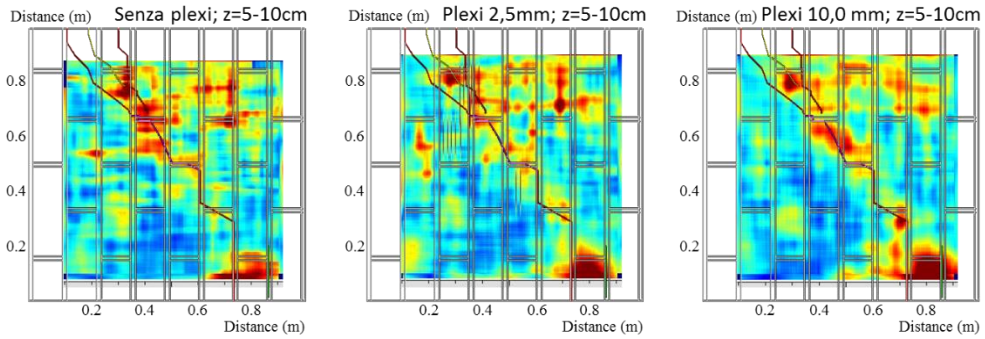


*Figure 4.36: Tuff sample: time slices at depth 5-10 cm analysis after the load application, with different configurations (0, 5, 10 mm). Color scale in normalized units*

Thus, we have shown the potential of the methodology to identify the main anomalies within the masonry sample. In particular, where a dielectric material layer is interposed

between the GPR antenna and the surface, we can improve the coupling, by reducing the effects of material roughness. While, in the case of undisturbed samples the response is strongly dependent on the sample geometry.

✓ 4.3.4.3 Dielectric constant

The effective dielectric constant variation of the different samples was obtained from the picking of the arrival time for each profile direction (longitudinal and transversal) and for each configuration, through eq. (4.1) of the reflection from the rear face of samples. In order to avoid possible errors due to interpolation, the effectively sampled points for each layer was mapped separately in the two main directions.

Figs. 4.37-4.40 shows the variation of the dielectric constant before and after the load application of the two samples, for the four different configurations. For the sake of simplicity, we narrow our analysis only considering the configuration no. 1 (without Plexiglas) and no. 4 (10 mm), for x- and y-directed profiles.

- Bricks sample

The dielectric constant maps calculated for the laboratory bricks sample before and after the load application without (c) and with 10 mm of Plexiglas (d) are presented in Fig. 4.37 and 4.38 for x- and y-directed profiles, respectively.

Data acquired in x- and y-directions before the load application are slightly different among themselves (Figs. 4.37-4.38a,b), while after the load application this effect is not significant. This could indicate that, before the load application, the dielectric constant depend mainly on the geometry of constructive materials, while after the load application on the suffered stress.

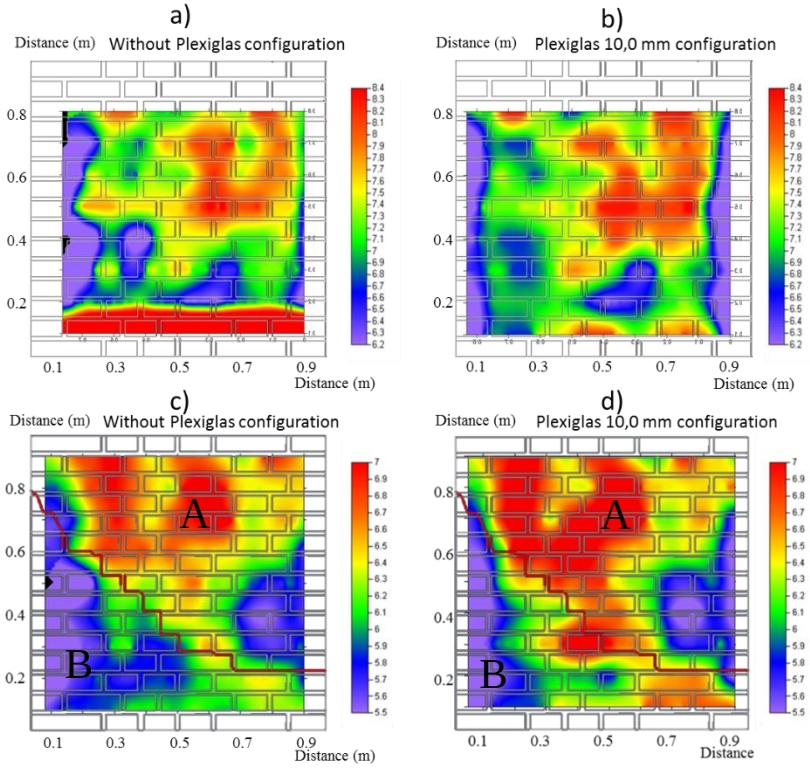


*Figure 4.37: Dielectric constant calculated for the laboratory bricks sample before the load application, without (a) and with 10 mm of Plexiglas (b), and after the load application without (c) and with 10 mm of Plexiglas (d). Maps are drawn considering only the x -directed profiles*

The maps of the dielectric constant (Figs. 4.37 and 4.38) confirm the evidences of the time-slices, namely that the GPR response, before load application, is principally conditioned by samples geometry.

The undisturbed bricks panel (Figs. 4.37a,b and 4.38a,b) displays higher $\varepsilon_r$ values (red zone) in correspondence of the single row of the bricks (black ellipse), while elsewhere $\varepsilon_r$ is lower. Such dependence on geometry is more evident in the case of the y-directed profiles, because this orientation of the bricks results to be uniform on the vertical direction (Fig. 4.38a,b). Overall the mean dielectric constant is around 7.5.

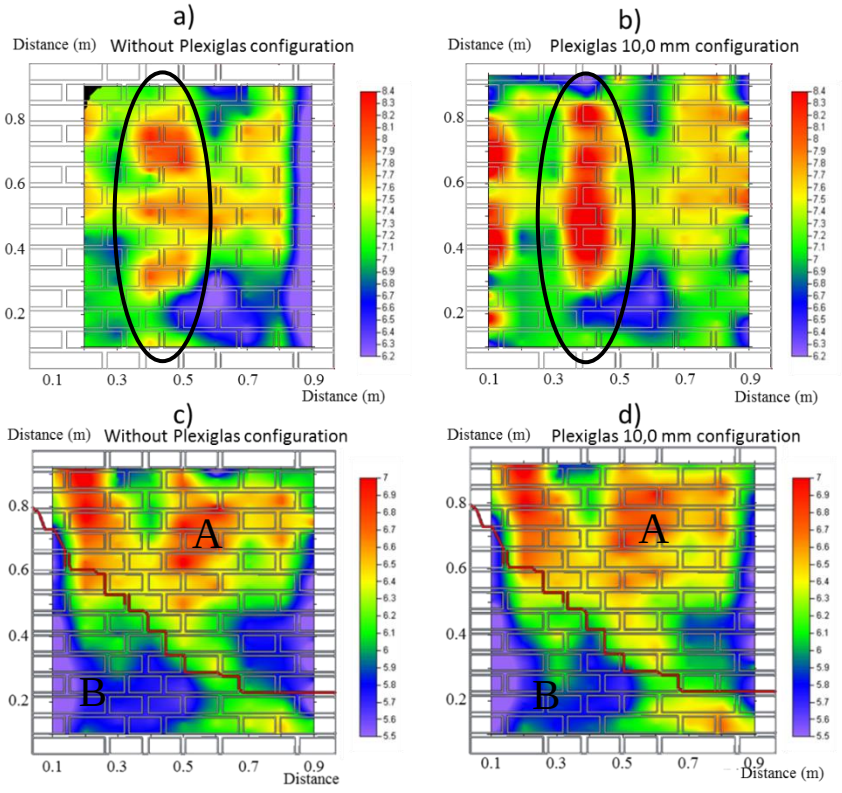


*Figure 4.38: Dielectric constant calculated for the laboratory bricks sample before the load application, without (a) and with 10 mm of Plexiglas (b), and after the load application without (c) and with 10 mm of Plexiglas (d). Maps are drawn considering only the y-directed profiles*

The applied stress causes a rearrangement of the dielectric constant into two main zones (A and B in the Figs. 4.37c,d and 4.38c,d): in the upper-left part we have higher $\varepsilon_r$ values (red zone - A: $\varepsilon \geq 7$) with respect to the bottom-left (blue zone - B: $\varepsilon \leq 5.8$), due to a higher stress level and therefore the fracturing is more intense in the zone B in the Figs. 4.38c,d. However, this effect is not so clearly visible in the respective time-slices of Figs. 4.31. At the end the Plexiglas layer does not produce a remarkable effect on these maps. Therefore, the EM velocities, before and after the load application tend to increase, in particular EM velocity range before any load application (i.e. cases a and b) is from about 10.3 up to 12.0 cm/ns, while after the stress the EM velocity range is from about 11.3 up to 12.8 cm/ns. Beside possible errors and uncertainties this range is quite large considering that the testing wall was built in laboratory and it could be therefore considered as "homogeneous". I expect that such velocity range should be even larger for actual GPR application when for instance the moisture content would also play an important role.

- Tuff sample

Even for the tuff panel, the dielectric constant maps calculated before and after the load application without (a, c) and with 10 mm of Plexiglas (b, d) are drawn separately for the x-directed (Fig. 4.39) and the y-directed profiles (Fig. 4.40).

In this case, the maps of the dielectric constant, both before and after the load application, do not present particular variations in relation to the direction of the profiles, except for boundary effects seen at the final part of the profiles.

Before the load application (Figs. 4.39a-4.40a), the response in terms of dielectric constant is almost heterogeneous (ε = 6-8) and mainly triggered by the samples geometry, whereas after the load test the sample has been rearranged as an effect of the stress undergone.

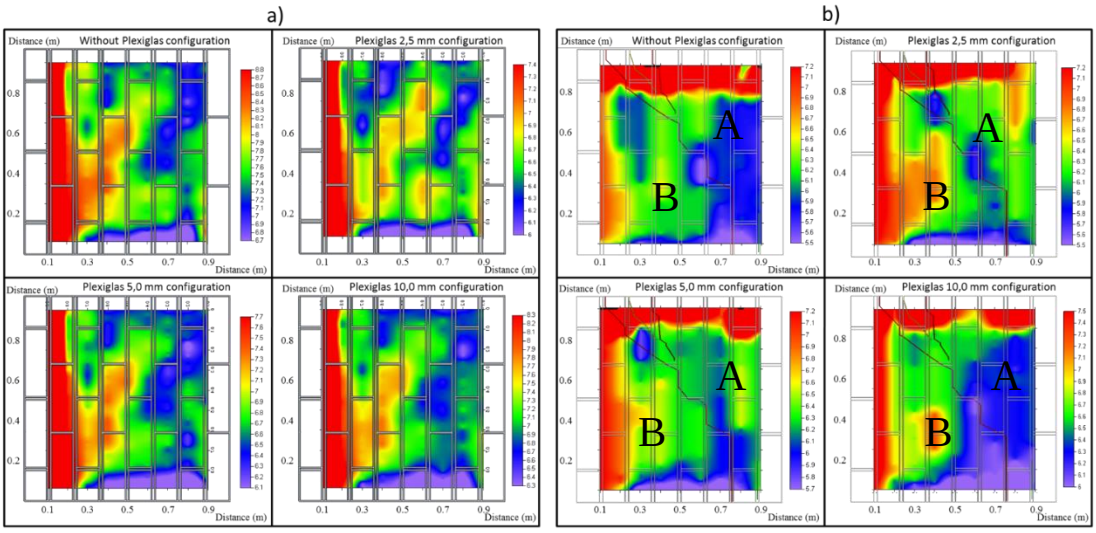


*Figure 4.39: Maps of the dielectric constant before (a) and after (b) load application for the bricks sample with the four different configurations. Maps are drawn considering only the y - directed profiles*

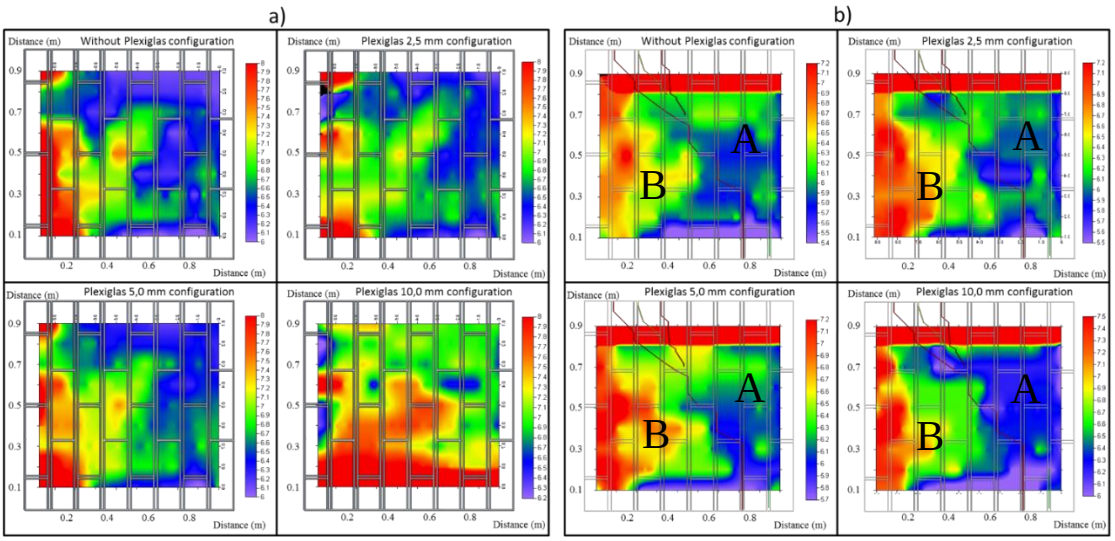


*Figure 4.40: Maps of the dielectric constant before (a) and after (b) load application for the tuff sample with the four different configurations. Maps are drawn considering only the x -directed profiles*

Before the load application, the tuff panel has a mean value of the dielectric constant around 7 (discarding the high values > 8, due to the effect of an adjacent steel beam at x = 0.1-0.2 m), lower than the bricks as expected. After the load test (Figs. 4.39b-4.40b) the mean value drops to 6 as a result of the intense fracturing occurred within the sample. Here, the panel is divided into two main zones: above the main fracture, with relative lower values of $\varepsilon_r$ (5.5-6.5) ("A" zone in Figs. 4.39b-4.40b) and below it where the dielectric constant is slightly higher (6.5-7.5) ("B" zone in Figs. 4.39b-4.40b).

✓ 4.3.4.4 Mean absolute amplitude

As the GPR pulse propagates in the medium, it suffers attenuation as the result of absorption and dispersion, besides spherical divergence. The quality of the GPR images is then strongly dependent on an adequate correction of the attenuation effects.
In this section, a study for the evaluation of changes in the attenuation is proposed, using the mean absolute amplitude of the GPR signal calculated using relation (4.2).

- Bricks sample

The maps of the mean absolute amplitude, obtained before the load applications (Fig. 4.41a,b) are quite homogenous. In particular, the MAA map of Fig. 4.41b, calculated from the GPR y-directed profiles with a 10 mm thick Plexiglas plate, exhibits a different behaviour according to the geometry of the bricks: the signal is strongly attenuated in

presence of a single row of bricks (black ellipse), as expected due to the higher conductivity of the bricks with respect to the mortar, while higher amplitude is retrieved elsewhere. This behavior is less evidence in the without Plexiglas configuration (Fig.4.41a).

As a result of the load test, the brick sample shows a higher signal amplitude (MAA = 8.5-10·$10^5$) in the bottom part ("B" zone in Figs. 4.41c,d) and a lower amplitude (MAA < 8·$10^5$) in the upper part ("A" zone in Figs. 4.41c,d) of the sample. This effect is enhanced for Plexiglas acquisitions (Figs. 4.41b,d).

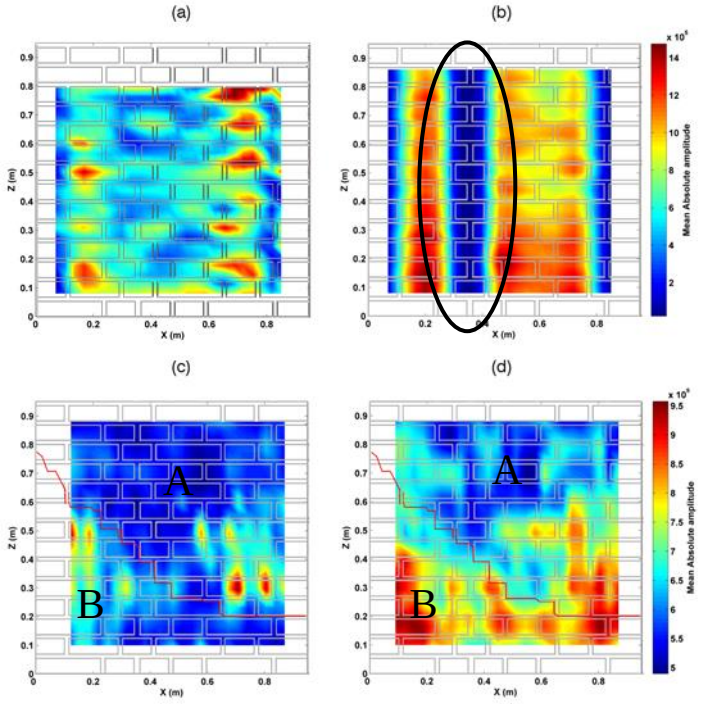


*Figure 4.41. Mean absolute amplitude calculated for the laboratory bricks sample before the load application, without (a) and with 10 mm of Plexiglas (b), and after the load application without (c) and with 10 mm of Plexiglas (d)*

- Tuff sample

The MAA maps for the undisturbed tuff panel (Fig. 4.42a,b) confirm the generally uniform response among the different configurations (with or without Plexiglas), observed before. After the load test the main fracture is clearly visible (in particular with the Plexiglas interposition, Fig. 4.42d) and similarly to the time slices of Fig. 4.36 and dielectric constant maps (Figs. 4.39-4.40), a high amplitude zone located in the top-right part of Fig. 4.42c ("A" zone) is highlighted, even if less evident.

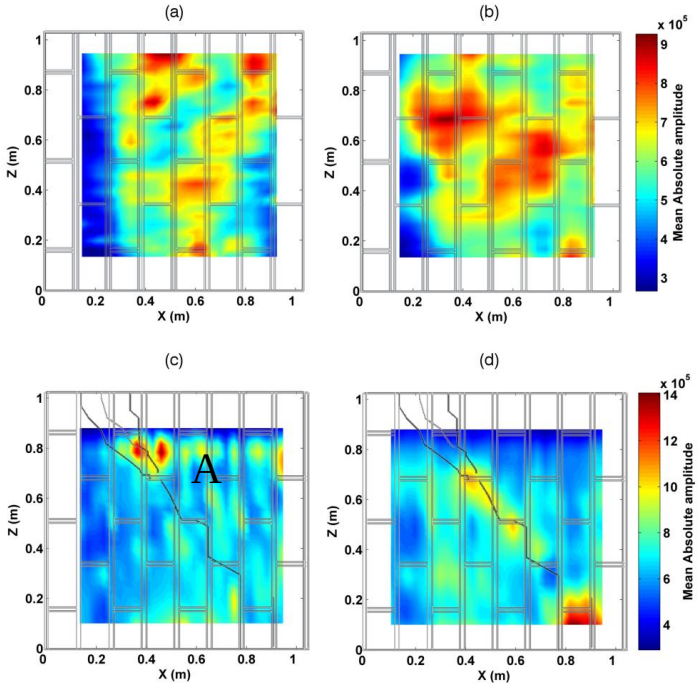


*Figure 4.42. Mean absolute amplitude calculated for the laboratory tuff sample before the load application, without (a) and with 10 mm of Plexiglas (b), and after the load application without (c) and with 10 mm of Plexiglas (d)*

✓ 4.3.4.5 ERT

Results of 3D ERT inversion were analysed in terms of depth slices (5, 10, 15 cm), directly comparable with the GPR time slices of Figs. 4.27-4.32. However only the shallowest section is significant (depth = 5±5 cm), since the resolution of ERT method rapidly decrease with depth and the deeper sections have a degree of resolution not compatible with these goals.

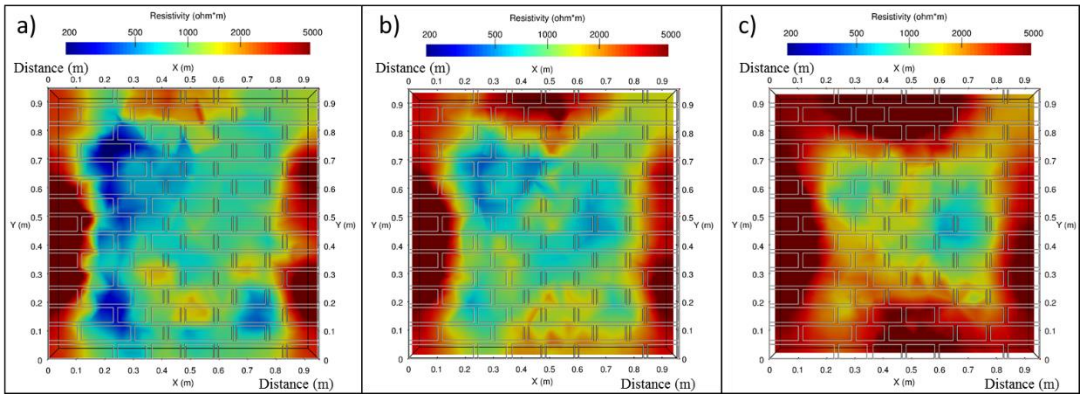


*Figure 4.43: Before load application bricks sample: ERT resistivity map related to increasing depths: 5 cm (a); 10 cm (b); 15 cm (c)*

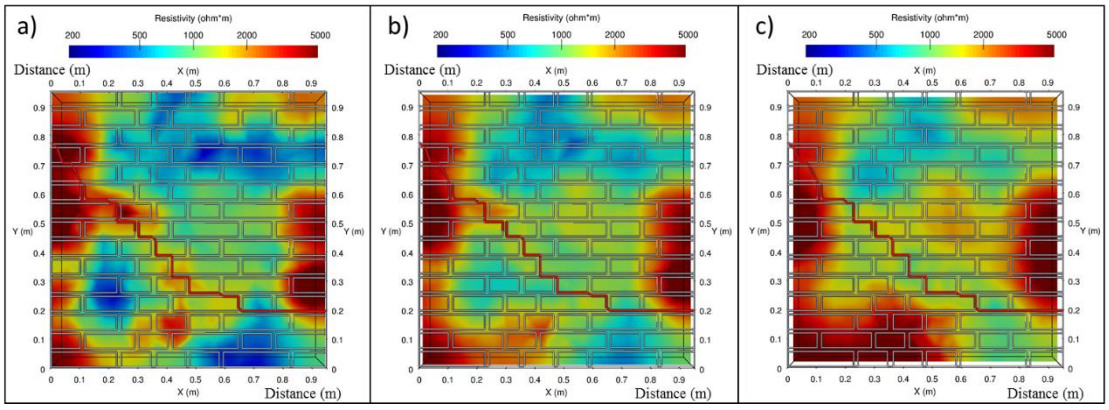


*Figure 4.44: After load application brick sample: ERT resistivity map related to increasing depths: 5 cm (a); 10 cm (b); 15 cm (c)*

ERT inverted models are represented in Figs. 4.43 and 4.44 (bricks) and 4.45 and 4.46 (tuff) respectively before (Figs. 4.43-4.45) and after (Figs. 4.44-4.46) the load application. Although the resolution is lower with respect to GPR both models are able to correctly depict the fractures. In fact, there are noteworthy differences between the undisturbed (Figs. 4.43 and 4.45) and the fractured (Figs. 4.44 and 4.46) configurations, where higher resistivity values are retrieved in correspondence of the fracture.

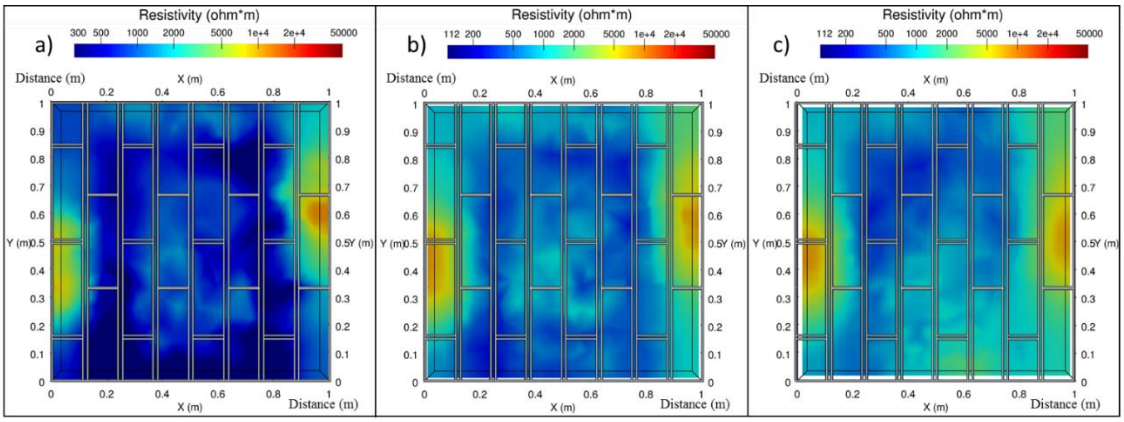


*Figure 4.45: Before load application tuff sample: ERT resistivity map related to increasing depths: 5 cm (a); 10 cm (b); 15 cm (c)*

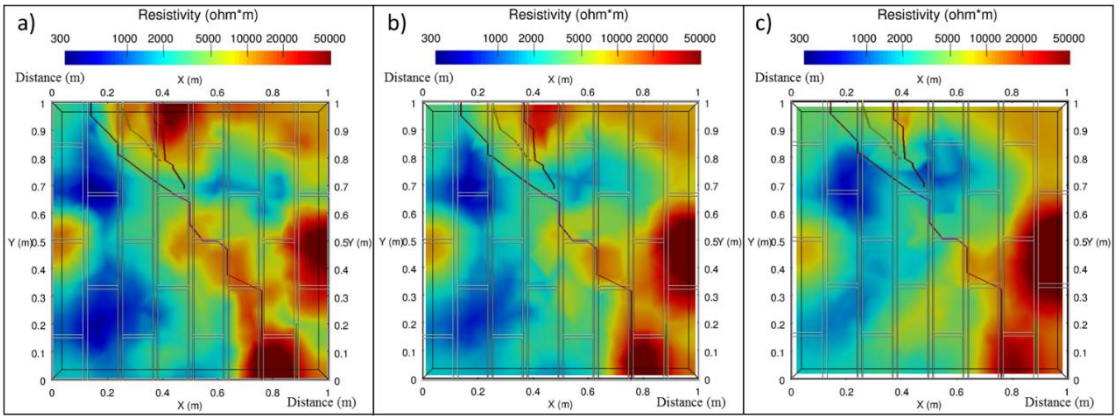


*Figure 4.46: After load application tuff sample: ERT resistivity map related to increasing depths: 5 cm (a); 10 cm (b); 15 cm (c)*

This effect is enhanced on the tuff sample (Fig. 4.45-4.46), more homogenous compared to the bricks panel (Fig. 4.43-4.44), except for some boundary effects. Resistivity models of undisturbed panels are almost homogenous denoting a mean resistivity of 700 Ωm and 500 Ωm for tuff and bricks respectively, comparable with the values obtained in the laboratory on single blocks. The bricks panel exhibits a relative conductive zone (x = 0.15-0.3 m, ρ = 300 Ωm) as a function of their arrangement within the panel (one or two rows), due to the presence of the single row of bricks, as displayed before in Figs. 4.30, 4.38b and 4.41b.

After the load application, the bricks sample (Fig. 4.44) displays high resistivity values in correspondence of the fracture and in the bottom-left zone, that are the most weakened areas. The main fracture is also detected on the tuff sample (high resistivity), and the sample is divided into two main zones due to a different degree of fracturing: high resistivity (ρ ≥ 10000 Ωm) in the upper right part of the sample and a relative conductive zone in the bottom left part (x = 0.15-0.3 m, ρ = 300 Ωm).

## 4.4 Data integration

At the end, we compare the results of GPR and ERT methods, separately for bricks and tuff samples before and after load application.

✓ *4.4.1 Bricks sample*

- Before load application

We compare in Fig. 4.47 the GPR time slice (Fig. 4.30c), the ERT horizontal section (Fig.4.43a), the MAA (Fig. 4.41b) and the dielectric constant maps (Fig. 4.38b) related to the bricks sample before the load application.

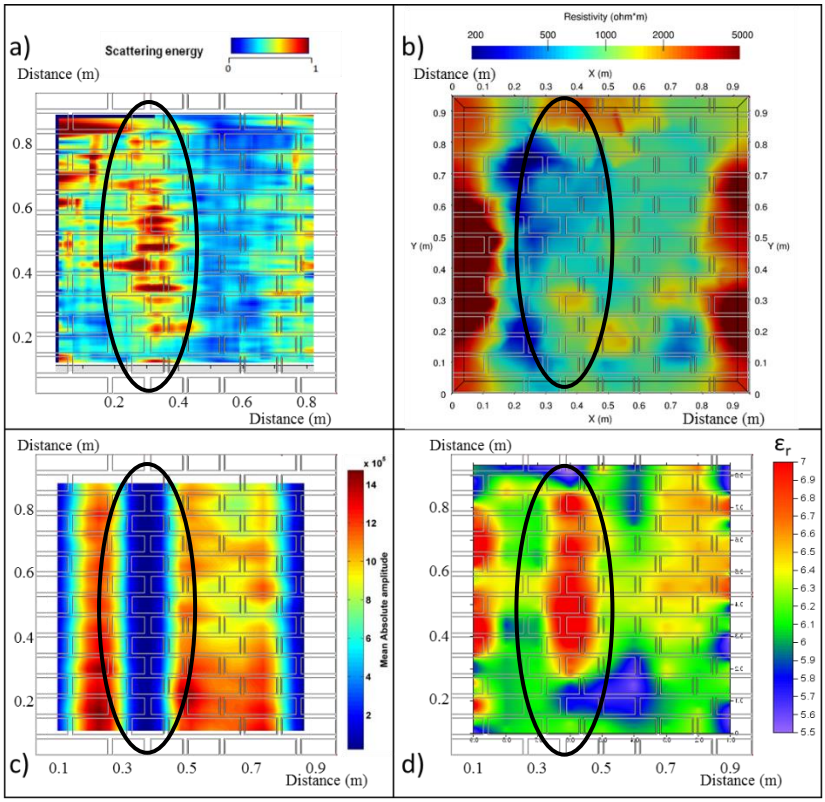


*Figure 4.47: Bricks sample. Comparison of data before load application: a) GPR time slice; b) ERT resistivity map; c) Mean absolute amplitude map; d) Dielectric constant map*

All proposed methods are able to detect the heterogeneity due to the sample geometry. In particular, in the area characterized by a single row of bricks (black ellipse), high values of dielectric constant are found (red zone in Fig. 4.47d), together with low resistivity and high signal attenuation (Fig 4.47 b and 4.47c respectively).

- After load application

We compare in Fig. 4.48 the GPR time slice (Fig. 4.31c), the ERT horizontal section (Fig. 4.44a), the MAA (Fig. 4.41d) and the dielectric constant maps (Fig. 4.44a) related to the bricks sample after the load application.

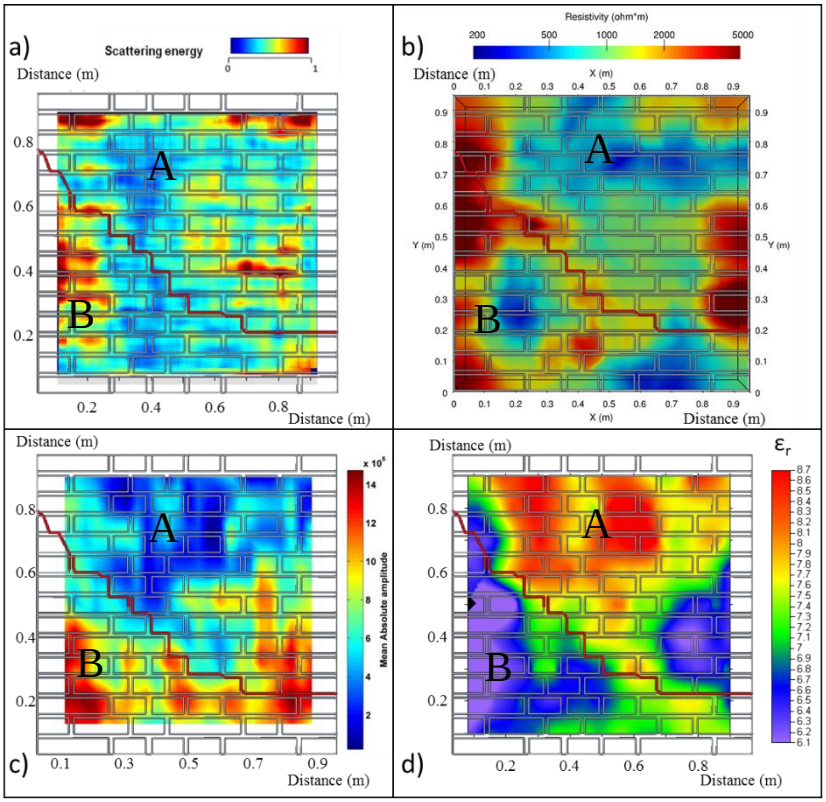


*Figure 4.48: Bricks sample. Comparison of data after load application: a) GPR time slice; b) ERT resistivity map; c) Mean absolute amplitude map; d) Dielectric constant map*

After the load test, Fig. 4.48 shows two different areas, located above and below the main fracture, in terms of the studied parameters. In particular, we can associate high resistivity values, together with high GPR scattering ("B" zone in Fig. 4.48a,b). As a confirmation of this, the same area (B) shows lower permittivity ("B" zone in Fig. 4.48d) and attenuation of the GPR signal ("B" zone in Fig.4.48c). In fact, high permittivity values ("A" zone in Fig. 4.48d), can be associated with lower resistivity values ("A" zone in Fig. 4.48d), indicating a lower degree of fracturing of the panel.

### ✓ *4.4.2 Tuff sample*

- Before load application

Even for the tuff sample we compare in Fig. 4.49 the time-slice (Fig. 4.35a), the ERT horizontal section (Fig. 4.45a), the MAA (Fig. 4.42a) and the dielectric constant maps (Fig. 4.39a) before the load application.

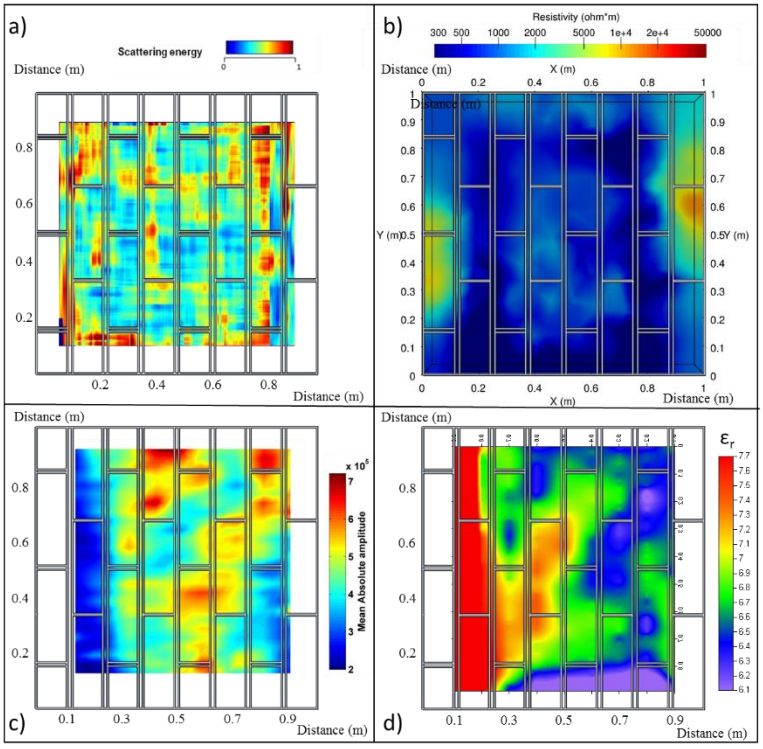


*Figure 4.49: Tuff sample. Comparison before load application: a) GPR time slice; b) ERT resistivity map; c) Mean absolute amplitude map; d) Dielectric constant map*

The GPR time slices (Fig. 4.49a) show a higher scattering that may be associated to the joints between the blocks, while the other maps, having a lower resolution, can give an estimation of the global behaviour of the sample. ERT model (Fig. 4.49b) shows a globally homogeneous response, while the left area of the sample (x=0-0.1 m) is characterized by a high value of the dielectric constant and a low signal amplitude (Fig. 4.49c,d), probably as a result of a boundary effect due to the presence of a steel beam, close to the sample.

- After load application

We compare in Fig. 4.50 the time-slice (Fig. 4.36c), the ERT horizontal section (Fig. 4.46a), the MAA (Fig. 4.42d) and the dielectric constant maps (Fig. 4.40b), after the load application.

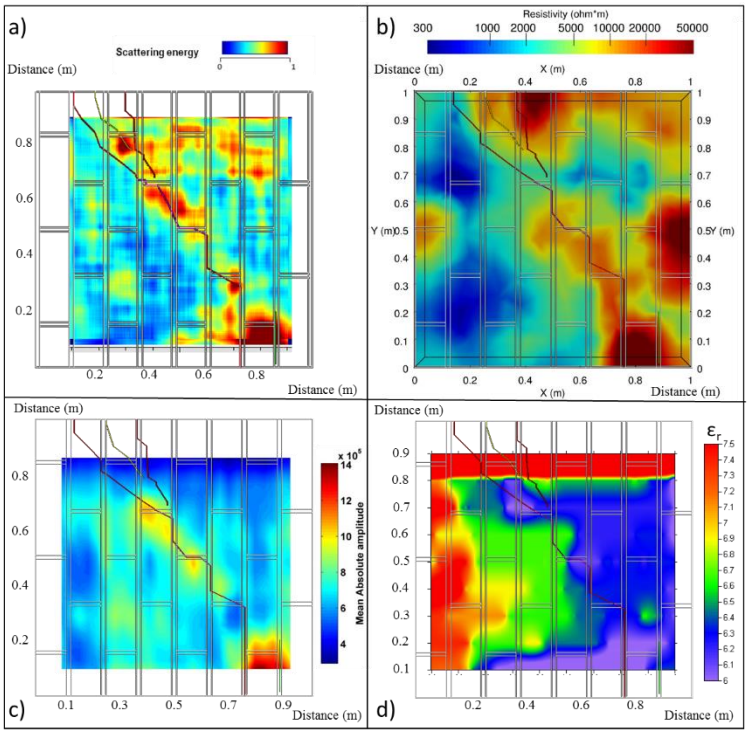


*Figure 4.50: After load application tuff sample comparison: a) GPR time slice; b) ERT resistivity map; c) Mean absolute amplitude map; d) Dielectric constant map*

The investigation of the fractured panel gives homogenous results among the techniques employed: high GPR scattering (Fig. 4.50a), high ERT resistivity (Fig. 4.50b) and low dielectric constant values (Fig. 4.50c) can be seen in the fractured zone, indicating a high level of stress of the masonry (Fig. 4.50), except for some boundary effects highlighted in the ERT slice at x = 0.9-1.0 (out of the GPR investigated area) and y = 0.3-0.5.

# CONCLUSIONS

This thesis has been developed with the aim to explore thoroughly potential and limit of the GPR and ERT methods for monitoring heterogeneous structures where different construction materials are combined together.

Firstly we analysed the GPR response, due to the different construction materials related to different modern, historical or archaeological structures. In particular, three test sites during this work were investigated: the Pyramid of Caius Cestius, the Passage of Commodus and the Colle Oppio Nymphaeum in Rome. As expected, field examples highlighted different GPR responses according to the different types of material and frequency antennas, because the attenuation is directly correlated to the building material and resolution to antenna frequency and size of the target. In detail, the case study of the Pyramid, where blocks are compact and homogeneous, represents the *optimum* with high resolution and signal penetration. On the contrary the Nymphaeum wall displays low resolution resulting from a non-optimal antenna-wall coupling and from the roughness of the wall. Moreover, even by increasing the frequency, we do not obtain an evident increase of the resolution in the shallower layer. Nevertheless, the frequency increase corresponds to a higher scattering for the smaller objects, making more complex the interpretation of GPR sections.

In light of this, the interposition between the surface of the investigated medium and the GPR antenna of a dielectric material (e.g. Plexiglas) was studied in order to improve the vertical resolution of the shallow subsurface, avoiding the direct wave overlapping, despite losing horizontal resolution.

Furthermore, the diagnostic potential of the joint interpretation of GPR and ERT data was analysed for the characterization of reinforced masonry structures, widespread in historical centers affected by huge earthquakes in the last decade (e.g. Central Italy). In light of this, an important issue is represented by the capability to detect fractures within the masonry and to discriminate the response due to weakened zones and construction materials.

To this aim a combined application of the GPR and ERT methods for monitoring a load test executed on masonry samples is presented. These panels were built up in the laboratory controlled conditions using tuff and bricks (materials employed in Italy for decades for masonry buildings), and reinforced with a high-conductive fibre fabric. The

geophysical investigations were performed before and after the application of a diagonal compression load.

Firstly synthetic models, reproducing the laboratory samples, were developed for analysing the effect of the different construction materials and of the load application, with the additional goal to understand the benefit given by a dielectric layer, placed underneath the GPR antenna, for reconstruction of anomalies. The results demonstrated the capability of the method to detect the different geometry of the masonry sample (orientation of bricks, joints) and, after the load test, to clearly detect the fractures, even though the benefit of the Plexiglas layer was limited for acquisition made on the unreinforced face of the samples. However, thanks to the presence of the Plexiglas, a better discretization of the shallower part of the sample was obtained, since this part is often hidden from the direct wave.

The corresponding laboratory data display similar results, both in terms of detectability of anomalies and of the role played by the dielectric layer.

A strong improvement is observed in the GPR synthetic radargrams related to the bricks and tuff panels, investigated from the reinforced face, where the high-conductive fabric prevents the signal propagation in the absence of the dielectric layer.

In particular for the GPR laboratory data acquired directly on the reinforced face of samples, it is demonstrated that the interposition of a dielectric material between the antenna and the structure can improve substantially the coupling and consequently the capability to detect fractures and to reach the rear face of the sample, despite losing resolution. Moreover, mapping the GPR data in terms of the dielectric constant and mean absolute amplitude is particularly diagnostic to detect the effective fracturing pattern, after the application of the diagonal load. In fact we have lower dielectric constant together with higher amplitudes in presence of a high degree of fracturing. Consequently, this procedure can reduce the degree of uncertainty in the detection of fractures, voids or cavities, with respect to the standard processing, consisting of radargrams and time-slices amplitude analysis. In this sense, the ERT technique can be complementary used to validate the GPR evidence, where more resistive zones are associable with the presence of fractures and weakness zones. In fact, given the low resolution of the electrical method, it cannot be employed for these purposes as a standalone technique.

At the end, this thesis demonstrated that the integrated application of GPR and ERT investigations can be a reliable tool to check the effects of static load tests, due to the complete non-invasiveness, the cost-effectiveness and the high-resolution achieved by these methods. Therefore, this procedure can be extended to whole load cycle (before, during and after the experiment), with the primary aim to have a quantitative assessment of the effective distribution of fractures within the sample during the load application.
Finally, in light of the results achieved for reinforced masonries, it will be important to evaluate the benefit of the interposition of a dielectric layer for different type of structures, materials and geometries. In fact, this add-on, once specifically engineered and sized, could be easily implementable with a standard GPR system and could also be applied in the investigation in presence of high-conductive media (reinforcements, bars or materials with high moisture contents), in order to improve the detectability of hidden objects.

# REFERENCES

Abbas, A., Kamei, H., Helal, A., Atya, M., & Shaaban, F. (2005). "Contribution of geophysics to outlining the foundation structure of the Islam Museum, Cairo, Egypt". *Archaeological Prospection, vol. 12*, 167-176.

Akhter, Z., & Akhtar, M. J. (2016). "Free-Space Time Domain Position Insensitive Technique for Simultaneous Measurement of Complex Permittivity and Thickness of Lossy Dielectric Samples". *IEEE TRANSACTIONS ON INSTRUMENTATION AND MEASUREMENT, VOL. 65*, 2394-2405.

Alldred, J. C. (1995). "Improvements to the orthogonal method for determining reinforcing bar diameter usin a cover meter". *Engineering Technics Press, vol. 2.*, 11-5.

Al-Qadi, I., & Lahouar, S. (2005). "Measuring layer thicknesses with GPR-theory to practice" . *Constr Build Mater*, 763-72.

Annan, A. P. (1996). Transmission dispersion and GPR. *JEEG*, 125-136.

Annan, A. P. (2003). *"Introduction to GPR, Sensor & Software, Inc.-Tutorial notes".*

Annan, A. P. (2005). *"Ground peetrating radar, in near surface geophysics", in D. K. Butler (eds), Society of Exploration Geophysicists, Tulsa, OK, USA.* 357-438: Investigation in Geophysics No. 13.

Annan, A. P., & Davis, J. L. (1992). "Design and development of a digital ground penetratind radar system". *Pilon, J. (Ed.) Ground Penetrating Radar. Geol. Surv. Can.* , 90-4.

ASTM E 519-07. (2007). *"Standard test method for diagonal tension (shear) in mansory assemblages".* West Conshohocken: America Society for Testing and Materials.

Balanis, C. A. (2005). *Antenna Theory: Analysis and Design. 3rd Edition.* New York: John Wiley & Sons.

Balanis, C. A. (2012). *"Advanced Engineering Electromagnetics-2nd ed.".* John Wiley & Sons, Inc.

Bano, M. (1996). Constant dielectric losses of ground penetrating radar waves. *Geophysical Journal International*, 279-288.

Barrile, V., & Pucinotti, R. (2005). "Application of radar technology to reinforced concrete structures: a case study". *NDT&E Int*, 596-604.

Bergmann, T., Robertsson, J. O., & Holliger, K. (1998). "Finite-difference modelling of electromagnetic wave propagation in dispersive and attenuating media". *Geophysics*, 856–67.

Bevan, B. W., & Kenyon, J. (1975). "Ground Penetrating Radar for historical archaeology". *Masca Newsletter*, 2-7.

Born, M., & Wolf, E. (1980). *"Principles of Optics, 6th edition"*. Oxford, UK: Pergamon Press.

Bourgeois, J., & Smith, G. (1996). "A fully three-dimensional simulation of a ground-penetrating radar: FDTD theory compared with experiment". *IEEE T Antenn Propag*, 36–44.

Bungey, J. H. (1994). "The testing of concrete in structures". 228.

Bungey, J. H. (2004). "Sub-surface radar testing of concrete: a review". *Construction and Building Materials*, 1-8.

Cardarelli, E., & De Nardis, R. (1998). "The use of 3D and 2D seismic tomography for assessing the physical integrity of building panels". *European Journal of Environmental and Engineering Geophysics 3*, 131-142.

Cardarelli, E., & Di Filippo, G. (2009). "Integrated geophysical methods for the characterisation of an archaeological site (Massenzio Basilica—Roman forum, Rome, Italy)". *Journal Applied of Geophysics* , 508-521.

Cardarelli, E., G. De Donno, G., Scatigno, C., Oliveti, I., Preite Martinez, M., & Prieto-Taboada, N. (2016). "Geophysical and geochemical techniques to assess the origin of rising damp of a Roman building (Ostia Antica archaeological site)". *Microchemical Journal*, 49-57.

Cardarelli, E., Godio, A., Morelli, G., Sambuelli, L., Santarato, G., & Socco, L. (2002). "Integrated geophysical surveys to investigate the Scarsella vault of St. John's Baptistery in Florence". *The Leading Edge 21*, 467-470.

Cassidy, N. J. (2007). "GPR frequency-dependent attenuation and velocity charateristics of nano-to-microscale, lossy, magnetite-rich materials". *Near Surface Geophysics*.

Cassidy, N. J., & Millington, T. M. (2009). “The application of finite-difference time-domain modelling for the assessment of gpr in magnetically lossy materials”. *Journal of Applied Geophysics, vol. 67, no. 4*, 296-308.

Charles Stokes Ritchie, C. N., & Edward A. Burkard, E. A. (2002). *NY (US) Patent No. 0090871 A1*.

Clough, J. W. (1976). "Electromagnetic lateral waves observed by earth-sounding radars". *Geophysics 41*, 1126-1132.

Colla, C., Das, P., McCann, D., & Forde, M. (1997). "Sonic, electromagnetic and impulse radar investigation of stone masonry bridges". *NDTE International*, 249-254.

Colla, C., McCann, D. M., Das, P. C., & Forde, M. C. (1996). "Non-contact, NDE of masonry structures and bridges". *Proceedings of the Third Conference on Nondestructiive Evaluation of Civil Structures and Materials. University of Colorado at Boulder*, 441–54.

Conyers, L. (2013). *"Ground penetrating radar for archaeology"*. UK: AltaMira press.

Cook, J. C. (1974). "Status of ground-probing radar and some recent experience". *Proc. Conf. Subsurface Exploration for Underground Excavation and Heavy Construction. Am. Soc. Civ. Eng.*, 175-194.

Cook, J. C. (1975). "Radar transparencies of mine and tunnel rocks". *Geophys.*, 865-885.

Daniels, D. J. (1996). "Subsurface penetrating radar". *London: The Institution of Electrical Engineers*.

Daniels, D. J. (1996). *"Surface Penetrating Radar, Radar, Sonar, Navigation and Avionics Series 6"*. London, UK: The institute of Electrical Engineers.

Daniels, D. J. (2004). *"Ground Penetrating Radar 2nd Edition"*. London, UK: David J. Daniels.

De Donno, G. (2013). "2D tomographic inversion of complex resistivity data on cylindrical models". *Geophysical Prospecting 61(Suppl.1)*, 586–601.

De Donno, G., & Cardarelli, E. (2014). "3D complex resistivity tomography on cylindrical models using EIDORS, Near Surface". *Geophysics 12(5):*, 587-598.

De Donno, G., & Cardarelli, E. (2016). "VEMI: a flexible interface for 3D tomographic inversion of time- and frequency-domain electrical data in EIDORS". *Near Surface Geophysics*.

Diamanti, N., Tsokas, G., Tsourlos, P., & Vafidis, A. (2005). "Integrated Interpretationof Geophysical Datainthe Archaeological Site of Europos (Northern Greece)". *Archaeological Prospection, 12* , 79-91.

Elsener, B., Andrade, C., Gulikers, J., Polder, R., & Raupach, M. (2003). "Half-cell potential measurements - Potential mapping on reinforced concrete structures". *Materials and Structures*, 461-471.

Evans, S. (1963). 'Radio techniques for the measurement of ice thickness'. *Polar Record*, 406-410.

Fisher, E., McMechan, G. A., & Annan, A. P. (1992). "Acquisition and processing of wide-aperture ground penetrating radar data". *Geophysics, Vol. 57*, 495.

Fletcher, J. F., & Woolhouse, C. I. (2012). "Practical operation of data-logging covermeters and the interpretation of results". *3rd International Conference on Concrete Repair, Rehabilitation and Retrofitting, ICCRRR 2012*, 715-722.

Forde, M. C., & Mackie, R. I. (1996). "Non-destructive evaluation of a bonded externally reinforced concrete bridge using the frequency response function method". *ICCI'96, University of Arizona* , 1031–8.

Gaffney, C. (2008 ). "Detecting trends in the prediction of the buried past: A review of geophysical techniques in archaeology". *Archaeometry 50*, 313-336.

Giannopoulos, A. (2005). "Modelling ground penetrating radar by GprMax". *Construction and Building materials, 19*, 755-762.

Golubića, S., Pietrini, A. M., & Ricci, S. (2015). "Euendolithic activity of the cyanobacterium Chroococcus lithophilus Erc. In biodeterioration of the Pyramid of Caius Cestius, Rome, Italy". *International Biodeterioration & Biodegradation*, 7-16.

Goodman D. and Nishimura Y. (1993). Ground radar view of Japanese burial mounds. *Antiquity*, 224-232.

Grandjean, G., Gourry, J. C., & Bitri, A. (2000). "Evaluation of GPR techniques for civil-engineering applications: study on a test site". *Journal Applied of Geophysics*, 141-56.

Greaves, R. J., Lesmes, D. P., Lee, J. M., & Toksoz, M. N. (1996). "Velocity variation and water content estimated from multi-offset, ground penetrating radar". *Geophysics, Vol. 61*, 683-695.

Grote, K., Hubbard, S., Harvey, J., & Rubin, Y. (2005). "Evaluation of infiltration in layered pavements using surface GPR reflection techniques". *Journal Apllied of Geophisics*, 129-53.

Hadi, M., & Preko, K. (2013). "Thickness evaluation of asphalt and base layers of some major and minor arterial roads in Kumasiusing ground penetrating radar". *International Journal of Scientific & Engineering Research Volume 4*.

Hasted, J. B. (1972). *"Aqueous Dielectrics"*. London, UK: Chapman and Hall.

Hoła, J., Sadowski, Ł., & Schabowicz, K. (2009). "Nondestructive evaluation of the concrete floor quality using impulse response method and impact-echo method". *e-Journal of Nondestructive Testing & Ultrasonics*.

Hollender, F., & Tillard, S. (1998). Modeling ground-penetrating radar wave propagation and reflection with the Jonscher parameterization. *Geophysics*, 1933-1942.

Honcharenko, W., & Bertoni, H. L. (1994). "Transmission and reflection characteristics at concrete block walls in the UHF bands proposed for future PCS". *IEEE Trans. Antennas Propagat., vol. 42*, 232-239.

Hulsenbeck, e. a. (1926). *German Patent No. 489434.*

Isaaks E.H. and Srivastava R.M. (1989). An introduction to applied geostatics. New York: Oxford University Press.

Jackson, J. D. (1962). *"Classical Electrodynamics"*. New York: John Wiley and Sons.

Jol, H. (1995). Ground penetrating radar antennae frequencies and transmitter powers compared for penetration depth, resolution and reflection continuity. *Geophysical Prospecting*, 693-709.

Jol, H. M. (2009). *"Ground Penetrating Radar: Theory and applications"*. Oxford: Elsevier Science.

Jonscher, A. K. (1977). The universal dielectric response. *Nature*, 673-679.

Kadaba, P. K. (1976). "Penetration of 0.1 GHz to 1.5 GHz electromagnetic waves into the earth surface for remote sensing applications". *Proc. IEEE S. E. Region 3 Conf*, 48-50.

King, R. W., & Smith, G. S. (1981). *"Antennas in matter"*. Cambridge, MA: MIY Press.

Kylili, A., Fokaides, P. A., Christou, P., & Kalogirou, S. A. (2014). "Infrared thermography (IRT) applications for building diagnostics: A review". *Applied Energy*, 531-549.

La Regina, A. (2009). *"Sangue e arena"*. Milan: Mondadori Electa.

Linan, C. R., Morales Conde, M. J., De Hita, P. R., & Galvez, F. (2015). "Application of non-destructive techniques in the inspection of wooden structures of protected

buildings: The case of nuestra señora de los dolores church (Isla Cristina, Huelva)". *International Journal of Architectural Heritage*, 324-340.

Liu, L., Lane, J. W., & Quan, Y. (1998). "Radar attenuation tomography using the centroid frequency". *Journal of Applied Geophysics 40*, 105-116.

Lorenzo, H., & Cuéllar, V. H. (2001). "Close range radar remote sensing of concrete degradation in a textile factory floor". *Journal Apllied of Geophisics* , 327-36.

Marcari, G., Basili, M., & Vestroni, F. (2016). "Experimental investigation of tuff masonry panels reinforced with surface bonded basalt textile-reinforced mortar". *Composite Part B*, 131/142.

Martinez, A., & Byrnes, A. P. (2001). "Modeling Dielectric-constant values of Geologic Materials: An Aid to Ground-Penetrating Radar Data Collection and Interpretation". *Kansas Geological Survey. Vol. 247*, 1-16.

McCann, D. M., & Forde, M. (2001). "Review of NDT methods in the assessment of concrete". *NDT&E International* , 71-84.

Medeiros, P. X. (2006). A practical approach to correct attenuation effects in GPR data. *Journal of Applied Geophysics*, 140-151.

Mishin, A. V. (1997). "Portable linear electron accelerators for electron beam curing of composites,non-destructive testing and other applications". *Engineering Technics Press. Proceedings of the Seventh International Conference on Structural Faults & Repair*, 367-73.

Mocchegiani Carpano, C. (1977). *"Nuovi dati sulle fondazioni dell'Anfiteatro Flavio"*. Roma: Antiqua II-7.

Mol, L., & Preston, P. (2010). "The writing's in the wall: a review of new preliminary applications of electrical resistivity tomography within archaeology". *Archaeometry, 52*, 1079-1095.

Morey, R. M. (1974). "Continuous sub-surface profiling by impulse radar". *Proc. Conf. Subsurface Exploration for Underground Excavation and Heavy Construction*, 213-232.

Najjar, W., Aderhold, H. C., & Hover, K. C. (1986). "The application of neutron radiography to the study of micro cracking in concrete, Cement. Concrete Aggregates". *CCAGDP*, 103-10.

Neal, A. (2004). "Ground-penetrating radar and its use in sedimentology: principles, problems and progress". *Earth-Science Reviews*, 261-330.

Neubauer, W., Eder-Hinterletner, A., Seren, S., & Melichar, P. (2002). "Georadar in the Roman civil town Carnuntum, Austria: an approach for archaeological interpretation of GPR data". *Archaeological Prospection vol.9*, 135-156.

Ohtsu, M., Yamamoto, T., & Matsuyama, K. (1997). "Quantitative NDE estimation for rebar corrosion in concrete. Proceedings of the Seventh International Conference on Structural Faults & Repair". *Engineering Technics Press, vol. 2. ,* 265.

Orlando , L., Pezone, A., & Colucci, A. (2009). Modeling and testing of high frequency GPR data for evaluation of structural deformation. *NDT&E International*, 216-230.

Orlando, L. (2007). Using GPR to monitor cracks in a historical building. *4th internetional workshop on advanced ground penetrating radar*, (pp. 45-7). Naples.

Orlando, L. (2012). "Detecting steel rods and micro-piles: A case history in a civil engineering application". *Journal of Applied Geophysics*, 130-138.

Orlando, L., & Renzi, B. (2013). "Non-destructive testing to the characterization of Moai statues (Easter Island-Chile)". *Archaeological Prospection 20*, 23-37.

Orlando, L., & Slob, E. (2009). "Using multi component GPR to monitor cracks in a historical building". *Journal of Applied Geophysics, vol.67*, 327-334.

Orlando, L., Cardarelli, E., & Cercato, M. D. (2015). "Characterization of a Pre-Trajan Wall by Integrated Geophysical Methods". *Archaeological Prospection*, 221-232.

Orlando, L., Cardarelli, E., Cercato, M., De Donno, G., & Di Giambattista, L. (2016). "Pavement testing by integrated geophysicals methods: feasibility, resolution and diagnostic potential". *Journal applied of geophysics*, 462-473.

Orlando, L., De Donno, G., & Renzi, B. (2014). "Intensity of scattering for the lithotype characterization of an excavated pre-Trajan wall". *15th International Conference on Ground Penetrating Radar - GPR 2014.* Brussels.

Owen, R., & DeBaun. (1997). "Portable linear accelerators for X-ray and electron beam applications in civil engineering". *Engineering Technics Press. Proceedings of the Seventh International Conference on Structural Faults & Repair*, 395-405.

Pena, D., Feick, R., Hristov, H. D., & Grote, W. (2003). "Measurement and Modeling of Propagation Losses in Brick and Concrete Walls for the 900-MHz Band". *IEEE TRANSACTIONS ON ANTENNAS AND PROPAGATION*, Vol. 51, NO. 1.

Peña, D., Feick, R., Hristov, H., & Grote, W. (2003). "Measurement and Modeling of Propagation Losses in in brick and concrete walls for the 900-MHz band". *IEEE Transactions on antennasand propagation Vol. 51, No. 1,* 31-39.

Perez-Gracia, V., Garcia Garcia, F., & Rodriguez Abad, I. (2008). "GPR evaluation of the damage found in the reinforced concrete base of a block of flats: A case study". *NDT&E International 41*, 341-353.

Pieraccini, M., Luzi, G., & Atzeni, G. (2001). "Terrain mapping by ground-based interferometric radar". *IEEE Transactions on Geoscience and Remote Sensing, 39* , 2176–2181.

Pieraccini, M., Luzi, G., Mecatti, D., Fratini, M., Noferini, L., Carissimi, L., . . . Atzeni, C. (2004). "Remote sensing of building structural displacements using a microwave interferometer with imaging capability". *NDT & E International, 37,* 545-550.

Pieraccini, M., Mecatti, D., Noferini, L., Luzi, G., Franchioni, G., & Atzeni, C. (2002). "SAR interferometry for detecting the effects of earthquakes on buildings". *NDT & E International, 35*, 615-625.

Piro, S., Goodman, D., & Nishimura, Y. (2003). "The study and characterization of Emperor Traiano's Villa (Altopiani di Arcinazzo, Roma) using high-resolution integrated geophysical surveys". *Archaeological Prospection, vol.10*, 1-25.

Plumb, R., Noon, D., Longstaff, I., & Stickley, G. (1998). A waveform-range performance diagram for ground-penetrating radar. *Journal of Applied Geophysics*, 117-126.

Polymenakos, L., Papamarinopoulos, S., Miltiadou, A., & Charkiolakis, N. (2002). "Investigation of the foundations of a Byzantine church by three-dimensional seismic tomography". *Journal of Applied Geophysics 57*, 81-93.

Powers, M. H. (1997). Modeling frequency-dependent GPR. *The Leading Edge*, 1657-1662.

Rea, R., Beste, H., & Lancaster, L. (2002). "Il cantiere del Colosseo". *Cantieri Antichi*, 341-375.

Reynolds, J. M. (1997). *"An introduction to Applied and Environmental Geophysics"*. Chichester, England: John Wiley & Sons.

Roe, K. C., & Ellerbruch, D. A. (1979). "Development and testing of a microwave system to measure coal layer thickness up to 25 cm". *Nat. Bur. Stds., Report No.SR-723-8-79*.

Saarenketo, T., & and Aho, S. (2005). "Monitoring and classifying spring thaw weakening on low volume roads in northern periphery". 11.

Sansalone, M. J., & Street, W. B. (1997). "Impact–echo: non-destructive evaluation of concrete and masonry". *Ithica, NY: Bullbrier Press*.

Sass, O. (2005). "Rock moisture measurements: techniques, results, and implications for weathering". *Earth Surf. Process. Landf., 30*, 359-374.

Sass, O., & Viles, H. (2010). "Wetting and drying of masonry walls: 2D-resistivity monitoring of driving rain experiments on historic stonework in Oxford, UK". *Journal Applied of Geophysics, 70*, 72-83.

Shaari, A., Millard, S. G., & Bungey, J. H. (2004). "Modelling the propagation of a radar signal through concrete as a low-pass filter". *NDT&E Int*, 237-42.

Shangguan, P., & Al-Qadi, I. L. (2015). “Calibration of fdtd simulation of gpr signal for asphalt pavement compaction monitoring,” . *Geoscience and Remote Sensing, IEEE Transactions on, vol. 53, no. 3, pp. 1*, 1538–1548.

Sharma, A., Sandhu, B. S., & Singh, B. (2011). "A gamma ray tomographic densitometer system for the investigation of concrete structures". *Journal of the Korean Physical Society*, 3.

Slob, E. a. (2002). "Coupling effects of two electric dipoles on an interface". *Radio Science, VOL. 37, NO. 5*, 1073.

Solla, M., Lorenzo, H., Rial, F., & Novo, A. (2012). “Ground-penetrating radar for the structural evaluation of masonry bridges: Results and interpretational tools”. *Construction and Building Materials, vol. 29*, 458-465.

Stanley, C., & Balendran, R. V. (1995). "Developments in assessing the structural integrity of applied surfaces to concrete buildings and structures using infra-red thermography". *Engineering Technics Press. Proceedings of the International Conference on Structural Faults & Repair*, 39-44.

Steenson, B. O. (1951). "Radar methods for the exploration of glaciers". *PhD Thesis, Calif. Inst. Tech., Pasadena, CA, USA*.

Streich, R., & Van der Kruk, J. (2007a). "Accurate imaging of multicomponent GPR data based on exact radiation patterns". *IEEE Transactions on Geoscience and Remote Sensing 45*, 93-103.

Streich, R., & Van der Kruk, J. (2007b). "Vector migration of standard copolarized 3D GPR data". *Geophysics 72*, J65–J75.

Taflove, A. (1995). "Computational electrodynamics: the finite-difference time-domain method". *Artech House*.

Tarchi, D., Rudolf, H., Pieraccini, M., & Atzeni, C. (2000). "Remote monitoring of buildings using a ground-based SAR: application to cultural heritage survey". *International Journal of Remote Sensing, 21*, 3545-3551.

Tran, A. P., Andre, F., & Lambot, S. (2014). "Validation of near-field ground penetrating radar modeling using full-wave inversion for soil moisture estimation". *Geoscience and Remote Sensing, IEEE Transactions on, vol. 52, no. 9*, 5483-5497.

Turner, G., & Siggins, A. (1994). "Constant Q attenuation of subsurface radar pulse". *Geophysics, Vol.59, No.8*, 1192-1200.

Turner, G., & Siggins, A. F. (1994). Constant Q attenuation of subsurface. *Geophysics*, 1192-1200.

Unterberger, R. R. (1978). "Radar and sonar probing of salt". *5th Int. Symp. on Salt* (pp. 423-437). Hamburg: Northern Ohio Geological Society.

Van der Kruck, J., Wapenaar, C., Fokkema, J., & Van Den Berg, P. (2003). Improved three-dimensional image reconstruction technique for multi-component ground penetrating radar data. *Subsurface Sensing Technologies and Applications*, 61-99.

Vasanelli, E., Calia, A., Luprano, V., & Micelli, F. (2016). "Ultrasonic pulse velocity test for non-destructive investigations of historical masonries: an experimental study of the effect of frequency and applied load on the response of a limestone". *Materials and structures*.

Warren, C., Giannopoulos, A., & Giannakis, I. (2015). "An advanced gpr modelling framework: The next generation of gprmax". *Advanced Ground Penetrating Radar (IWAGPR), 2015 8th International Workshop on*, 1-4.

Warren, C., Pajewski, L., Ventura, A., & Giannopoulos, A. (2016). "An Evaluation of Finite-Difference and Finite-Integration Time-Domain Modelling Tools for Ground Penetrating Radar Antennas". *2016 10th European Conference on Antennas and Propagation (EuCAP)*.

Watts, R. D., & England, A. W. (1976). "Radio-echo sounding of temperate glaciers: Ice properties and sounder design criteria". *Journal of Glaciology, Vol. 21*, 39-48.

# Figure captions